Observations of the Early Universe at millimetre wavelengths

Andrea Catalano

Communauté
UNIVERSITÉ Grenoble Alpes

MÉMOIRE

Présenté pour obtenir le diplôme d'

HABILITATION À DIRIGER DES RECHERCHES

Spécialité : **Physique**

Présentée par

Andrea CATALANO

Docteur en Astronomie et Astrophysique de l'observatorie de Paris
Chargé de Recherche au CNRS

préparée au sein du **Laboratoire de Physique Subatomique & Cosmologie (LPSC) - Grenoble**

"Observations of the Early Universe at millimetre wavelengths"

Thèse soutenue publiquement le **"05/11/2020"**,
devant le jury composé de :

Laurent Derome
President

Sophie Henrot-Versille
Referee

Ken Ganga
Referee

Bruno Maffei
Referee

A. Benoit
Member

"A bello fiore, che sempre mi ricorda io qui che ci sto a fare"

Merci, merci merci...

Les remerciements sont la partie que sans doute j'ai écrit les plus volontiers dans ce mémoire. Tellement volontiers que j'ai commencé ce travail par cela. Il y a beaucoup de personnes que je tiens à remercier pour avoir aidé mon parcours professionnel jusqu'à ici.

Avant tout, un énorme merci à mon ami et collègue Juan. Sa compétance, son dévouement et son empathie démesurée ont été pour moi un trésor unique.

Merci Alessandro, de réussir à garder le labo à flot malgré tout (et tous!). De long discours et quelque dispute (scientifique), je te dois beaucoup de mon expérience.

En outre, j'ai eu l'honneur d'être camarade scientifiques d'Alain Benoit. Son instinct et sa proximité naturelle à l'essence des problèmes m'a profondément touché. J'espère d'avoir réussi à en arracher des brides.

Merci à tous les jeunes et moins jeunes que avec moi partagent les tribulations de la recherche instrumentale: Nicolas, Alessandro Junior, Johannes, Greg, Aurélien, Frédérique, Florence, Olivier, Martino, Laurence, Xavier, Jean-Paul, Florian R. et Florian K. et beaucoup d'autre belle personnes croisés pendant le parcours: Marco, Alicia, Alessia, Santiago, Dave, Pablo, Eduardo, José Alberto, Guilaine, et beaucoup d'autres.

Au fond, à la fin, ce qui est le plus important, ce sont les moments de difficulté et de bonheurs qu'on a partagé ensemble: quand on fait exploser une tête de pulse tube, quand on arrive à réparer une fuite qui nous bloque depuis des moins ou bien quand on fait marcher un instrument après l'avoir monté au plan focal d'un télescope...

Mais, au cœur des choses, il y a eaux: Marghe, Amalia, Vincenzo, Santiago .... et toute ma famille. Je vous aime.

Andrea Catalano
10-09-2019

Contents

Introduction

The field in which I have worked extensively is experimental cosmology and more generally, experimental millimetre and sub-millimetre science. As many scientists say, for the past few decades, we have been living in the era of precision cosmology. This happened particularly due to the technological improvements of the instruments used to observe the distant galaxies and the Cosmic Microwave Background (CMB). It is nevertheless necessary to stress that the word *precision* is motivated by the fact that the final precision depends only on the sensitivity of the instrument rather than the difficulty of interpreting the results. In fact, the simplicity of the physical cosmological model makes the interpretation of the data straightforward. Nevertheless, despite the fact that the Big Bang theory is characterized by a small number of free parameters at early times (the standard ΛCDM model is based on only six parameters), describing the complexity of the present Universe would require an enormous number of parameters. This is why cosmologists during the last two decades concentrated their efforts in describing the universe at early times rather than trying to understand the evolution and the origin of the Universe starting from present time. Some scientists (see for example [Eisenstein et al.(1999)]) conclude that precision cosmology is essentially a χ^2-based cosmology. Parameter estimation requires two conditions being fulfilled: the data set must be free from systematic errors, and the fitted model must be physically correct. In our cosmology, it may be that the fitted data are not clean enough, and that a different set of physical laws applied to a different cosmology would fit the same data set equally well. For this reason, an appropriate set of tests must be identified and performed to verify the basic hypotheses. These tests have to be model-independent. That is, independent of the values of the cosmological parameters involved. A very important source of model-independent tests is the CMB and in particular its primary and secondary anisotropies [Peebles (1995)]. During the last decade, CMB observations from space (most recently by the European Space Agency's Planck satellite [Planck Collaboration et al.(2019)]) have significantly increased our understanding of the standard model of cosmology, allowing percent constraints on the cosmological parameters. Nonetheless, the current model remains deeply unsatisfactory. The nature of dark energy and dark matter is still unknown. The current expansion rate (H_0) of the Universe measured using the cosmic distance ladder and time delay of gravitationally lensed quasars is discrepant at the 5 σ level with the one inferred from observations of the early Universe. The amplitude of matter fluctuation (σ_8) measured from galaxy surveys is in tension with the one predicted from the CMB [Planck Collaboration et al.(2019)] (see Fig 1). Cosmology seems to be at the edge of a crisis, and one way to reveal new physics beyond the standard model is through the advent of the new generation spaceborne experiments and of high resolution ground based CMB telescopes.

The first generation of instruments devoted to CMB observations from space (COBE [Kogut et al.(1996)], WMAP [Bennett et al.(2013)], Planck [Planck Collaboration et al.(2019)]) and ground-based (BOOMERanG , MAXIMA, Archeops, Dasi, QUaD, ACT, POLARBEAR, BICEP to cite some of the most prominent experiments) permitted increased precision. In particular, the last space-borne experiment, Planck, after 5 full sky surveys has shown the best full sky picture of the primordial Universe in temperature and in polarisation. It has uncovered a wide range of new systematic effects revealed by the exceptionally high sensitivity of the bolometers mounted in High Frequency Instrument (HFI). Incredibly, even with these wonderful polarisation CMB maps, Planck mission was not conceived as the ultimate instrument for CMB polarisation measurements,

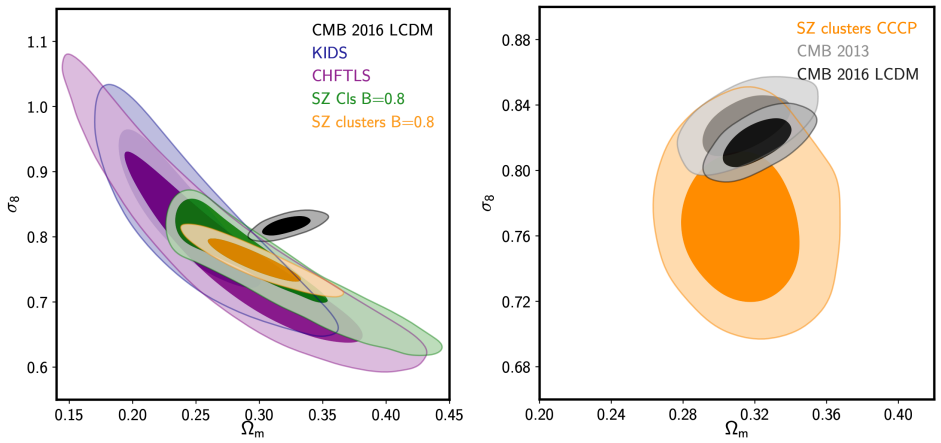

Figure 1: Left: recent large scale constraints compared with CMB (black filled contours). See text for references. Right: Comparison of SZ cluster constraints from Planck (yellow) with CCCP prior on the mass bias and Planck CMB constraints from 2013 and 2016 (grey and black respectively) [Douspis et al.(2019)].

and therefore Planck satellite could only place an upper limit on B-modes detection, the missing observational proof for the cosmic inflation theory.

The next generation of experiments therefore must not only achieve higher precision and make an unambiguous detection of inflationary B-modes, but eventually also precisely measure the distortion of the CMB spectrum which is becoming an important and complementary tool; the distortions are produced from the out-of-equilibrium energy exchange between matter and radiation before the last scattering surface and through the inverse Compton scattering by high-energy electrons in galaxy clusters. In the latter case, the low-energy CMB photons receive an overall energy boost during collisions with the high-energy cluster electrons (Sunyaev–Zel'dovich effect). Based on these scientific motivations, several ground-based experiments such as ACT [Salatino(2017)], BICEP3/Keck Array [Bischoff(2018)], SPT [Pan(2019)] and Polar Bear [Lee et al. 2008] have been deployed, and future ground-based CMB Stage-4 experiments [Keating(2019)], Simons Observatory [Ade et al. (2019)] and space mission LiteBIRD [Lee et al.(2019)] have been proposed. Current experiments have a focal plane on the order of 10,000 detectors which improves the Noise Equivalent Power by at least one order of magnitude in comparison to that of the first generation precision cosmology experiments.

My work fits in this context: I am involved in preparing the next generation of CMB experiments. In particular: detecting CMB B-mode polarization with an experiment that is currently in discussion to join the S4 network, studying the Sunyaev Zel'dovich effect through the NIKA 2 and the KISS spectro-interferometer and, in the near future, the CONCERTO spectro-interferometer, and finally, understanding foregrounds from dust emission by studying high frequencies instruments for balloon and space applications. Additionally, my work focuses on the development of a new generation of cryogenics detectors KID (Kinetic Inductance Detectors, their photometric validation, annex instrumentation and the scientific calibration.

KIDs are high-quality microwave resonators that have a change in their electromagnetic properties in response to incoming radiation. The resonator is a superconductor which absorbs photons

exceeding its gap energy, resulting in Cooper pairs breaking and thus, a change in the ratio of paired and unpaired (quasi-particles) charge carriers.

This document does not go into the detail of KID theory because a lot of very useful reviews already exist. We suggest for example [Doyle et al.(2010), Day et al.(2003), Zmuidzinas et al.(2012)]. In Chapter 2 we will present a mini-review of KIDs focusing in the way that they are used in millimere astrophysics.

This document will summarise my work accomplished and currently in progress, within the context of the CMB field.

Bibliography

[Eisenstein et al.(1999)] Eisenstein, D. J., Hu, W., and Tegmark,M. 1999, Astrophysical Journal, 518:2–23

[Peebles (1995)] Peebles, J.P.E., 1995, Space Science Reviews, 72, 680

[Planck Collaboration et al.(2019)] Planck Collaboration, Aghanim, N., Akrami, Y., et al. 2019, arXiv e-prints, arXiv:1907.12875

[Kogut et al.(1996)] Kogut, A., Banday, A. J., Bennett, C. L., et al. 1996, Astrophysical Journal, 470, 653

[Bennett et al.(2013)] Bennett, C. L., Larson, D., Weiland, J. L., et al. 2013, Astrophysical Journal, Supplement, 208, 20

[Douspis et al.(2019)] Douspis, M., Salvati, L., & Aghanim, N. 2019, arXiv e-prints, arXiv:1901.05289

[Salatino(2017)] Salatino, M. 2017, IEEE Transactions on Applied Superconductivity, 27, E1

[Keating(2019)] Keating, B. 2019, APS April Meeting Abstracts 2019, Q12.003

[Bischoff(2018)] Bischoff, C. A. 2018, Fourteenth Marcel Grossmann Meeting - MG14, 2079

[Lee et al. 2008] Lee A. T., Tran H., Ade P., et al.,2008,AIPC, 1040,66

[Pan(2019)] Pan, Z. 2019, American Astronomical Society Meeting Abstracts #233 233, 343.01

[Ade et al. (2019)] Ade, Peter et al., 2019, Journal of Cosmology and Astroparticle Physics, 02, 056–056

[Lee et al.(2019)] Lee, A., Ade, P. A. R., Akiba, Y., et al. 2019, Bulletin of the AAS 51, 286

[Day et al.(2003)] Day, P. K., LeDuc, H. G., Mazin, B. A., et al. 2003, Nature, 425, 817

[Doyle et al.(2010)] Doyle, S., Mauskopf, P., Zhang, J., et al. 2010, Proceedings of the SPIE, 77410M

[Zmuidzinas et al.(2012)] Zmuidzinas, J. 2012, Annual Review of Condensed Matter Physics, 3, 169

1 The Early Universe

The Birth of Modern Cosmology

Cosmology is the astrophysical study of the origin, structure, composition and evolution of the Universe.

All types of people from prehistory to present day have wondered why there is something instead of nothing in the universe, and when and where the first object formed. The technological challenge in answering these questions during past centuries has been too great to provide all but a purely philosophical argument.

The birth of a *Scientific Cosmology*[1] could be considered to arise from the work of Alexander Friedmann in 1922 [A.A. Friedmann (1922)] on the cosmological solution of General Relativity for an isotropic and homogeneous universe. From then to the 1950s, many improvements and some observations have been made to modify and correct this model into a satisfactory representation of our reality. This mathematical framework is based on four principles and a set of equations:

The Dicke Principle: Gravity is a metric phenomenon and the geometry of the Universe is determined by its matter and energy contents;

The Newtonian Paradigm of Dimensions: We live in a universe with three space-like and one time-like dimensions;

The Conditional Cosmological Principle: The Universe is isotropic. If space is analytic, then isotropy implies homogeneity[2];

The Fluidity Principle: The Universe is filled by one or more ideal fluids (such as a perfect gas) governed by a simple equation of state: $P = \omega\rho$ where the *state parameter* ω is a function of time only, P and ρ are the pressure and energy density of the fluid, and the speed of light $c = 1$;

The Einstein Field Equations: The equations of General Relativity relate the properties of the cosmic fluids to that of the space-time geometry;

[1] Considering as *Scientific* a speculation following the Galilean scientific method

[2] The term *conditional* takes into account the possibility of a fractal Universe which can be isotropic but not homogeneous.

$$R_{\mu\nu} - \frac{1}{2} g_{\mu\nu} R - \Lambda g_{\mu\nu} = 8\pi G T_{\mu\nu} \tag{1.1}$$

where $g_{\mu\nu}$ is the metric, $T_{\mu\nu} = diag(\rho, p, p, p)$ is the momentum-energy tensor, ρ is the energy density, p is the pressure of the fluid and $R_{\mu\nu}$ is the Riemann tensor (and R its related scalar) and Λ is a component, as Einstein originally included in his formulation of general relativity, called the *cosmological constant*, which is not diluted with the expansion of the universe. The Riemann tensor depends on the second derivatives of the metric and contains information about the considered space curvature.

In general, under the assumptions of homogeneity and isotropy along with the first two principles, we can obtain the Friedmann-Robertson-Walker metric which can be expressed as:

$$d^2 s = d^2 t - a^2(t)[\frac{d^2 r}{1 - kr^2} + r^2(d^2\theta + \sin^2\theta d^2\varphi)] \tag{1.2}$$

in polar coordinates (r,θ,ϕ), where $k = 0,\pm 1$ and fixes the space-time metric, and $a(t)$ is the time (t) dependent scale factor.

At the beginning of the 1950s, George Gamow, by interpreting Hubble's observations [E. Hubble (1929)] of the recession of galaxies[3], added physics to the model of Mathematical Cosmology, by which the primordial Universe was in a phase of high temperature allowing the systhesis of light elements (H, He-4, He-3, D, Li, Be) [G. Gamow (1946)]. This new idea was called *Big Bang* Cosmology by Fred Hoyle and opened the era of *Modern Cosmology*.
Filling the metric in the general relativity equation, we obtain the dynamic equation for a homogeneous and isotropic Universe (Friedmann equations):

$$\left(\frac{\dot{a}}{a}\right)^2 = \frac{8G\pi}{3}\rho - \frac{k}{a^2} + \frac{\Lambda}{3} \tag{1.3}$$

$$\frac{\ddot{a}}{a} = -\frac{4\pi}{3} G(\rho + 3p) + \frac{\Lambda}{3} \tag{1.4}$$

where $\dot{a} = Ha$ is the *Hubble Law* (in its linearised form).

The scale factor behaves differently for matter and radiation: in the case of matter, the number of particles is preserved so the energy density decreases as $\frac{1}{R^3}$ [4]. For radiation (photons and massless neutrinos), the energy density scales as $\frac{1}{R^4}$[5].

In order to solve the Friedmann equations, we have to specify the matter density of the Universe. The Friedmann equations then become:

$$\left(\frac{da}{adt}\right)^2 = H_0^2[\Omega_{R_0}(\frac{a_0}{a(t)})^4 + \Omega_{M_0}(\frac{a_0}{a(t)})^3 + (1 - \Omega_0)(\frac{a_0}{a(t)})^2 + \Omega_\Lambda] \tag{1.5}$$

where $\Omega_0 = \Omega_{R_0} + \Omega_{M_0} + \Omega_\Lambda = \frac{\rho}{\rho_c}$ and ρ_c is the critical density at which the expansion (of the universe) is constant.

For these reasons the history of the Universe is roughly divided in three eras [Padmanabhan (1993)]: the *radiation-dominated era*, the *matter-dominated era* and the *dark energy-dominated*

[3] This shift in observed frequency from the emitted frequency, called $redshift$, is proportional to the distance to the galaxies and indicates the expansion of the Universe.

[4] $R \equiv \chi a(t)$ is the product between the comoving distance χ and the scale factor parameter $a(t)$.

[5] The radiation energy density decreases for two reasons: a factor of $\frac{1}{R^3}$ (as for matter) and another factor of $\frac{1}{R}$ due to the wavelength stretching.

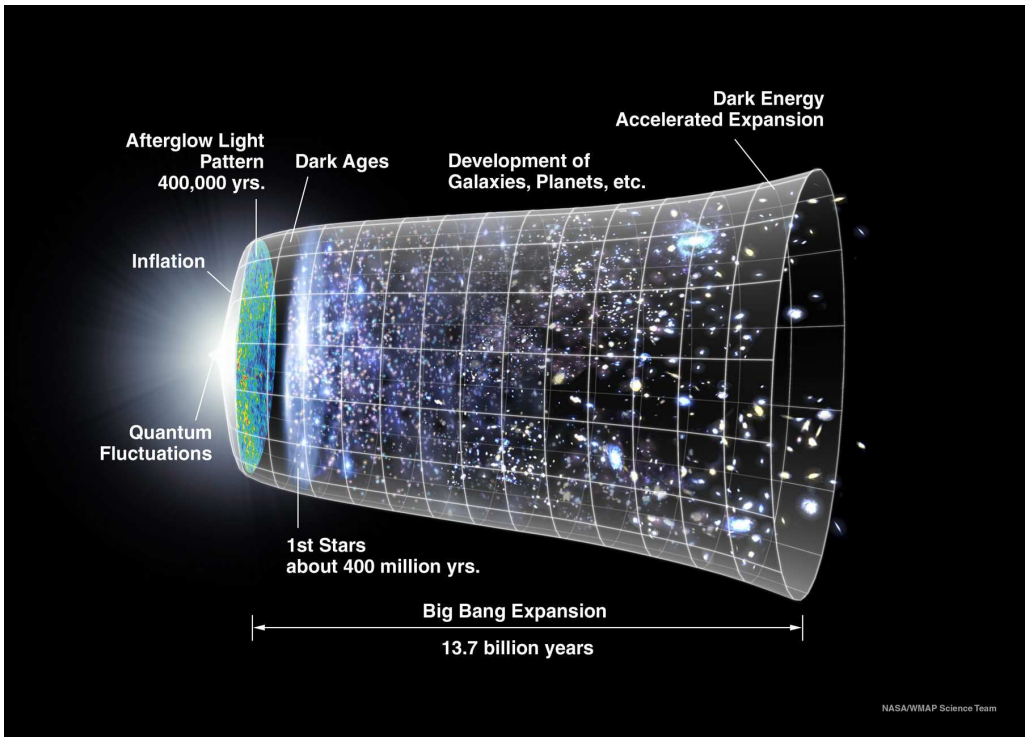

Figure 1.1: Events in the history of the Universe as it evolved from the Big Bang (http://www.jwst.nasa.gov/firstlight.html).

era. The radiation-dominated era occurred during the first 10^5 years of the universe. At the beginning of the radiation-dominated era, a few minutes after the initial singularity, the temperature and the baryonic density of the Universe were high enough to allow the nucleosynthesis of light elements to take place. At earlier times, current theories suggest that the Universe underwent a phase of accelerated expansion, known as *inflation* [Guth (1980)]. At redshift $z \sim 1100$, radiation de-coupled from matter (de-coupling era). This is known as the surface of last scattering (LSS) in which the photons were de-coupled from the matter and were free to move in a transparent Universe, which became the present day Cosmic Microwave Background (CMB) radiation. The Big Bang model was strongly supported by the discovery of CMB in 1965 by Arno Penzias and Robert Wilson [Penzias (1965)]. This discovery proved that the Universe at very large scale is isotropic and homogeneous.

1.1 The Cosmic Microwave Background

The evolution of the Universe as it has been presented in the last section, is essentially a thermal history because it is determined by the mean energy of the photons through the different epochs and consequently their different interactions with matter.

The expansion of the Universe is an adiabatic process[6] in which the temperature decreases as $T \propto a(t)^{-1}$. Before redshift $z \sim 1100$ the temperature of the Universe was such that protons

[6]We neglect exothermic matter processes such as electron-positron annihilations. In these cases the temperature increases but not the a parameter.

and electrons were de-coupled and free to move in a primordial plasma. Compton scattering of electrons, which are in turn tied to the protons through Coulomb interactions, strongly coupled photons to baryons and establishes a photon-baryon fluid.

Photon pressure resisted compression of the fluid due to gravitational infall and these two competing forces set up acoustic oscillations. During this epoch, the temperature fell low enough for electrons and protons to recombine and the photon Compton cross-section with electrons decreased rapidly. At redshift $z \sim 1100$, this recombination produced neutral hydrogen, allowing photons to free stream. Regions of compression and rarefaction at this epoch represent hot and cold spots respectively in the CMB. Photons might also be gravitational redshifted from climbing out of the potentials on the last scattering surface. The resultant fluctuations appear to the observer today as anisotropies in the CMB [Hu et al. 1994].

Since CMB is projected onto the sky, it is conventional to develop the sky maps in coordinates with spherical harmonics Y as:

$$\frac{\Delta T}{T_0} = \sum_{l=2}^{\infty} \sum_{m=-l}^{+l} a_{lm}^T Y_{lm}^T(\theta, \varphi) \tag{1.6}$$

where the coefficients a_{lm} are random variables with an average equal to zero. A single spherical harmonic Y_{lm} corresponds to angular variations of $\delta \sim \pi/l$.

The following describes in more detail the different components of these anisotropies:

- **The Monopole ($l = 0$):** The Last Scattering Surface (LSS) epoch corresponds to a temperature of about 3000 K which means, in relation to the standard scaling with the a parameter, $T_{CMB}^{Now} = T_{CMB}^{LSS}/(1+z)$, we expect that our present Universe is permeated by a radiation of a blackbody at a temperature of about $T = 2.72$. All viable cosmological models predict a very nearly Planckian spectrum to within the current observational limits. The CMB mean temperature has been measured equal to 2.7255 $\pm$ 0.0006 K (1σ) [Fixen (2009)] with a number density $n_\gamma \sim 411$ cm^{-3}, and a fraction of the critical density $\Omega_\gamma \sim 5.38 \times 10^{-5}$
- **The Dipole:** The most visible anisotropy is the one corresponding to the dipole (l=1) which

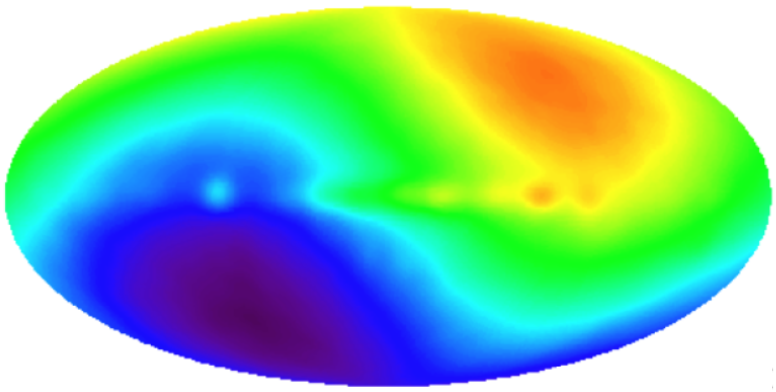

Figure 1.2: CMB dipole maps from FIRAS. [Fixen (2009)]

is associated to the peculiar motion of the observer with respect to the local cosmological rest frame. The motion of an observer produces a Lorentz-boosted temperature pattern:

$$T \sim T_0(1+\beta\cos\theta+...) \tag{1.7}$$

where T_0 is the mean temperature of the CMB over the sky, $\beta = v/c$ is the velocity of the observer with respect to the LSS at redshift $z = 1100$, and θ is the angle between the direction of observation and that of motion. This fluctuation has been precisely measured by Planck satellite as a fluctuation of 3.3645 ± 0.0020 mK [Planck Collab (2016)] with a direction (in galactic coordinates) of $l = 264.4$ and $b = 48.4$.

The kinetic explanation of the dipole comes from a peculiar velocity of the observer, which can be explained only as the result of a gravitational acceleration integrated in time. We know that the local group of galaxies has a peculiar velocity with respect to LSS. From the COBE measurements [A. Kogut (1993)], we find $v_{LG} = 627 \pm 22$ toward $l = 276 \pm 3$ and $b = 30 \pm 3$ degrees.

The dipole is largely used as a calibration for mapping experiments, using the variation in time of the orbital motion of the Earth, and/or a comparison to the cosmological dipole measured by satellite experiments.

- **High-Orders Multipoles:**

  At higher multipoles ($l \geq 2$), the anisotropies are generated by the perturbations in the density of the early Universe, at the epoch of the last scattering. For Gaussian fluctuations (no correlations between the modes), the statistical content is encapsulated in the two points temperature correlation function, or equivalently, its angular decomposition into Legendre moments C_l.

$$\left\langle \left(\frac{\Delta T}{T_0}\right)^2 \right\rangle = \frac{1}{4\pi}\sum_{l=1}^{\infty}(2l+1)C_l^{TT} \tag{1.8}$$

  where we set:

$$\langle a_{lm}^T \cdot a_{l'm'}^T \rangle = C_l^{TT}\delta_{ll'}\delta_{mm'} \tag{1.9}$$

  From recent observations of Planck Satellite, the hypothesis of Gaussianity seems to work extremely well overall. Nevertheless we caution here that there is some indications of non-Gaussianity presented as weak signatures at large scales, seen in Planck data [planck collab. (2014)]. This deviation does not to be significant enough to reject the original assumption.

  The anisotropies at $l \geq 2$ results mostly from density fluctuations in the primordial plasma when radiation and matter were tightly coupled. Density nonuniformities led to differences in gravitational potential: if photons "climbed out" of a potential well to reach us, they became redshifted (and vice versa). This caused a decrease the observed temperature (gravitational potential redshift) from the particular location on the sky. We can distinguish four different regions in the power spectrum of the CMB as shown in Fig.1.3: in the region where $l < 100$, anisotropies have scales larger than the horizon at the LSS (which is around $l \sim 100$), therefore they cannot evolve. In this case, anisotropies reflect the intrinsic temperature fluctuation on the initial conditions at recombination and the gravitational redshift. This results into a constant spectrum and which is known as Sachs-Wolfe plateau for $10 < l < 100$. If $l < 10$, time variation of the potentials makes the lowest l rise above the plateau (*integrated Sachs-Wolfe effect*).

  In the region where $100 < l < 1000$ (on the order of one degree on the sky or less), the anisotropies are inside the horizon scale. These are driven by acustic oscillations of the photon-baryon fluid of the primordial plasma. At the decoupling, the oscillations were

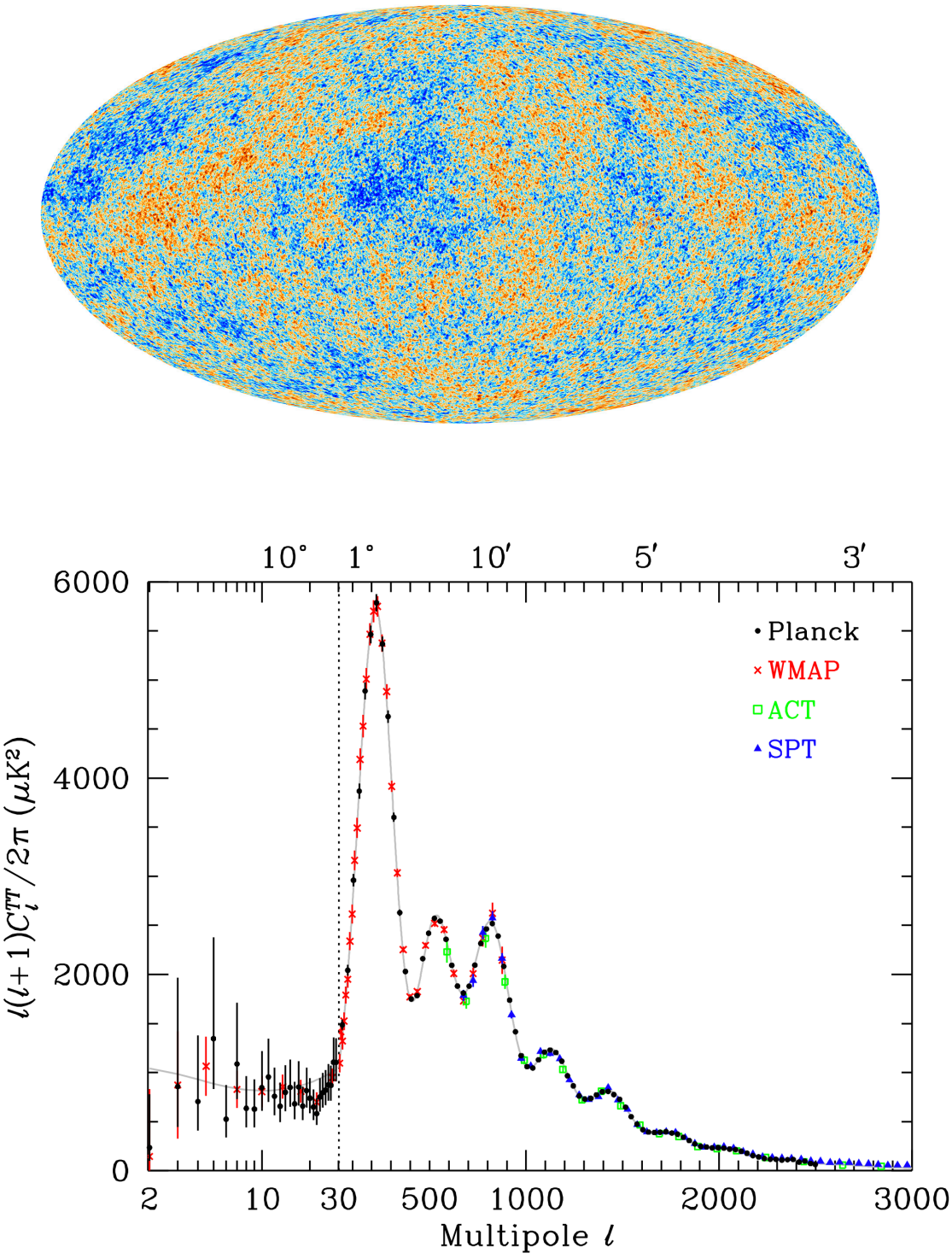

Figure 1.3: CMB temperature map of anisotropies seen by Planck (top panel). Bottom panel: CMB power spectrum of the CMB anisotropies made with results from the Planck, WMAP, ACT, and SPT experiments. The curve plotted is the best-fit ΛCDM model to Planck data [Scott 2016, Planck Collab 2015, Hinshaw et al. 2013, Swetz et al. 2011, Calstron et al. 2011].

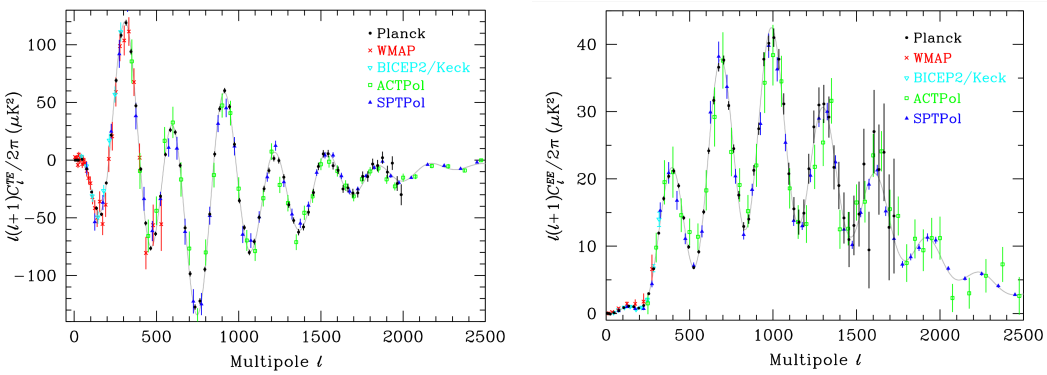

Figure 1.4: Cross-power spectrum TE (Left panel) and power spectrum of E-modes polarization (right panel) from Planck, WMAP, BICEP2/Keck, ACTPol, and SPTPol [Scott 2016, Planck Collab 2015, Hinshaw et al. 2013, Swetz et al. 2011, Calstron et al. 2011]

frozen-in, and became projected on the sky as a harmonic series of peaks in the power spectrum. This can be understood as a frozen image of a random standing wave: the main peak represents the maximum compression with a mode shifted by $\pi/4$[7]. The even peaks represent maximal under-densities. The physics and the interpretation of the measurements behind this region of CMB anisotropies are straightforward, therefore it is possible to directly link them to the cosmological parameters. In addition, this interpretation has been confirmed by the detection of oscillations in the baryon component of the power spectrum of near galaxies [Eisenstein (2005)].

In the region where $l > 1000$ the anisotropies scales become smaller than the diffusion scale of the travelling photons. This diffusion damps the anisotropies at these scales (*damping tail region*).

In Fig. 1.3, the most recent constraints on the CMB anisotropies are presented. To date, it seems evident that in term of temperature anisotropies, the systematic effects are under control. On the other hand, this is not completely the case for the other part of informations that can be taken from CMB observations: the polarisation anisotropies. Let us describe quickly what they are.

- **CMB Polarisation:**

  Thomson scattering of the photons off free electrons generates linear polarisation expected at a level of about 5 % with respect to the temperature anisotropies. Therefore, if the primordial fluctuations are partially polarised at last scattering, they would polarise the CMB anisotropies for present observers [Hu-White (1997)].

  Temperature perturbations have three geometrically distinct sources: the scalar (compressional), vector (vortical) and tensor (gravitational wave) perturbations. Each source of perturbation leads to different patterns of polarisations: the scalar perturbations represent perturbations in the density of the primordial plasma at LSS and are the only fluctuations which can form structure through gravitational instability. Vector perturbations represent the vortical motions of matter. There is no associated density perturbation and the vorticity

[7] Each mode of the spherical harmonics is independent and it represents a mode of a $\pi/2$ out of phase harmonic oscillator with amplitude reduced by the sound speed.

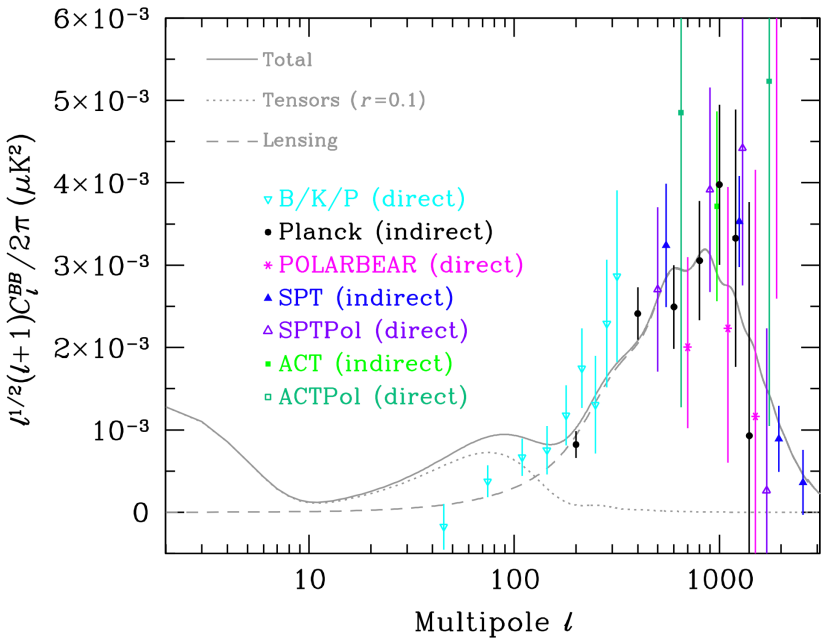

Figure 1.5: Power spectrum of B-mode polarization including combined analysis between BICEP2/Keck Array/Planck (B/K/P) [Planck Collab. (2015)]

is damped by the expansion of the Universe as are all motions that are not enhanced by gravity. Tensor fluctuations are transverse perturbations to the metric, which can be viewed as gravitational waves. A plane gravitational wave perturbation represents a quadrupolar stretching of space in the plane of the perturbation.

An intuitive geometrical way to decompose polarisation is into two parts: a 'divergent' mode (*E-mode*) with axes oriented in the same orientation as the polarization and a 'curl' mode (*B-mode*) where the pattern can be thought of as a 45 deg rotation of the E-mode pattern. Density perturbations only induces parallel polarisation and so generate only E-mode polarisation. Gravitational waves generate both and so have a component of B-mode polarisation. Therefore, a detection of B-mode polarisation would be a clear evidence of gravitational waves.

Using *E-modes* and *B-modes*, we can expand the polarisation pattern in spherical harmonics as we have done for temperature anisotropies. We obtain:

$$\frac{P_{(ab)}}{T_0}(\theta,\varphi) = \sum_{l=2}^{\infty}\sum_{m=-l}^{l}\left[a^E_{lm}Y^E_{lm(ab)}(\theta,\varphi) + a^B_{lm}Y^B_{lm(ab)}(\theta,\varphi)\right] \tag{1.10}$$

From Eq. 1.10 it is possible to deduce five different spectra:

$$\langle a^E_{lm}\cdot a^E_{lm}\rangle = C^{EE}_l\delta_{ll'}\delta_{mm'} \tag{1.11}$$

$$\langle a^B_{lm}\cdot a^B_{lm}\rangle = C^{BB}_l\delta_{ll'}\delta_{mm'} \tag{1.12}$$

$$\langle a^T_{lm}\cdot a^E_{lm}\rangle = C^{TE}_l\delta_{ll'}\delta_{mm'} \tag{1.13}$$

$$\langle a^T_{lm}\cdot a^B_{lm}\rangle = C^{TB}_l\delta_{ll'}\delta_{mm'} \tag{1.14}$$

$$\langle a^E_{lm}\cdot a^B_{lm}\rangle = C^{EB}_l\delta_{ll'}\delta_{mm'} \tag{1.15}$$

Due to their origin, temperature fluctuations are expected to be well correlated with *E-modes* while *B-modes* power spectrum is expected to be not correlated with temperature. Observations provide important tools for reconstructing the model of the fluctuations from the observed power spectrum because different sources of temperature anisotropy (scalar, vector and tensor) give rise to different patterns in polarisation. Thus, by including polarisation information, one can provides information complementary to the temperature power spectrum. In addition, the polarisation spectrum is sensitive to the presence of gravitational waves at a wider angular scale range than the temperature spectrum. Indeed, inflationary theory predicts the existence of a stochastic gravitational-wave background with a nearly scale-invariant spectrum. CMB polarisation would thus allow a way to study the inflationary model and to understand the primordial plasma before the LSS.

The cross $T-E$ and the $E-E$ power spectra have been measured and mapped by different experiments but the ultimate observation was performed by Planck (see Fig.1.4). These observations confirm that the polarisation is due to Thomson scattering at z $\sim$ 1100.

On the other hand, the $B-B$ power spectrum is expected to be very small and therefore this observation is extremely challenging. Even combined analysis of different experiments as plotted in Fig.1.5, the B-modes seem to be only marginally detected. For this reason and the theoretical implications, this measurement is becoming a *Holy Grail* of the coming years of experimental cosmology and several ground-based and proposed next-generation satellites are focused on making this detection.

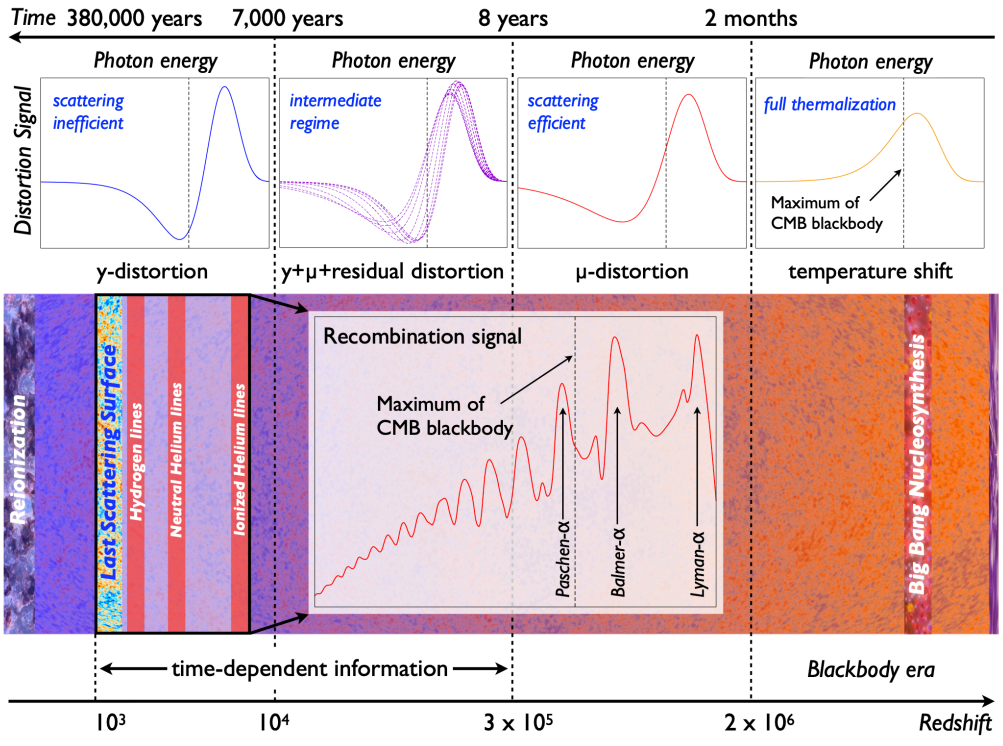

Figure 1.6: Evolution of spectral distortions across time [Chluba et al. 2019].

1.2 Spectral Distortion of the CMB

All mapping experiments cited previously involve differential measurements, therefore they are insensitive to the average level of temperature; only the COBE satellite was able to observe the sky to an absolute temperature, via the FIRAS instrument [Mather (1999)]. FIRAS measured the temperature of the CMB compared with a blackbody to a precision of 10^{-4} over three decades in frequencies. Twenty-five years after this beautiful result, it still represents the best measurement we have. However it would be very interesting to improve the data of the CMB monopole spectrum: more sensitive measurements should reveal small deviations from a blackbody. This would result from out-of-equilibrium energy exchange between matter and radiation via Compton scattering. Indeed, any physical process that could inject energy into the universe should have distorted this spectrum (for example dark matter particles that annihilate or decay) [Chluba et al. 2019]. At very early time (couple of decades after the Big Bang when $z > 5 \cdot 10^4$), the Universe was so dense such that Compton scattering was very efficient. Any process producing energy would affect all of the CMB photons, creating a chemical potential distortion in the blackbody spectrum (μ-distortion). A μ-distortion cannot be generated at recent epochs and thus directly probes events in the pre-recombination era. When $z < 5 \cdot 10^4$, Compton scattering becomes inefficient enough that any injections of energy would be felt by only a fraction of CMB photons, producing what are called y-distortions in the spectrum (see Fig.1.6). This y-type distortion probes the thermal history during recombination and reionization up to the most recent Universe via The Sunyaev-Zel'dovich (SZ) effect (detail of the SZ effect are given in the next section).

After more than a decade of beautiful observations CMB temperature and polarisation anisotropies, today, thanks to the technological advances, new generations of instruments have the potential to improve the constraints on energy released in the early Universe and therefore probe spectral distortion mechanisms and eventually detect the residual lines from the cosmological recombination of hydrogen and helium (see Fig.1.7). This could open an exciting new window to early Universe physics.

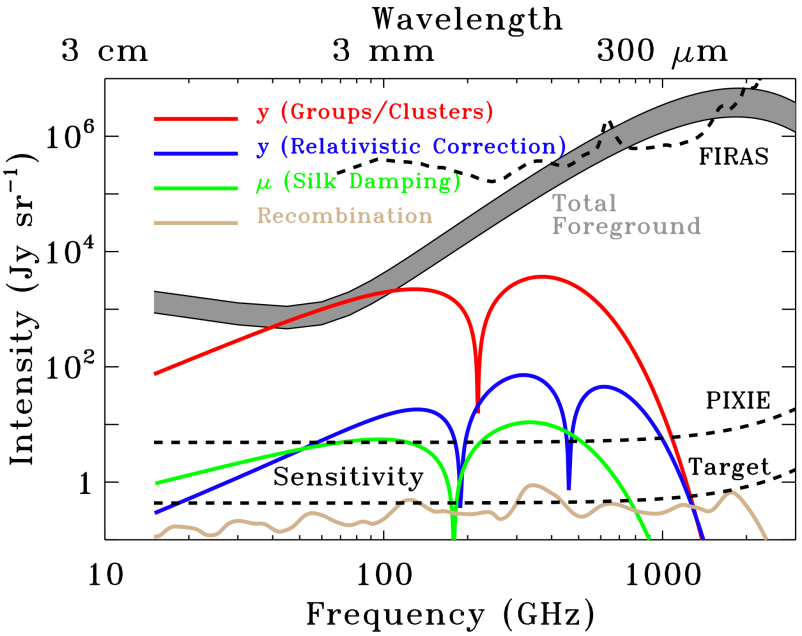

Figure 1.7: Different components of CMB spectral distortion compared to sensitivity of FIRAS, proposed experiment PIXIE (not funded) and new targets for new experiments proposed (PRISTINE, Super-PIXIE [Aghanim (2019), Kogut (2019)])

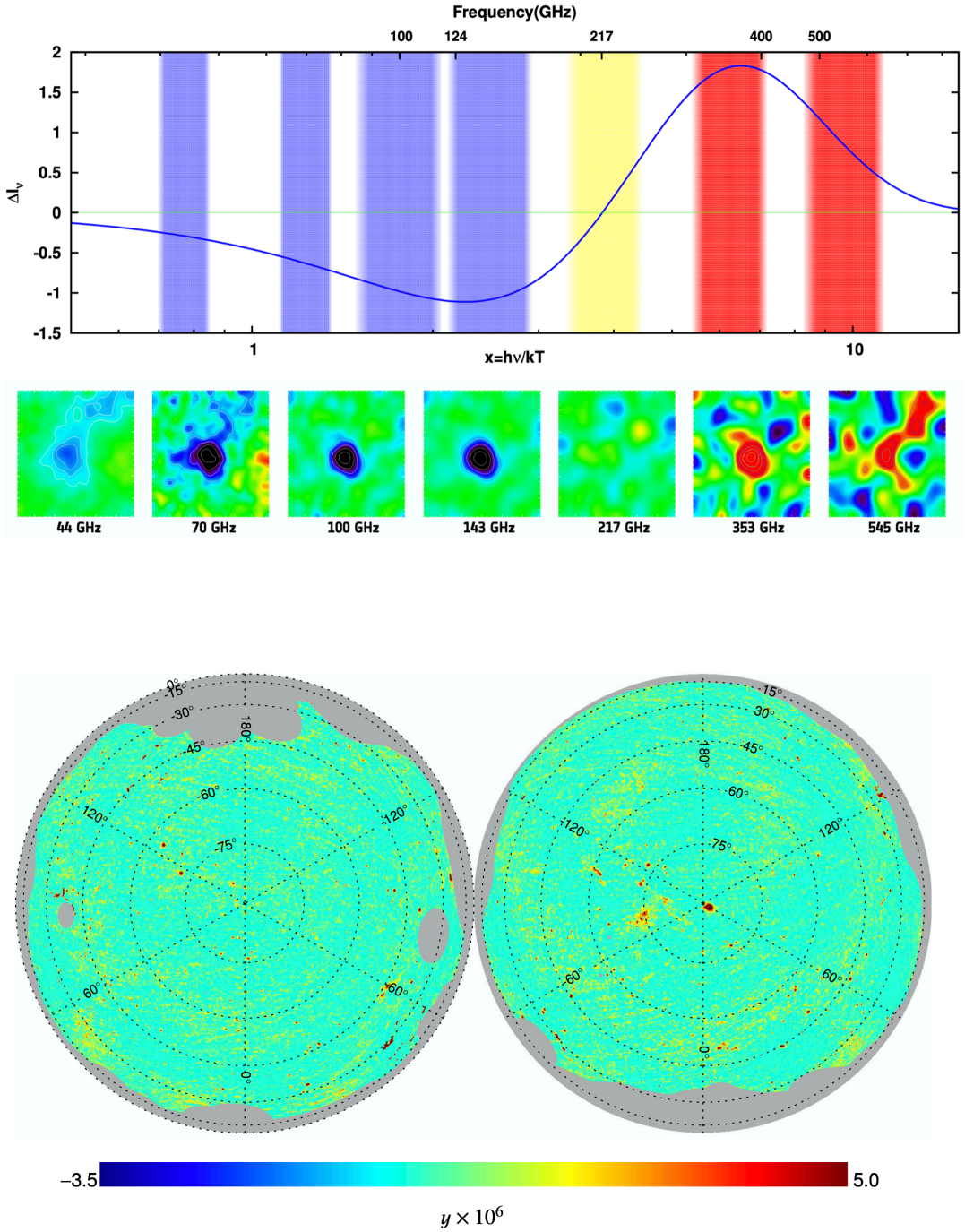

Figure 1.8: Top Panel: thermal SZ effect from cluster Abell 2319 seen by different channel of Planck. Bottom Panel: Reconstructed all sky Compton parameter map in orthographic projection [Planck Collab. 2016] using the MILCA algorithm [Hurier et al. 2013].

1.2.1 Spectral Distortion from Secondary Anisotropies: the Sunyaev-Zeldovich Effect

An additional spectral distortion of CMB which is commonly considered as a secondary anisotropy comes from the interaction of CMB photons with hot electron gas in the Universe at z $<<$ 1000 (of the order of unity). This effect is particular by important in galaxy clusters through which it possible to observe a partially Comptonized spectrum of CMB, resulting in a decrement at radio wavelengths and an increment in the submillimetre. This effect is known as the Sunayaev-Zel'dovich effect (SZ) [Sunyaev-Zeldovich (1980)]. In contrast to CMB primordial spectral distortions, a significant spectral distortion is associated with an anisotropic distribution on the sky, thanks to the SZ effect.

The SZ effect appears as an intensity decrease at frequencies lower than $\sim$ 217 GHz and an increase at higher frequencies (Fig 1.8). Due to its spectral signature, the thermal SZ effect can be separated from the primary CMB anisotropies by observing at several frequencies. Indeed, the variation in temperature produced by the SZ effect results:

$$\Delta T/T = y \cdot f(x)$$

where the y-parameter represents the product between the integral of Thomson optical depth times kT_e/m_ec^2 through the cluster, and $f(x) = x\coth x/2 - 4$ where $x = kT_e/m_ec^2$ for a gas not exceeding a temperature of few keV (non-relativistic gas). In addition to this *thermal* SZ effect, a smaller component known as the *kinetic* effect arises from the proper motion of the cluster gas, giving $\Delta T/T \sim \tau(v/c)$ (where τ is the Thomson optical depth), having the same spectrum as the primary CMB anisotropies.

The SZ effect recovers much astrophysical and cosmological information: first, since the effect is independent of redshift, it can be used to find cluster even out to large distances. With a potential big survey of clusters, this effect can be used to constraint cosmological parameters, such as the clustering amplitude σ_8 and the equation of state of the dark energy, by counting clusters detected as a function of redshift [Planck Collab. 2016].

Also, the SZ effect can be used to find and study individual clusters, combined with X-ray observations to obtain estimates of the Hubble constant.

Several experiments are doing cosmology studies observing cluster with the SZ effect. New generation ground-based instruments such as Simons Obervatory [Ade et al. (2019)] and CMB-Stage 4 [Keating(2019)] are aiming for medium angular resolution. For high angular resolution, the NIKA 2 SZ large program and other targeted observations, coupled with ancillary X-ray data, will allow an in-depth characterisation of the SZ-observable-mass relation that will be used to (re)-evaluate cluster-based cosmological constraints from past or ongoing/future SZ surveys.

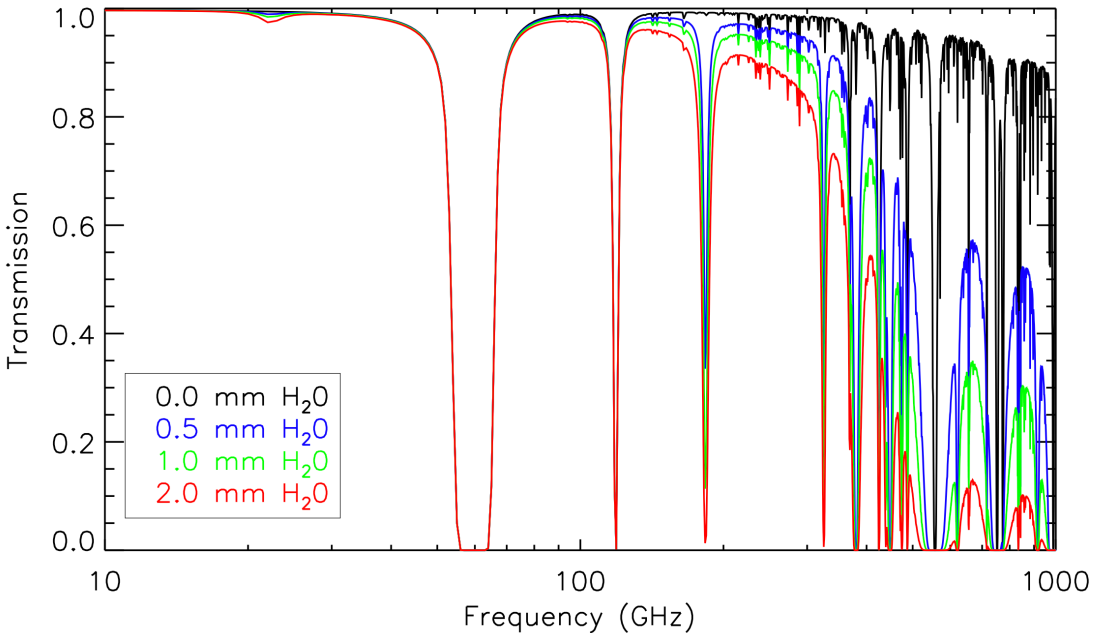

Figure 1.9: Atmospheric transmission at the Atacama desert for four different PWV amounts derived with the ATM model from [Pardo 2001]

1.3 Foregrounds

Foregrounds are all the astrophysical sources that cause spurious effects in the CMB observations. In the case of a ground-based experiments we have to deal with foregrounds coming from the atmosphere in addition to astrophysical foregrounds. Different components of foregrounds have spectral indices quite different for that of the CMB, making component separation possible thanks to multi-frequency observations. In addition, the total astrophysical foregrounds spectrum has a minimum around 100 GHz which corresponds closely to the peak of the CMB. At these frequencies therefore, the emission of astrophysical foregrounds corresponds typically to about 10 % of the CMB temperature anisotropies (for observations away from the galactic disk). In terms of polarisation, the polarised foregrounds are relatively brighter than that for temperature and therefore, separating the foregrounds from the CMB polarisation signal is more difficult.

Apart from the atmosphere, there are four main distinct astrophysical foregrounds in temperature (free-free, synchrotron, dust and spinning dust emissions), and two in polarisation (synchrotron and dust) [Dickinson 2016, Bouchet&Gispert 1999]. In Fig. 1.10 the contributions of different astrophysical foregrounds in temperature and in polarisation are presented as measured by the Planck Satellite.

- **Atmosphere :**

  At millimetre wavelengths, observations are possible with ground-based instruments because the atmosphere is partially transparent (see Fig.1.9). In this range of frequencies, absorption is mostly due to the water vapor except for an absorption line of oxygen around 60 GHz and 115 GHz. In addition, water vapour has absorption lines at 22, 183, 325, and 380 GHz. Therefore, spectrometers or photometers observing from the ground have only a few windows accessible for observations (below 50 GHz, and around 95, 150, 250 and at 340 GHz). Of course, the site has to be chosen carefully, since, particularly for high frequencies, the atmosphere must be very dry (precipitable water vapour - PWV of the order of 1 mm or less) and this happens only for very few sites over the World (e.g. the Atacama

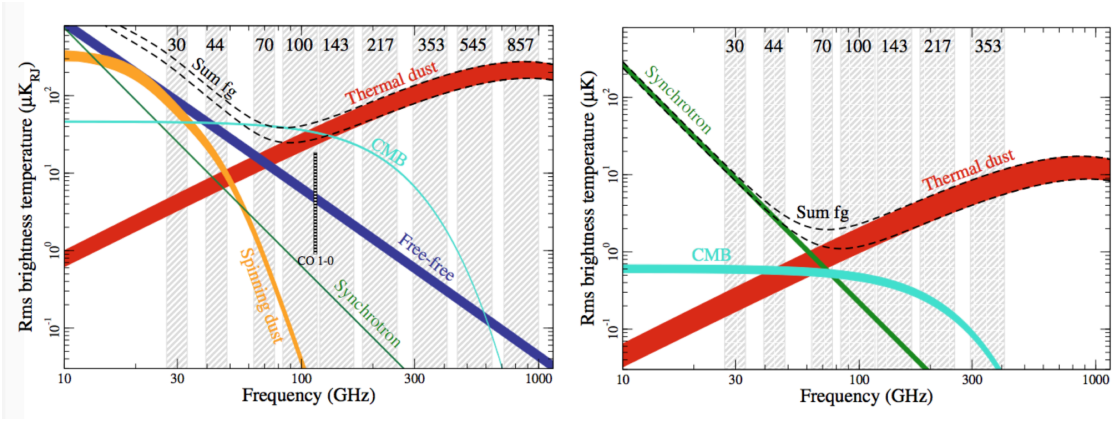

Figure 1.10: Spectral characteristics of the average fluctuation (on 1 degree scales over ~ 80 % of the sky) of foregrounds and CMB in temperature (left) and polarisation (right) [Planck 2018]. These estimates represent the average fluctuations.

desert and South Pole). The atmospheric emission is expected to be fully un-polarised. Nevertheless, due to its large emission relative to the CMB anisotropies, it can contribute to the polarisation leakage signal via instrumental systematic effects (detectors cross-pol, bandpass mismatch, imperfection of optical elements like half wave plates, etc....) [Errard 2015].

- **Free-Free Emission :** Thermal bremsstrahlung from an ionized hydrogen cloud (HII region) is often called free-free emission because it is produced by free electrons scattering off ions without being captured. The electrons are free before the interaction and remain free afterwards. The emission is proportional to [Planck 2014]:

$$T_{Br} \propto \nu^{-2.13} \tag{1.16}$$

  Free-free emission is intrinsically unpolarised but it can be partially polarised by Thomson scattering within the HII region. The emission is larger at low frequencies but it is not expected to be dominant for polarisation observations at any frequency.

- **Synchrotron Emission :** A charged particle moving in a magnetic field radiates energy. At non-relativistic velocities, this results in cyclotron radiation while at relativistic velocities it results in synchrotron radiation. Synchrotron radiation is typically generated by galaxies, where relativistic electrons spiral (and hence change velocity) through magnetic fields.

  The synchrotron emission follows the power law:

$$T_{synchro} \propto \nu^{\beta} \tag{1.17}$$

  where β is determined by the energy of electrons and the intensity of the magnetic field in the considered region. Planck has measured $\beta = -2.7 \pm 0.2$ [Planck 2016]

  This non-thermal radiation contains a percentage of polarised emission:

$$P = \frac{3\beta + 3}{3\beta + 1} \tag{1.18}$$

  The r.m.s. fluctuation of synchrotron emission corresponds to a change in temperature of about 50 μK. Synchrotron emission and its polarisation is the dominant source of foregrounds at frequencies lower than 100 GHz.

- **Dust Emission :** Dust emission is due to the thermal emission from grains and small particles in a local medium. Part of this emission is polarised by its local magnetic field which aligns elongated grains so that they spin with their long axes perpendicular to the field. Its radiation can be considered as a blackbody emission modified by opacity effects due to the interstellar dust grains having a typical temperatures of about 20 K.

  The observed electromagnetic spectrum is expressed as:

  $$T(\nu) \propto \nu^{\beta} \cdot B(\nu, T)$$

  where β has been measured by combined measurements by FIRAS and Planck equal to 1.6 [Planck 2016], $B(\nu, T)$ is the blackbody spectrum, and τ is the optical depth.

  At low galactic latitudes, thermal emission from dust particles dominates the IR spectrum. In general, depending on the shape and the alignment of dust particles, emission from dust can be polarised from 2 % to 10 %. At frequencies higher than 200 GHz, dust is the dominant foreground for continuum and polarisation observations. For polarisation, this emission results in a linear polarisation that can be also used to measure the direction of the magnetic field.

- **Spinning-Dust Emission**

  Small interstellar dust grain and molecules ($\sim 10^{-9}$ m) can rotate at very high frequencies ($\sim$ GHz). If they have an electric dipole moment, they emit by electric dipole radiation [Draine 1998]. Observations have shown a good fit to a spinning dust spectrum with a typical peak frequency around 15-20 GHz for foregrounds. Theoretical works suggest that spinning dust is not highly polarised at frequencies above a few GHz [Draine 2016]. Measurements of the level of polarisation of spinning dust largely consist of upper limits at the level of a few percent.

Due to the different spectral indices (see Fig. 1.10), the minimum in the foreground polarisation, as with the temperature, is near 100 GHz. For full sky measurements, because synchrotron emission is more highly polarised than dust, the optimum frequency at which to measure intrinsic (CMB) polarisation is slightly higher than for anisotropy. Over any small region of the sky where one or more of the foregrounds is known a priori to be absent, the optimum frequency would clearly be different. However, as with anisotropy measurements, polarised foregrounds can be removed with multi-frequency coverage.

It also interesting to consider how the spatial as well as the frequency signature of the polarisation can be used to separate foregrounds. Using angular power spectra for the spatial properties of the foregrounds is a simple generalisation of methods already used in anisotropy work. For instance, in the case of synchrotron emission, if the spatial correlation in the polarisation follows that of the temperature itself, the relative contamination will decrease on smaller angular scales due to its diffuse nature. Furthermore, the peak of the cosmic signal in polarisation occurs at even smaller scales than for temperature anisotropy.

1.4 Status on CMB observations and perspectives

The review presented in this chapter shows that an enormous amount of cosmological information has been already extracted from the CMB. In Tab 1.11 the current status of our knowledge of cosmological parameters constraints is presented from the various CMB spectra, individually and

without CMB lensing, including a wider variety of derived parameters of physical interest [Planck Collab. 2018]). The overall picture is is one of remarkable consistency with the 6-parameter ΛCDM cosmology. However we can learn more, there is indeed a large amount of unexplored information about our Universe. A lot of activity in the coming years will continue to focus on CMB observations from ground-based experiment and potentially from space.

Of course, a part of the job will be to determine cosmological parameters with increasing precision. This is very important in order to improve the consistency between predictions of the standard model but also to solve inconsistencies between combined observations of the early and the next Universe (see for example Fig.1).

A second area of interest will be mapping dark energy with galaxy clusters, using the spectral distortions of the CMB frequency spectrum by the Sunyaev-Zeldovich effect [Bolliet et al. 2018]. This will map the density of galaxy clusters as a function of redshift and thus establish powerful constraints on the evolution of the Universe during precisely when dark energy begin to dominate. Although the constaints given by the SZ are probably not competitive with BAO. Notice that clusters are expected to be found mainly between redshift of 0-2 with a peak at about 1. Dark energy dominates at much later times.

Last but not least, the next generation of experiments primarily aims to identify the tell-tale sign of cosmic inflation: the imprint of primordial gravitational waves on CMB polarisation.

Different communities of cosmologist are working in strong collaboration (much more than in the past) to pursuit these goals. ESA, Jaxa and NASA are working together to deploy the fourth generation satellite for CMB : LiteBIRD [Lee 2019]). From the ground, The United States leads the way in ground-based experiments with the Simons Observatory and the CMB next generation Stage-4 experiments. Several European laboratories nevertheless are starting to collaborate with these ground-based experiments, also due to the development of new technologies (some of which were opened up entirely in recent times) led by many European institutes.

Parameter	TT+lowE 68% limits	TE+lowE 68% limits	EE+lowE 68% limits	TT,TE,EE+lowE 68% limits	TT,TE,EE+lowE+lensing 68% limits	TT,TE,EE+lowE+lensing+BAO 68% limits
$\Omega_b h^2$	0.02214 ± 0.00022	0.02248 ± 0.00026	0.0233 ± 0.0012	0.02229 ± 0.00016	0.02229 ± 0.00015	0.02234 ± 0.00014
$\Omega_c h^2$	0.1205 ± 0.0021	0.1169 ± 0.0021	0.1192 ± 0.0047	0.1196 ± 0.0014	0.1197 ± 0.0012	0.11907 ± 0.00094
$100\theta_{MC}$	1.04084 ± 0.00048	1.04141 ± 0.00051	1.03928 ± 0.00087	1.04088 ± 0.00032	1.04087 ± 0.00031	1.04095 ± 0.00030
τ	0.0521 ± 0.0080	0.0504 ± 0.0088	0.0504 ± 0.0088	0.0528 ± 0.0080	$0.0536^{+0.0069}_{-0.0077}$	$0.0552^{+0.0067}_{-0.0076}$
$\ln(10^{10} A_s)$	3.039 ± 0.016	3.031 ± 0.021	3.058 ± 0.022	3.039 ± 0.016	3.041 ± 0.015	$3.043^{+0.013}_{-0.015}$
n_s	0.9638 ± 0.0058	0.978 ± 0.011	0.967 ± 0.014	0.9658 ± 0.0045	0.9656 ± 0.0042	0.9671 ± 0.0038
H_0 [km s^{-1} Mpc^{-1}]	66.98 ± 0.92	68.72 ± 0.93	67.9 ± 2.6	67.41 ± 0.62	67.39 ± 0.54	67.66 ± 0.42
Ω_Λ	0.680 ± 0.013	0.703 ± 0.012	$0.687^{+0.035}_{-0.028}$	0.6861 ± 0.0085	0.6858 ± 0.0074	0.6897 ± 0.0057
Ω_m	0.320 ± 0.013	0.297 ± 0.012	$0.313^{+0.028}_{-0.035}$	0.3139 ± 0.0085	0.3142 ± 0.0074	0.3103 ± 0.0057
$\Omega_m h^2$	0.1432 ± 0.0020	0.1400 ± 0.0020	0.1431 ± 0.0038	0.1426 ± 0.0013	0.1426 ± 0.0011	0.14205 ± 0.00090
$\Omega_m h^3$	0.09593 ± 0.00045	0.09622 ± 0.00054	$0.0971^{+0.0015}_{-0.0017}$	0.09610 ± 0.00031	0.09610 ± 0.00031	0.09611 ± 0.00031
σ_8	0.8110 ± 0.0089	0.799 ± 0.012	$0.809^{+0.019}_{-0.017}$	0.8083 ± 0.0076	0.8091 ± 0.0060	0.8083 ± 0.0060
$\sigma_8(\Omega_m/0.3)^{0.5}$	0.837 ± 0.024	0.795 ± 0.025	0.825 ± 0.058	0.827 ± 0.016	0.828 ± 0.013	0.822 ± 0.011
$\sigma_8 \Omega_m^{0.25}$	0.610 ± 0.012	0.590 ± 0.013	0.604 ± 0.028	0.6050 ± 0.0083	0.6058 ± 0.0064	0.6033 ± 0.0057
z_{re}	$7.49^{+0.83}_{-0.75}$	$7.18^{+0.93}_{-0.75}$	$7.06^{+0.90}_{-0.76}$	$7.52^{+0.83}_{-0.75}$	7.61 ± 0.75	7.75 ± 0.73
$10^9 A_s$	2.089 ± 0.034	2.072 ± 0.042	2.130 ± 0.046	2.088 ± 0.034	$2.092^{+0.028}_{-0.031}$	$2.097^{+0.028}_{-0.032}$
$10^9 A_s e^{-2\tau}$	1.882 ± 0.014	1.873 ± 0.019	1.925 ± 0.024	1.879 ± 0.011	1.879 ± 0.011	1.877 ± 0.011
Age [Gyr]	13.825 ± 0.037	13.757 ± 0.039	13.75 ± 0.14	13.805 ± 0.025	13.805 ± 0.023	13.796 ± 0.020
z_*	1090.26 ± 0.41	1089.51 ± 0.42	$1088.8^{+1.6}_{-1.8}$	1089.99 ± 0.28	1089.99 ± 0.26	1089.88 ± 0.22
r_* [Mpc]	144.49 ± 0.48	145.15 ± 0.50	143.94 ± 0.66	144.58 ± 0.31	144.57 ± 0.28	144.70 ± 0.23
$100\theta_*$	1.04105 ± 0.00047	1.04158 ± 0.00050	1.03937 ± 0.00084	1.04107 ± 0.00031	1.04106 ± 0.00031	1.04114 ± 0.00030
z_{drag}	1059.43 ± 0.45	1059.98 ± 0.55	1061.9 ± 2.3	1059.73 ± 0.33	1059.74 ± 0.32	1059.79 ± 0.32
r_{drag} [Mpc]	147.23 ± 0.48	147.79 ± 0.52	146.31 ± 0.69	147.27 ± 0.31	147.26 ± 0.28	147.38 ± 0.25
k_D [Mpc^{-1}]	0.14054 ± 0.00052	0.14021 ± 0.00060	0.1423 ± 0.0012	0.14061 ± 0.00034	0.14063 ± 0.00033	0.14054 ± 0.00031
z_{eq}	3408 ± 48	3331 ± 48	3405 ± 90	3392 ± 31	3393 ± 27	3379 ± 22
k_{eq} [Mpc^{-1}]	0.01040 ± 0.00015	0.01017 ± 0.00014	0.01039 ± 0.00027	0.010352 ± 0.000095	0.010355 ± 0.000083	0.010314 ± 0.000066
$100\theta_{s,eq}$	0.4487 ± 0.0046	0.4565 ± 0.0047	0.4492 ± 0.0091	0.4503 ± 0.0030	0.4502 ± 0.0026	0.4515 ± 0.0021
f_{2000}^{143}	30.8 ± 3.0			29.8 ± 2.8	29.7 ± 2.8	29.5 ± 2.8
f_{2000}^{217}	107.6 ± 2.0			106.9 ± 1.9	106.9 ± 1.9	106.8 ± 1.9
$f_{2000}^{143\times217}$	33.0 ± 2.1			32.2 ± 2.0	32.2 ± 2.0	32.0 ± 2.0

Figure 1.11: Parameter 68 % intervals for the base-ΛCDM model from Planck CMB power spectra, in combination with CMB lensing reconstruction and BAO [Planck Collab. 2018]. The top group of six rows are the base parameters, which are sampled in the MCMC analysis with flat priors. The middle group lists derived parameters. The bottom three rows show the temperature foreground amplitudes $f^{TT}_{l=2000}$ the corresponding frequency spectra.

Bibliography

[A.A. Friedmann (1922)] Friedmann A.,1922,ZPhy, 10,377

[E. Hubble (1929)] Hubble 1929 1929CoMtW...3...23H Hubble E. 1929 CoMtW 3 23

[G. Gamow (1946)] G. Gamow. Expanding Universe and the Origin of Elements. Physical Review, 70:572–573, March 1946.

[Padmanabhan (1993)] Padmanabhan T.,1993,sfu..book,499

[Guth (1980)] A.H.Guth. Inflazionary Universe: a possible solution to the horizon and flatness problems. Phys.Rev., 1980.

[Penzias (1965)] A. A. Penzias and R. W. Wilson. A Measurement of Excess Antenna Temperature at 4080 Mc/s. Astrophysical Journal, 142:419–421, July 1965.

[Hu et al. 1994] Hu W., Scott D., Silk J.,1994,ApJL, 430,L5

[Mather (1999)] J.C. Mather et al., Astrophys. J. 512, 511 (1999)

[Chluba et al. 2019] Chluba J., Kogut A., Patil S. P., et al.,2019,BAAS, 51,184

[Fixen (2009)] D.J. Fixsen, Astrophys. J. 707, 916 (2009).

[Planck Collab (2016)] Planck Collab. 2015 Results I, Astron. & Astrophys. 594, A1 (2016).

[Scott 2016] Scott D., Smoot G. F.,2010,arXiv,arXiv:1005.0555

[Planck Collab 2015] Planck Collab. 2015 Results I, Astron. & Astrophys. 594, A1 (2016)

[Hinshaw et al. 2013] G. Hinshaw et al., Astrophys. J. Supp. 208, 19 (2013)

[Calstron et al. 2011] J.E. Carlstron et al., Publ. Astron. Soc. Pacific 123, 568 (2011)

[Swetz et al. 2011] D.S. Swetz et al., Astrophys. J. Supp. 194, 41 (2011)

[A. Kogut (1993)] A. Kogut et al., Astrophys. J. 419, 1 (1993).

[planck collab. (2014)] Planck Collab. 2013 Results XXIII, Astron. & Astrophys. 571, A23 (2014)

[Eisenstein (2005)] D.J. Eisenstein, New Astron. Rev. 49, 360 (2005)

[Hu-White (1997)] W. Hu and M. White, New Astron. 2, 323 (1997)

[Planck Collab. (2015)] BICEP2/Keck Collaboration, Planck Collaboration, Ade P. A. R., et al.,2015,PhRvL, 114,101301

[Aghanim (2019)] N. Aghanim et al., ESA F-class mission proposal (2019).

[Kogut (2019)] A. Kogut et al., arXiv e-prints (2019), 1907.13195.

[Sunyaev-Zeldovich (1980)] R.A. Sunyaev and Ya.B. Zeldovich, Ann. Rev. Astron. Astrophys. 18, 537 (1980)

[Planck Collab. 2016] Planck Collaboration, Aghanim N., Arnaud M., et al.,2016,A&A, 594,A22

[Hurier et al. 2013] Hurier G., Macías-Pérez J. F., Hildebrandt S.,2013,A&A, 558,A118

[Ade et al. (2019)] Ade, Peter et al., 2019, Journal of Cosmology and Astroparticle Physics, 02, 056–056

[Keating(2019)] Keating, B. 2019, APS April Meeting Abstracts 2019, Q12.003

[Pardo 2001] Pardo, J. R., Cernicharo, J., & Serabyn, E. 2001, IEEE Transactions on Antennas and Propagation, 49, 1683

[Planck 2018] Planck Collaboration, Akrami Y., Ashdown M., et al.,2018,arXiv,arXiv:1807.06208

[Dickinson 2016] Dickinson C.,2016,arXiv,arXiv:1606.03606

[Bouchet&Gispert 1999] Bouchet F. R., Gispert R.,1999,NewA, 4,443

[Errard 2015] Errard J., Ade P. A. R., Akiba Y., et al.,2015,ApJ, 809,63

[Planck 2014] Planck Collaboration, Ade, P. A. R., Aghanim, N., et al. 2014, A&A, 565, A103

[Planck 2016] Planck Collaboration, Ade, P. A. R., Aghanim, N., et al. 2016, A&A, 586, A141

[Draine 1998] Draine, B. T., & Lazarian, A. 1998, ApJ, 508, 157

[Draine 2016] Draine, B. T., & Hensley, B. S. 2016, arXiv:1605.06671

[Lee 2019] Lee, A., Ade, P. A. R., Akiba, Y., et al. 2019, BAAS51, 286

[Planck Collab. 2018] Planck Collaboration, Aghanim N., Akrami Y., et al.,2018,arXiv,arXiv:1807.06209

[Bolliet et al. 2018] Bolliet B., Comis B., Komatsu E., Macías-Pérez J. F.,2018,MNRAS, 477,4957

2

Lumped Element Kinetic Inductance Detectors for mm and sub-mm observations: a mini-review

Cryogenic detectors, with operating temperatures on the order of 100 mK, are currently the preferred technology for astronomical observations at millimetre and sub-millimetre wavelength ranges but also they have important application at the X-ray and gamma ranges [Zmuidzinas et al.(2012), Mazin et al.(2006)]. In the ultraviolet, optical, and near infrared (0.1-5 μm) wavelength range, these detectors are fundamentally limited by the band gap of the semiconductor and thermal noise sources from their relatively high (about 100 K) operating temperatures [Mazin et al.(2012)].

KIDs are a particular type of non-equilibrium superconducting photon detector, where incident radiation is absorbed in a superconducting material which is arranged in a resonant circuit. They were first developed by Peter Day and others scientists at the California Institute of Technology and the Jet Propulsion Laboratory in 2003 [Day et al.(2003)]. The primary attraction of KIDs is that, unlike most of the other low temperature detectors, they present several advantages:

- Easy to fabricate, in most cases, a single layer deposition is sufficient.
- Very sensitive, reaching the photon noise limit for most applications.
- They can be used in a very broad band.
- Fast, with a small time constant (from tens of microseconds to hundred of microseconds) for a large range of optical loads.
- Highly multiplexed (which means that making large arrays is simple).
- Relatively insensitive to micro-phonics and Electromagnetic interference (EMI).

In order to absorb incident millimetre and sub-millimetre radiation, it is necessary to match the impedance of the detector absorber to free space. In the case of KIDs, there are two methods to do it: the first is *Lumped-Element* KID (LEKID) where the inductive meander section is designed to act as a solid absorber for the target frequencies. By accounting for the resonator and substrate impedance and the cavity formed with the sample holder, it is possible to directly impedance match the LEKID to free space [Doyle et al.(2010)]. The second solution, is the use

Astrophysical Probes	SZ Eff.	Re-ionisation	CMB-B mode
Scientific Requirements	*1) Mapping Cluster from z = 0.02 - 1 with $rms_{Map} \approx 0.1mJy$ per bin* *2)Freq-Range (120-300 GHz)* *3) Pointed Observations*	*1) Molecules lines meas. ($rms_{Map} \approx 0.1mJy$ per bin)* *2) Freq-Range (100-400 GHz)* *3) Several deg^2 Survey*	*1) $rms_{Map} \approx 1\mu K$ - arcmin* *2) Freq-Range (60-400 GHz)* *3) Survey (30-40 % sky coverage)*
Technological Requirements	*1) Photometer or Low Res. Spectrometer ($\approx$ 1 GHz)* *2) Low/Medium Ang. Res. ($\approx$ 1-5') mappping nearby clusters)* *2) High Ang. Res. ($\approx$ 5-20" mappping distant clusters)*	*1) Low Res. Spectrometer ($\approx$ 1 GHz)* *2) Medium Ang. Res. $\approx$ 20-30"* *3) High control of time drift*	*1) Polarimeter* *2)Low Ang. Res. $\approx$ 10-30'* *3) High Control of Instr. Pol.*
Ground-Based Applications	*NIKA 2 (2015 - 3 kpixels)*, *KISS (2019- 600 pixels)*, *CONCERTO (2021- 4 kpixels)*	*CONCERTO (2021- 4 kpixels)*	CMB Stage-3/4 (2025) 10-100 k-pixels
Space Applications	*None*	*None*	*R&D*

Tableau 2.1: LEKID range of application to date and future perspectives. Ground-based instruments are green if they are already installed, orange if they are in preparation, red if they are planned to appear in a next future.

of a lens and antenna structure to adapt the resonator to free space (antenna-coupled KIDs). The Grenoble collaboration (Institut Néel, LPSC and IPAG) has pioneered the utilization of LEKID at millimeter frequencies. In parallel, other laboratories in France as APC, CSNSM and GEPI are developping preliminary work on antenna-coupled devices for millimetre science application [Traini et al. 2018] and LEKIDs for application in the optical range [Beldi et al. 2019].

The scientific picture which drove and drives the development of LEKID detectors within the Grenoble collaboration is essentially focused on the study of CMB B-mode of polarization, Sunyaev Zel'dovich effect and re-ionisation. In table 2.1, we present the LEKID range of application to date. Based on these scientific cases, we have both a fundamental R&D on the detectors-readouts, and an instrumental program in order to develop and optimize photometers, polarimeters and interferometers devoted to observe galactic polarization and CMB B-modes (NIKA 2 and ongoing discussions on a participation to the Stage-4 network), distortion of the CMB spectrum via the S-Z effect (NIKA 2, KISS and CONCERTO) and intensity line mapping (CONCERTO). For further details on the mentioned astrophysical instruments and R&D, please refer to Chapters 3 and 4.

2.1 LEKID basics

A superconductor is a material that shows a zero electrical DC resistance below a given critical temperature T_c. Below this critical temperature the conduction electrons are condensed into charge-carrying Cooper pairs with a binding energy $2\Delta \approx 3.52 k_B T_c$, where k_B is the Boltzmann constant and Δ is the energy gap of the superconductor [D. C. Mattis; J. Bardeen 1958]. For example, for a $\approx$ 20 nm Aluminium film $T_c \approx 1.4$ K and $\Delta \approx 0.2\ meV$.

Even if at zero frequency, the Cooper pairs do not produce any electrical impedance, at non-zero frequencies energy can be stored resulting in an effective reactive impedance known as the kinetic inductance. Incident photons with an energy exceeding the energy gap can break a Cooper pair, producing two quasi-particles changing the kinetic inductance and therefore the total complex surface impedance (Fig. 2.1a). When the superconductor material is used to make a resonant circuit, a change in the kinetic inductance will be directly linked to a shift in the resonance frequency (and phase) of the resonator (Fig. 2.1b,c,d). A typical superconductor material largely used at millimetre wavelength is Aluminium where the superconducting gap corresponds to an electromagnetic frequency of about 110 GHz.

In real life, the change in kinetic inductance with change in quasi-particle density (upon photon absorption) is very small. This requires the film to be fabricated with high Quality factor Q in order to make this variation measurable by a microwave resonance circuit. This is a key requirement in producing KID because the photon absorption is directly scaled by Q, which can be of the order $10^4 - 10^5$ for a low-loss superconducting resonator operating well below the critical temperature.

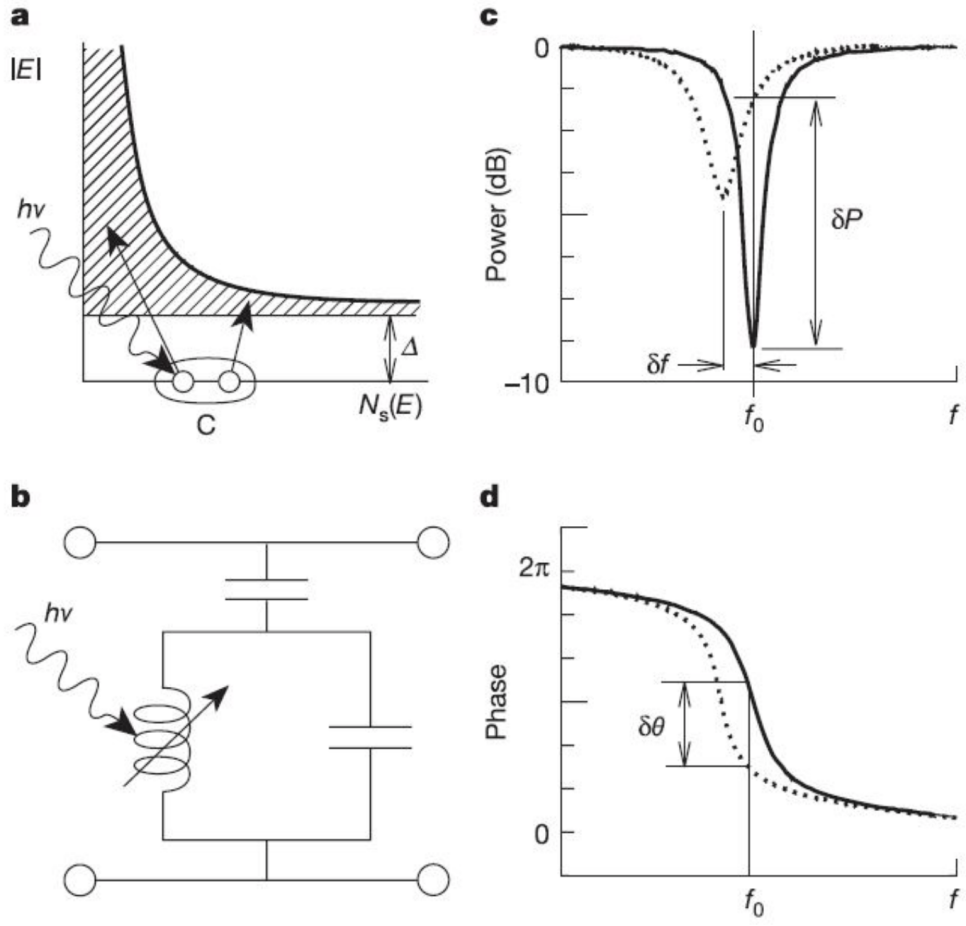

Figure 2.1: The KID detection principle [Mazin 2004].

The intrinsic noise limit of a KID is limited by generation-recombination (gr) noise, which scales with temperature and film volume [Sergeev et al.(2002)]. This gives the principal constraints on such a device to be operating around 100 mK where the gr noise is of the order of 10^{-20} W/$\sqrt{Hz}$. Under these conditions, we can monitor the change in phase of a fixed tone microwave signal centred on the resonant frequency.

As mentioned in the previous section, the Grenoble collaboration is actively involved in LEKID development. In these particular devices, the resonator is schematically composed by an inductive meander (used as an absorber) and an inter-digitated capacitor coupled to a co-planar feed line (see Fig. 2.1b). The resonant frequency is controlled geometrically by changing the capacitance of the inter-digitated capacitors of each detector distributing a large number of KIDs to a single transmission line (Fig. 2.2). This can be done with a low interference level (electrical cross-talk) if the frequency spacing between resonances is larger then $2\Delta\omega$ (where $2\Delta\omega$ is the bandwidth of order $\Delta\omega = \omega_0/Q \approx$ 10–100 kHz).

The meander-absorber geometry is designed depending on the particular goal of the related instrument. In Grenoble, we develop two geometries: the first to be intrinsically sensitive to a direction of the linear polarisation, the second sensitive to dual polarisation based on the Hilbert fractal geometry that we proposed some years ago [Roesch et al.(2012)] (see Fig. 2.2).

The responsivity of a KID under optical illumination only depends on the amount of power absorbed assuming that the majority of the quasiparticles are generated by incident photons. This is completely true when the incident photons have an energy compared to the superconductor gap where the whole energy of the photon is used to break a Cooper pair and therefore to produce a

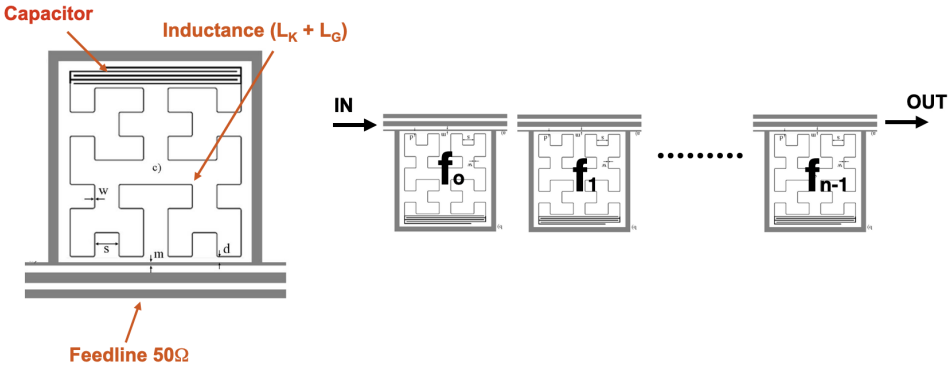

Figure 2.2: LEKID pixel representation (left) and schematic view of distribution of a large number of LEKID in a single feed line. *For this example , it is shown a meander/absorber sensitive to dual polarisation based on 3rd-order Hilbert pattern [Roesch et al.(2012)].*

measurable signal. The responsivity can be expressed in terms of a shift in the resonant frequency (ω) for a given change in optical power (W_{opt}) as [Doyle 2008]:

$$\Re_\omega = \frac{d\omega}{dW_{opt}} = -\frac{1}{2}\frac{dL}{dW_{opt}}\frac{\omega}{L}$$

where the variation of the inductance L over the optical power is:

$$\frac{dL}{dW_{opt}} = N_{sq}\frac{dL_k}{dn_{qp}}\frac{dn_{qp}}{dW_{opt}}$$

where N_{sq} is the number of squares in the meander, L_k is the kinetic inductance per square in the LEKID, n_{qp} is the quasiparticle density and $\frac{dn_{qp}}{dW_{opt}} = \frac{\tau_{qp}}{\Delta V}$ with V is the volume of the superconducting material and τ_{qp} is the quasi-particle lifetime.

For most of LEKID developed within the Grenoble collaboration, we are not limited by the intrinsic noise of the LEKID but rather by external noises such as amplifier noise in the readout (see section 2.4). This means that the sensitivity will be maximised when the responsivity is a maximum.

2.2 Fabrication process

A big advantage in using KID is that they are easy to fabricate. Indeed, in some cases they need just a single deposition step. This is a key point in the rise of this technology with respect to the other technologies (as for example high impendance bolometer and TES) where the lithography procedures are more complex. As far as focal planes are concerned indeed, an important parameter to evaluate a technology is the cost of producing an array of detectors which is strongly related to the number lithography procedures.

In the Grenoble collaboration, we developed a simple procedure which aims to build the focal planes of our instruments (see Chapter 3) and it is used as a reference for the developments of KID for space applications (see Chapter 4). In the following, we give some details about the fabrication process:

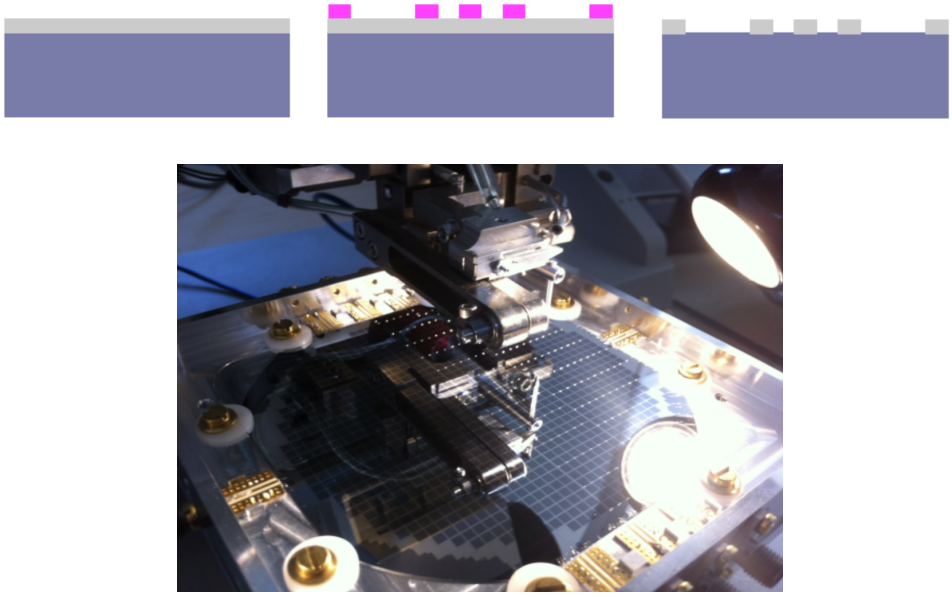

Figure 2.3: Top panels: schematic view of the different steps of a LEKID fabrication: left, evaporation of the film in the substrate. Middle, optical lithography. Right, etching. Bottom panel: picture of the kilo-pixel array operating in the NIKA 2 instrument.

The fabrication starts with a high-resistivity ($> 6000\Omega \cdot cm$) silicon substrate with a thickness optimised to maximise the optical coupling efficiency at the suitable electromagnetic frequencies (typically few hundreds of microns at millimetre wavelength). The native silicon oxide is etched with an HF:H_2O 5 % solution, then rinsed in H_2O. This step passivates the Si bonds on the surface, replacing O with H. The wafer is then put under vacuum within the next 30 minutes to prevent re-oxidation. One or more thin films are deposited (one for mono-layer Aluminium detectors used for most of our applications, two for bi-layers detectors used for detection at frequencies between 80 and 120 GHz), by e-beam evaporation under a $\sim 3 \cdot 10^{-8}$ mb vacuum, followed directly by a 25 nm thick aluminium film. This latter ensures that there is no oxidation layer at the interface between titanium and Aluminium and ensures the highest proximity effect between the two layers. The next step is a standard photo-lithographic process, with a positive resin (AZ1512Hs). The etching is made in two phases, first with an Al-etch dip, then with a diluted 0.1 % HF solution to etch Ti 2.3. After dicing, the array is mounted on a dedicated holder, and the CPW is wire-bonded to the launcher with an Al-Si wire.

2.3 Readout electronics

In the standard KID readout scheme, each pixel is excited using a fixed tone at its resonant frequency. The signal transmitted past the detector is compared to a reference copy of the excitation signal to get its in-phase (I) and quadrature (Q) components. To accomplish it, we need to develop a dedicated readout system which is composed of a cold electronics section and a front-end warm readout.

One of the key advantages of the KID technology is the simplicity of the cold electronics. Each block of detectors is connected to a single coaxial line providing the excitation and the readout.

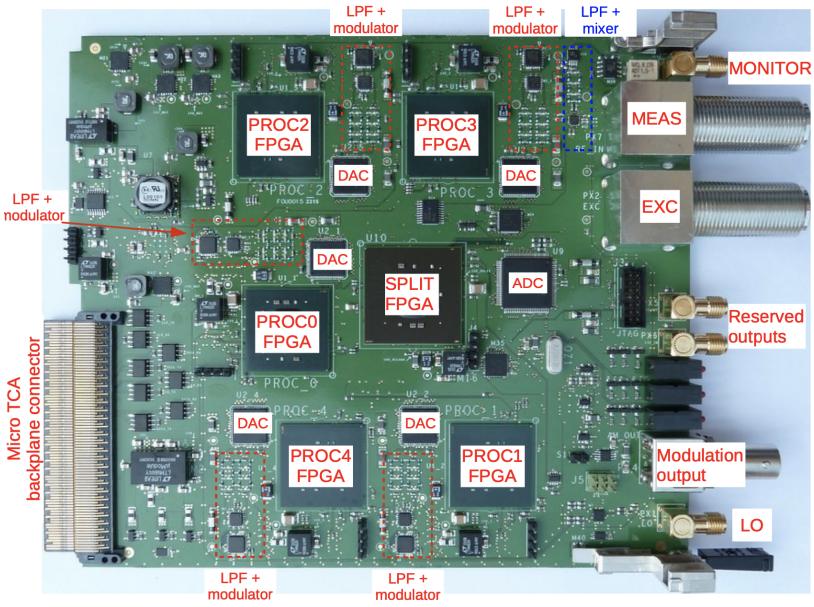

Figure 2.4: Readout Board designed and fabricated within the Grenoble Collaboration [Bourrion et al. 2016].

The number of detectors connected to each block defines the *multiplexing* factor. This factor has been 500 in the last version of the readout developed for the CONCERTO instrument (see details of the instruments in Chapter 3).

The excitation lines, composed of stainless-steel cables, are running from 300 K down to sub-Kelvin temperature with a proper thermalisation at each cryogenic stage and a fixed attenuation (usually on the 4 K stage) in order to suppress the room temperature thermal noise. Each excitation line ends through superconducting (aluminium) micro-bonds, to the silicon wafer holding the detectors. The approximate excitation power per resonator is typically of the order of 10 pW.

On the readout side, the same types of micro-bonds are used to transfer the signal out of the focal plane and to make it available on a second SMA connector. Then a superconducting (Nb) coaxial cable is used to connect the measurement output directly to the input of a cryogenic low-noise amplifier (LNA). The amplified signal provided by the LNA is transferred through the remaining cryostat stages (up to 300 K).

Outside the cryostat, the warm readout [Bourrion et al. 2016] has been designed and fabricated within the Grenoble collaboration named NIKEL (New Iram Kid ELectronic). In its more advanced version, it is capable of generating up to 500 tones each, over a 1 GHz bandwidth. This is achieved by using separate FPGAs, each one generating tones over a particular sub-band, using associated DACs. The FPGAs act as a central unit that combines the signal of the other units, appropriately shifting and filtering the different sub-bands to finally cover the whole bandwidth for the frequency comb used to excite the detectors. An analogous, but reversed, process is then applied to the signal acquired by the ADC of the board, which is once again split in sub-bands treated separately.

Each feedline is readout by one board (see Fig. 2.4) mounted in Advanced Mezzanine Card format, central, clocking and synchronisation boards (CCSB) mounted on the MicroTCA Carrier Hub (MCH). Each board is mounted in a micro-Telecommunication Computing Architecture (MTCA) crate. Depending on a considered instrument, different number of boards is used and/or different crates are needed.

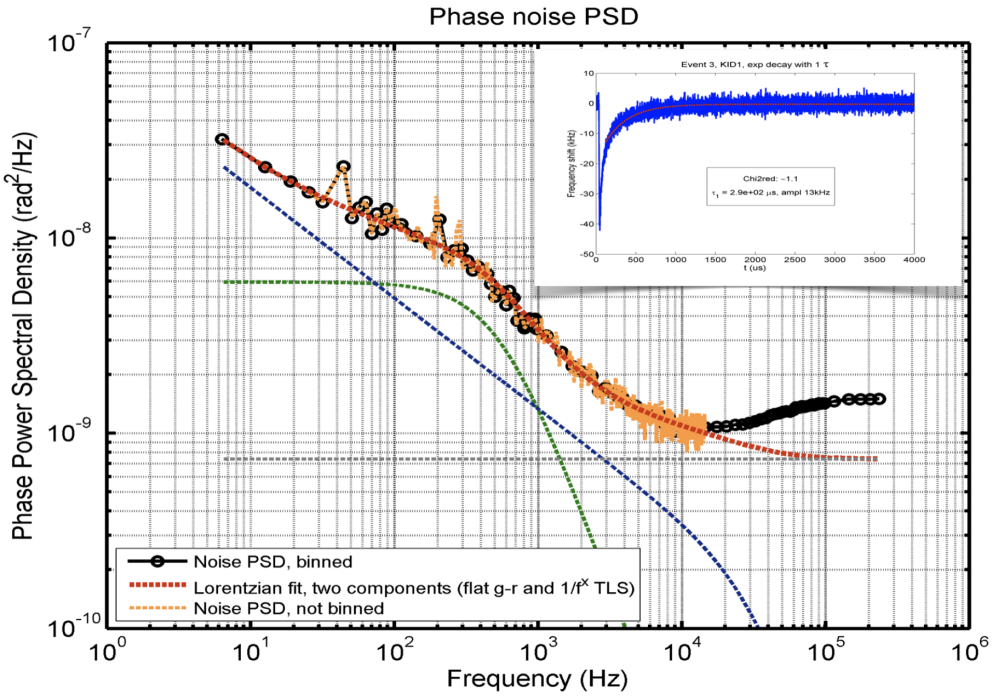

Figure 2.5: Phase noise density measured from 6 Hz to 300 kHz. Four components of noise are fitted in order to derive the recombination time constant. Top right: cosmic ray events. The decay time is fitted to derive the recombination time constant.

2.4 Time response and whole chain noise budget

Low temperature LEKIDs have a finite time response set by the fact that they are pair-breaking detectors, in which the absorbed photon energy breaks Cooper pairs inside the superconductor and create extra quasi-particles which recombine with a typical time constant (gr time constant τ_{qp}). In general, a time response, if slow (typically if greater than milliseconds), can have an impact on the final sensitivity since it attenuates the response. Also, more in particular for space applications, the impact of cosmic rays on the amount of unusable data will be much more important if the time constant is high. LEKID produced for ground applications have shown a time constant of the order of few tens of micro-seconds. We know from LEKID theory [Doyle 2008] that the quasiparticle lifetime is:

$$\tau_{qp} = \sqrt{\frac{n_0 \tau_0 V \Delta}{W_{opt}}}$$

where n_0 and τ_0 are materials constants, V is the volume of the superconducting material and W_{opt} is the background optical power. The time constant is supposed to increase with decreasing optical background, it is therefore important to measure it in space conditions in order to confirm that it does not exceed the typical millisecond range. In Fig. 2.5, we show a noise spectrum measured on a LEKID observing with a 30 % bandwidth centered at 150 GHz, with a typical optical load of a few pW (typical space environment given by the monopole of CMB at 2 mm). The spectrum has been performed using homodyne acquisition with picoscope in a range of frequencies between a few Hz up to a fraction of a MHz. In this range of frequencies indeed, we can clearly observe the cut-off due to the recombination time constant. In order to derive the recombination time constant, we fit few noise components:

1. Generation-Recombination noise : fitted as a low pass filter with a time constant τ_{qp} (lorentzian function-green curve)
2. Two system level noise (TLS) : attributed to tunneling states in amorphous dielectrics with broad microwave energy spectra. Hard to predict but following a well-known scaling law (blue curve).
3. Pre-ampli noise : constant in this frequency range (grey curve)
4. 1/f noise : due to all the sources that can generate low frequency noise (optical, vibrations, etc...)

In parallel to the noise measurements, we recorded a few events due to the cosmic rays (see insert of Fig. 2.5). By fitting the decay time of the spikes we can derive the recombination time constant and we can compare with the noise measurements. The agreement between the two analysis is very good, we obtain $\tau_{qp} = 298 \pm 22\mu s$ for noise measurement noise and $\tau_{qp} = 290 \pm 35\mu s$ by fitting the glitches decays. As expected, the time constant is higher with respect to the same pixel operating with higher background but still fast enough for a typical instrument that would be operated in space.

2.5 Photometry with LEKID

One of the most difficult challenges in operating with KID, is to convert the observed in phase (I(t)) and in quadrature (Q(t)) signal to absorbed optical power. This is a very different task with respect to the dissipative readout like thermal detectors (high impedance bolometer, TES, etc...). One possible solution is to perform a frequency sweep before starting each sky observation in order to determine the centre of the resonance circle (I,Q) and calibrate the change of the phase ($\theta(f)$) as a function of frequency (see Fig. 2.6a). The validity of this method depends directly on the stability of the atmosphere. Indeed, if the sky emission fluctuates during an observation, the resonance circle changes and therefore the responsivity of the detector changes. In order to improve the photometric reproducibility, we developed two systems to control the change of the signal. The two methods can be implemented depending on the different applications and instrument arrangements.

- **Slow sampling rate data acquisition** ($\approx 10 - 100$ Hz): This method was first developped for the NIKA prototype and then currently used for the NIKA 2 final instrument [Calvo et al.(2014), Catalano et al.(2014)]. The idea is to replace the standard excitation of the detectors, which uses a fixed tone, with a new excitation based on two different frequencies. We achieve this by modulating the frequency on the local oscillator (by few kHz) synchronously with the FPGA in order to generate two tones one just above and the other just below the resonant frequency of the detector. An average of about 50 points is then performed in the FPGA in order to extract a clean signal with low noise level. Thanks to this modulation, it is possible to estimate the variation of the resonant frequency of the detectors $\Delta\omega_0(t)$, by projecting ($\Delta I(t)$,$\Delta Q(t)$) along the gradient found as:

  Thus, each raw data point, which is sent to the acquisition software at a reduced sampling rate, is composed of the values $(I(t), Q(t))$ of each pixel, as well as the corresponding differential values (see Fig. 2.6b):

$$\left(\frac{dI}{d\omega}(t), \frac{dQ}{d\omega}(t)\right) = \left(\frac{I(\omega_+) - I(\omega_-)}{\delta\omega_{LO}}, \frac{Q(\omega_+) - Q(\omega_-)}{\delta\omega_{LO}}\right).$$

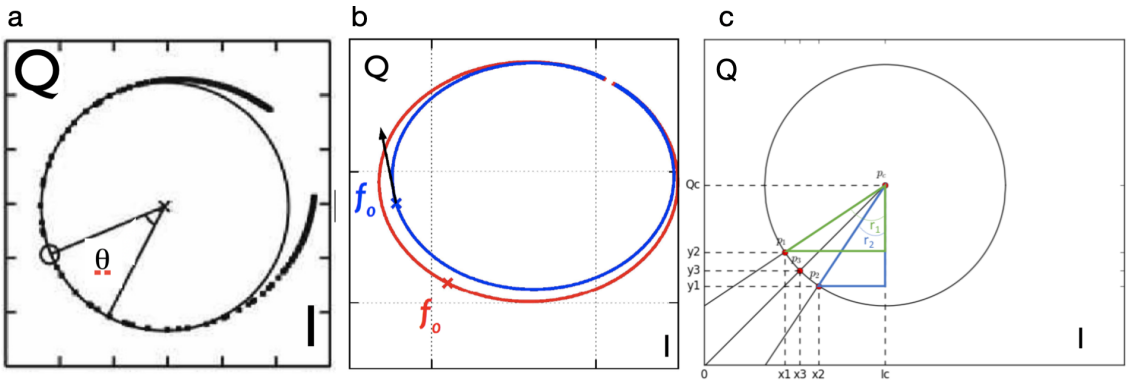

Figure 2.6: Different methods to calibrate the LEKIDs signal from the (I,Q) circle. Left panel: Classical (old) approach. Frequency sweep before each observation to calibrate the signal (poor photometric accuracy). Middle panel: Low sampling rate acquisition (used in NIKA 2). Representation of a sweep-around a resonance for two different data points (red and blue curve). The measure of the angles ϕ and θ can be carried out for each acquired point thanks to the modulated readout technique. Right panel: fast sampling rate acquisition (used for KISS and CONCERTO). p1 and p2 represent the modulation points, p3 represent the non-modulated (usable for science) data points.

If a variation $(\Delta I(t), \Delta Q(t))$ is observed between successive points, it is possible to estimate the corresponding shift in the resonant frequency, $\Delta\omega_0(t)$, by projecting $(\Delta I(t), \Delta Q(t))$ along the gradient found using previous equation:

$$\Delta\hat{\omega}_0(t) = \frac{(\Delta I(t), \Delta Q(t)) \cdot (dI/d\omega(t), dQ/d\omega(t))}{(dI/d\omega(t), dQ/d\omega(t))^2} \cdot \delta\omega_{LO}.$$

With this method the original sampling rate delivered by the readout is reduced (up to a factor 50 as mentioned previously), it therefore can be used for LEKID-based instruments having a data rate which does not exceed the range 10-100 Hz. For photometers this is in general true since the rate depends only on the scanning speed of the telescope.

- **Fast sampling rate data acquisition** ($\approx 1-4$ kHz):

  Interferomenters such as KISS and CONCERTO have more stringent constraints on the acquisition sampling rate. This is in particular true for ground-based FTS instruments where the movable part which makes beam interfering, must move faster then the typical atmospheric time scale (of the order of 1 Hz) in order to assure a low sky noise level. The fast LEKID time response permits to do this without any manifest loss of information. The readout sampling frequency also has to follow this requirement. We proved that 4-5 hundred data points for each interferogram are needed in order to preserve all the spectral informations in the data in the band of interest. This means that, if the sampling rate on the sky is of the order of 10 Hz, the readout electronics has to work with a sampling frequency higher than 4-5 kHz. In these conditions, it is not possible to modulate the signal each single point as we did for NIKA 2, because the FPGA does not reach the necessary rate. We developed therefore a new method which makes a monitoring of the optical background changing in time as well as the previous method, but in this case we modulate the frequency on the local oscillator by few kHz before each interferogram producing some dead time (where the mirrors do not move) at each block of data (see Fig. 2.7).

  We can extrapolate the calibration factor C [Hz/rad] through a circular fit on the modulation points (x1, y1) and (x2, y2), referring to Fig. 2.6c. We obtain, in this way, the coordinates

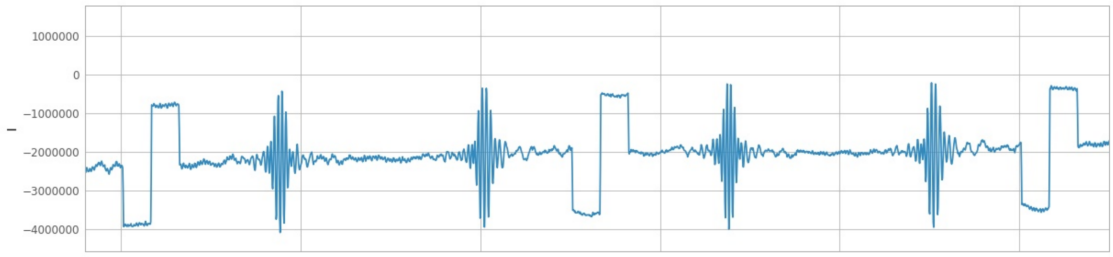

Figure 2.7: Typical raw signal for the interferometers KISS and CONCERTO which used a fast sampling rate acquisition at 4 kHZ. We modulate the frequency on the local oscillator before each interferogram producing some dead time at each block of data.

of the circle centre (Ic,Qc). We can calculate, thus, the r1 and r2 angles

as following:

$$r_1 = \arctan \frac{I_c - x_1}{Q_c - y_1}$$

$$r_2 = \arctan \frac{I_c - x_2}{Q_c - y_2}$$

The modulation factor C is obtained as follow:

$$\Delta\phi = r_2 - r_1$$

$$C = \frac{\Delta\phi}{\Delta\omega}$$

where $\Delta\omega$ is the modulation in Hertz set by the injecting tone.

2.6 KID around the World

KID for millimetre and sub-millimetre sky observations is one of the most active area of research, with several groups in Europe, United States and Japan actively developing detectors and KID-based instruments.

The very first KID instrument to be put on the sky, was DemoCam [Schlaerth (2008)] from the 10-m Caltech Sub-millimetre Observatory (CSO) in April 2007. It observed the planet Jupiter and the HII region G34.4v with 16-pixel, 2 color/pixel array.

However, the first instrument making science with KID was the NIKA prototype (see Chapter 3), designed, fabricated and exploited by the Grenoble collaboration. The NIKA camera is a 356-pixels instrument conceived as a resident common user instrument and an early technology demonstrator for NIKA 2. The NIKA prototype detected the cluster of Galaxy RXJ via the Sunayaev Zel'dovich effect in February 2012 [Adam et al. 2014].

Today, several instruments observe the millimetre sky using large-format focal plane arrays. A number of projects operating at millimetre (TolTEC [Toltec web page], SuperSpec [Shirokoff et al. (2014)], GroundBIRD [Nagasaki et al. 2018], OLIMPO [Paiella et al.2020]) and submillimetre (AMKID [Baselmans J. 2018], Deshima [Takekoshi et al. 2020], BLAST-TNG [Galitzki et al (2014)]) wavelenght. However, to date, experiments designed specifically to measure the

CMB have been led by instruments based on arrays of transition edge sensors (TESs) [Benson et al. 2014, Thornton et al. 2016]). State-of-the-art CMB experiments are at *Stage 2-3*, with focal planes containing 5000–10,000 TES. KID are coming into play in particular thanks to the discussions in progress for a participation of the Grenoble collaboration in the Stage-4 network. Further improvements in sensitivity can only be achieved by increasing total focal plane area and number of detectors which is a significant technological challenge. The advantages of KIDs could play therefore an important role in this sense.

Bibliography

[Mazin et al.(2006)] Mazin et al., Applied Physics Letters, 2006.

[Zmuidzinas et al.(2012)] Zmuidzinas, J. 2012, Annual Review of Condensed Matter Physics, 3, 169

[Mazin et al.(2012)] Mazin et al., Optics Express, 2012.

[Day et al.(2003)] Day, P. K., LeDuc, H. G., Mazin, B. A., et al. 2003, Nature, 425, 817

[Doyle et al.(2010)] Doyle, S., Mauskopf, P., Zhang, J., et al. 2010, Proceedings of the SPIE, 77410M

[Traini et al. 2018] Traini A., Tartari A., Bordier G., Boussaha F., Chaumont C., Beldi S., Reix F., Piat M.,2018,JLTP, 193,170

[Beldi et al. 2019] Beldi S., Boussaha F., Chaumont C., et al.,2019,arXiv,arXiv:1901.10193

[D. C. Mattis; J. Bardeen 1958] D. C. Mattis; J. Bardeen, Physical Review. 111: 412, 1958

[Mazin 2004] B. Mazin. PhD Thesis, Caltech, 2004.

[Sergeev et al.(2002)] A. V. Sergeev, V. V. Mitin and B. S. Karasik, Appl. Phys. Lett., Vol. 80, February 2002, pp. 817-819

[Roesch et al. 2012] Roesch M., Benoit A., Bideaud A., et al.,2012, arXiv,arXiv:1212.4585

[Doyle 2008] S. Doyle. PhD Thesis, Cardiff University, 2008.

[Bourrion et al. 2016] Bourrion O., Benoit A., Bouly J. L., et al.,2016,JInst, 11,P11001

[Calvo et al. 2013] Calvo, M., Roesch, M., Désert, F. X., et al. 2013, A&A, 551, L12

[Catalano et al.(2014)] Catalano, A., Calvo, M., Ponthieu, N., et al. 2014, A&A, 569, A9

[Schlaerth (2008)] J. Schlaerth, A. Vayonakis, P. Day, J. Glenn, J. Gao, S. Golwala, S. Kumar, H. Leduc, B. Mazin, J. Vaillancourt, and J. Zmuidzinas, J Low Temp Phys 151, 684–689 (2008).

[Shirokoff et al. (2014)] E. Shirokoff et al., J. Low Temp. Phys. 176(5), 657–662 (2014)

[Adam et al. 2014] Adam R., Comis B., Macías-Pérez J. F., et al.,2014,A&A, 569,A66

[Toltec web page] http://toltec.astro.umass.edu/about.php

[Galitzki et al (2014)] N. Galitzki et al., Instrum. 3(2), 1440001 (2014)

[Nagasaki et al. 2018] Nagasaki T., Choi J., Génova-Santos R. T., et al.,2018,JLTP, 193,1066

[Paiella et al.2020] Paiella A., Ade P. A. R., Battistelli E. S., et al.,2020,JLTP..tmp

[Baselmans J. 2018] Baselmans J.,2018,alas.conf,1

[Takekoshi et al. 2020] Takekoshi T., Karatsu K., Suzuki J., et al.,2020,JLTP..tmp

[Benson et al. 2014] B.A. Benson et al., SPIE Astron. Telesc. Instrum. 9153, 91531P91531P21 (2014)

[Thornton et al. 2016] R.J. Thornton et al., Astrophys. J. Suppl. Ser. 227(2), 21 (2016)

3

Next-Generation Ground-Based Experiments

3.1 Next-Generation Photometers

For the upcoming years, the international framework shows that the CMB community strongly believes in the need for CMB observations using ground-based instruments as much as possible. This is due to several reasons: compared to an experiment that observes from space, a ground-based experiment requires lower costs and can obtain, within some limitations, very remarkable results. In particular, for targets for which the level of signal is still unknown (such as the CMB B-modes polarisation), the use of a spaceborne instrument, would not only be very expensive but also very risky, since the instrument may not lead to any detection at the end of its lifetime. Furthermore, with regards to objectives such as the mapping of galaxy clusters via the SZ effect, or gravitational lensing mapping, high angular resolution is required. This requirement could never be fulfilled by a satellite whose telescope mirror can be only the order of 1-3 meters at most in diameter. As an example, in Fig.3.1, we present the expected sensitivity per pixel between a space payload and a ground-based instrument. If we consider a 2-year space mission at 100 GHz, in order to have a comparable observation, a ground-based instrument must have an increased integration time or number of detectors of about 2-3 order of magnitude. Therefore, considering that a space mission today could typically mount hundred-pixels arrays, for an equal integration time, we would need arrays of detectors on the scale 10-100 kpixels. This is indeed the typical size expected for the new generation stage-4 ground-based instruments.

From a technological point of view, ground-based experiments have a low risk coefficient because they can continuously undergo adjustments and maintenance operations as often as required. In addition, the electrical consumption and the cryogenic facilities are almost unlimited on the ground while they generate large limitations for experiments that observe from space.

For these reasons, after the results published by Planck, cosmologists realised that a well-coordinated effort for ground-based observations between 60-350 GHz could potentially make the first detection of the CMB B-mode polarization [Abazajian et al. 2019].

The first generation ground-based instruments deployed during the last decade. These instruments can be divided into high angular resolution instruments (such as ACT [Thornton et al. 2016], POLARBEAR [Barron et al. 2014], QUaD [Castro et al. 2009]) that aim to measure the primordial B-mode above $l \sim 10$, and low angular resolution instruments such as BICEP2 / Keck which instead focus on measuring primordial B-modes at low l. In the future, a new generation of instrument will be deployed, collectively known as the CMB-S4 collaboration, which consists of

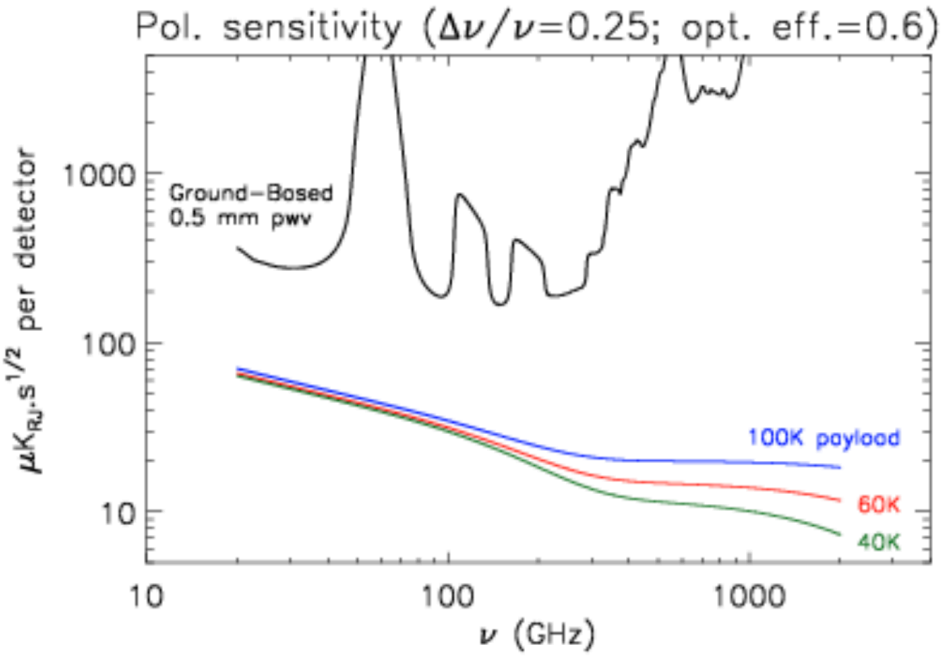

Figure 3.1: Example of comparison of the sensitivity between ground-based and space observation for polarisation. Noise Equivalent Temperature (NET) per single polarised pixel is presented for a typical CMB observations with a photometer (25 % bandwidth) and diffraction-limited observations. In the case of a spaceborne instrument, we consider 3 different temperatures of the payload. The ground-based scenario has the same conditions as the ATACAMA desert (PWV=0.5 mm), observing at 60 deg *elevation.*

several dedicated telescopes equipped with highly sensitive superconducting cameras[1].

In the last months, several discussions have taken place at various levels in France about the possibility of participating in the CMB-S4 collaboration. The scientific community expects a set program for the CMB research development. The idea is to proceed in parallel between setting the ground for our future involvement in Stage-4 or Simons Observatory by contributing to existing experiments and aggressively pursue on R&Ds projects. R&D means developing new hardware that will contribute to the Stage-4 project in some way. The goal is to have some structure to ensure our involvement by 2027. For the first period, our group in Grenoble will interact with French collaborators and US and German groups on the science targets and instrument design. The goal is to develop, construct, install, and commission a KID-based camera by 2025.

Naturally, our group in Grenoble is participating in competing for hardware R&D projects, contributing (together with the French community) to the discussions around CMB-S4 but above all, developing tools that play an important role for cosmology both from a purely astrophysical point of view and a technological point of view. This is the case for NIKA 2, KISS and CONCERTO instruments which are detailed in this chapter. For example, NIKA 2 is a high resolution, sub-arcmin, ground-based camera, which is complementary to CMB experiments [Perotto et al.(2019)] [Adam et al.(2018)]. NIKA 2 will allow not only a detailed reconstruction of the cluster dynamical history but also a measurement of the kinetic SZ effect (see Fig.3.2) making it complementary to the Athena measurements as well [Pointecouteau et al. (2015)]. Additionally, a

[1] https://cmb-s4.org

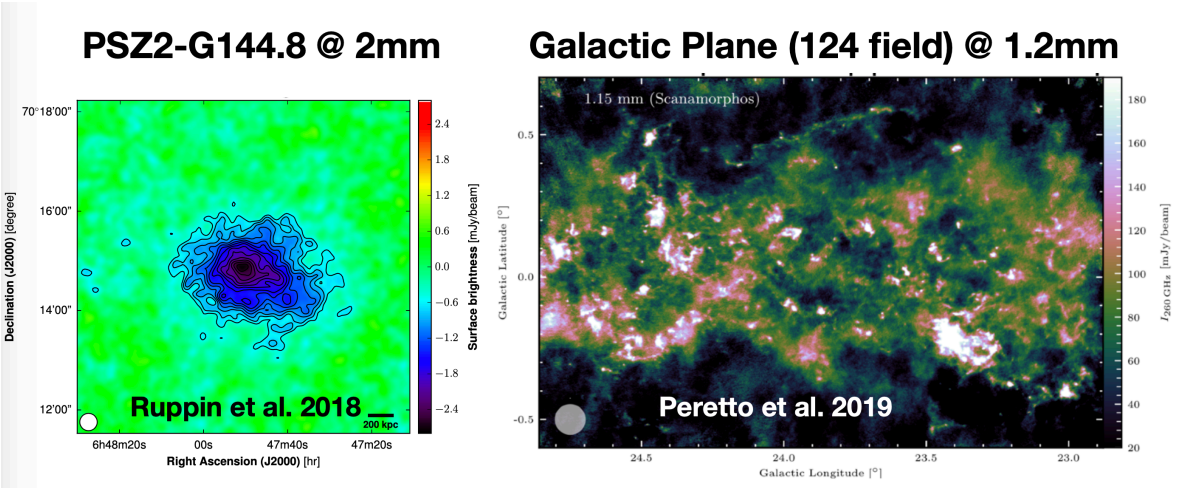

Figure 3.2: Recent results from the NIKA 2 instrument.

big advantage of NIKA 2 is that it represents the first operational deployed instrument using KIDs, and this technology is the front-runner of the French community as a detector to fill the CMB-S4 focal planes. Finally, NIKA 2 can also observe polarisation with a rotating half-wave plate (HWP) so it can be used to calibrate any systematic effects in polarisation for the next generation of instruments.

In the following sections, I will present a more detailed discussion of the ground-based instruments NIKA 2, KISS, and CONCERTO and my involvement in these projects.

3.2 The NIKA 2 instrument

Operating in two millimetre bands (1.15 mm and 2.0 mm), the NIKA 2 camera simultaneously observes the mJy point sources and maps the extended continuum emission with a field of view (FOV) of 6.5 arc-minutes in line with a diffraction-limited resolution and background-limited performance. Such observational capabilities led the NIKA 2 camera to be a science driver in several astrophysical fields for follow-up observations of Planck satellite clusters via the Sunyaev-Zel'dovich effect, high redshift sources and quasars, early stages of star formation and nearby galaxies emission. In addition, the NIKA 2 instrument is capable of detecting polarisation in the 1.15 mm arrays. This is done by using a rotating warm HWP to modulate the astrophysical polarised signal and a polariser mounted at the 100 mK stage to analyse the linear polarisations on the two 1.15 mm arrays. A first version of the instrument was fielded as the NIKA prototype (NIKA 1), which was few hundred-pixel demonstration instrument used as a pathfinder of the final

	Array 1&3	Array 2	Reference
Reference Wavelength [mm]	1.15	2.00	
Reference Frequency [GHz]	260	150	Sect. 8.1.1
Frequency [GHz]	254.7&257.4	150.9	Sect. 2.5
Bandwidth [GHz]	49.2&48.0	40.7	
Number of designed detectors	1140&1140	616	Sect. 2.3
Number of valid detectors[a]	952&961	553	Sect. 5.3
Fraction of valid detectors [%]	84	90	
Pixel size in beam sampling unit[b] $[\lambda/D]$	1.1	0.87	Sect. 5.2
FWHM[c] [arcsec]	11.1 ± 0.2	17.6 ± 0.1	Sect. 6.2
Beam efficiency[d] [%]	55 ± 3	77 ± 2	Sect. 6.3
Rms FWHM across the FOV [arcsec]	0.6	0.6	Adam et al. (2018)
Reference FWHM[e] [arcsec]	12.5	18.5	Sect. 8.1.1
Reference Beam efficiency[f] [%]	70 ± 4	85 ± 3	Sect. 8.1.3
Rms pointing error [arcsec]	< 3	< 3	Sect. 3.2
Absolute calibration uncertainty [%]	5	5	Sect. 9.1, App. A.1
Systematic calibration uncertainty[g] [%]	0.6	0.3	Sect. 9.1.3
Rms calibration uncertainty [%]	5.7	3.0	Sect. 9.2
α noise integration in time[h]	0.5	0.5	Sect. 10.3
NEFD[i] $[\mathrm{mJy} \cdot \mathrm{s}^{1/2}]$	30 ± 3	9 ± 1	Sect. 10.3
M_s[j] $[\mathrm{arcmin}^2 \cdot \mathrm{mJy}^{-2} \cdot \mathrm{h}^{-1}]$	111 ± 11	1388 ± 174	

Figure 3.3: Summary of the main characteristics describing NIKA 2 measured performance [Perotto et al.(2019)].

NIKA 2 camera between 2010-2014. The NIKA 1 camera has been open to public observations since the beginning of 2014 and it is considered as the first successful demonstration of KID technology on a science grade telescope [Catalano et al.(2014)]. The NIKA 2 instrument represented a huge step in performance as compared to the NIKA pathfinder instrument. After being commissioned at the end of 2016, NIKA 2 is now an IRAM resident instrument for the next ten years or more, allowing the astrophysical community to tackle a large number of open questions, from the role of the Galactic magnetic field in star formation to the discrepancy between cluster-based and CMB-based cosmology possibly caused by the unknown cluster physics. In particular, the NIKA 2 instrument has a large program directed by our group at the LPSC dedicated to map out Sunyaev–Zel'dovich signature in clusters out to distances of $z = 2$.

The NIKA 2 consortium, which has a large presence in Grenoble (LPSC, Institut Néel, IPAG and IRAM), has been responsible for the design, construction, and commission of the instrument. In addition, the NIKA 2 consortium pledged to provide technical support for the 10 years of estimated life time of the instrument. This contribution is rewarded with 1000 hours of guaranteed time distributed in five large programs over 4 years :

- Clusters of galaxies via the Sunyaev Zel'dovitch effect.
- Deep surveys.
- Mapping the insterstellar medium.
- Nearby galaxies.
- Polarization measurements of Galactic regions.

Contributions on NIKA 2 instrument: I am part of the NIKA 2 core team as a "builder" of the instrument. I was part of the team that built the instrument, installed at the 30 metre IRAM

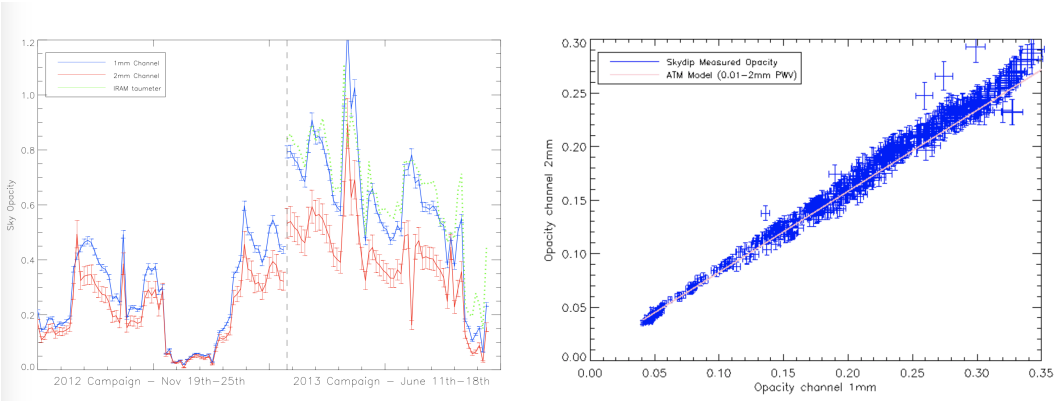

Figure 3.4: Left: atmospheric opacity evolution for the NIKA 2012 and 2013 observing campaigns calculated from the NIKA skydip technique. The error bars were estimated by analysing different skydip observations. During the 2013 observing campaign, the agreement with 225 GHz IRAM taumeter is good. Right: Comparison between the atmospheric opacities measured with the skydip technique (blue points) and an atmospherical model (purple lines) [Catalano et al.(2014)].

telescope and calibrated the instrument during the commissioning phase. In addition, I was in charge of the design, characterisation, and data analysis of the instrument configuration to measure polarisation together with Nicolas Ponthieu (IPAG).

When I first joned the NIKA collaboration in 2012 I realised that previous NIKA observational campaigns (three observing campaigns have been performed with the NIKA prototype instrument) had revealed several technical aspects that limited the sensitivity of the detectors and the overall calibration accuracy of the instrument. Some of the major aspects in particular were the real time optimisation of the detectors working point and the atmospheric absorption corrections that are crucial for reaching a high accuracy calibration. In particular, the atmospheric absorption correction was made using the IRAM tau-meter that performs elevation scans continuously at a fixed azimuth at 225 GHz. To derive the opacity at the exact position of the scan and at the same frequencies as NIKA, we implemented a procedure that uses the NIKA instrument itself as a tau-meter (see results on Fig. 3.4). An initial advantage of this method is that we do not need to perform the Skydip at the exact time of the source observations to properly correct the atmospheric contribution in the considered scan. A second advantage is that we can estimate the atmospheric opacity at the same (azimuth-elevation) position of the source, instead of the average sky opacity. Finally, with this method of correcting for the atmospheric absorption, the NIKA bandpasses are directly taken into account. This technique was implemented in the NIKA pipeline and now it is still used in the finel NIKA 2 instrument.

While the commissioning phase for observing in intensity ended in April 2017 (see Fig 3.3 that summarises the perfomance of NIKA 2) and the instrument has been opened to the astronomy community starting from fall 2017. The commissioning phase for polarisation observation is still in progress (as planned) and will end in the beginning of the next year. However, both NIKA 1 and NIKA 2 have already observed point and extended sources in polarisation producing several astrophysical results [Ritacco et al. (2015), Ritacco et al. (2017)]. With NIKA 2 in the polarisation commissioning phase, we already observed several polarised point sources (e.g. quasars) and extended sources (e.g. Crab Nebula) that allowed us to validate the whole polarisation measurement design (Fig 3.5).

Future personal implications in NIKA2: The NIKA2 instrument today is a resident IRAM instrument producing scientific observations. The Grenoble collaboration (Institut Néel, LPSC, IPAG and IRAM) is strongly involved in optimising the guaranteed time to measure the SZ

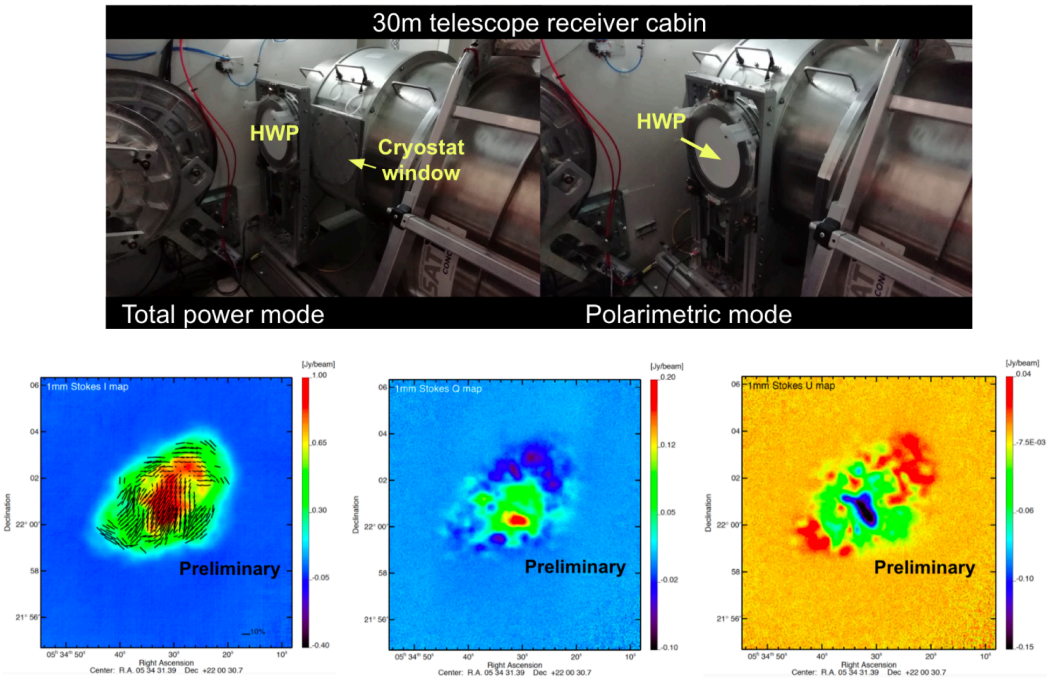

Figure 3.5: Polarisation with NIKA 2: on the top panel, the components used to measure polarisation in NIKA 2 paare presented. On the bottom panel, a preliminary result of the NIKA 2-pol is shown. From left to right: Stokes I map with polarisation vectors over-plotted where SNR $> 3\sigma$, Stokes Q map, and Stokes U map obtained at 1.15 mm.

effect for about 50 clusters. The NIKA 2 performance is beyond its original ambitions, in particular concerning the 2 mm channel. The gain "per beam" sensitivity is around 50 % higher compared to the first version NIKA. On top of that, the instantaneous field of view has been increased by a factor of 10. We estimate that in this phase of the instrument, no upgrade is needed in the instrument for the 2 mm channel. On the other hand, the 1 mm channel is just in line with the requirements. We estimate that we can improve the sensitivity by a factor of 2 by optimising the design of the LEKID array and therefore approaching its sensitivity to the photon noise level. This improvement can be done in the incoming years (to be planned with IRAM). We conclude therefore that the community using NIKA 2 would benefit from an upgrade of the instrument in this channel. In addition, this channel concerns also the polarisation mode of NIKA 2. Apart from this, for the next years my involvement in NIKA 2 will be limited to supporting the team to handle the systematics for the data analysis and helping with observations at the telescope.

3.3 New Generation Spectro-Interferometers: KISS and CONCERTO instruments

CMB spectroscopy, used to measure both the primordial CMB spectral distortion and secondary anisotropies, requires low spectral resolution and a large range in electromagnetic frequencies (at least from 80 to 300 GHz). The use of multi-chroic detectors is a natural solution because

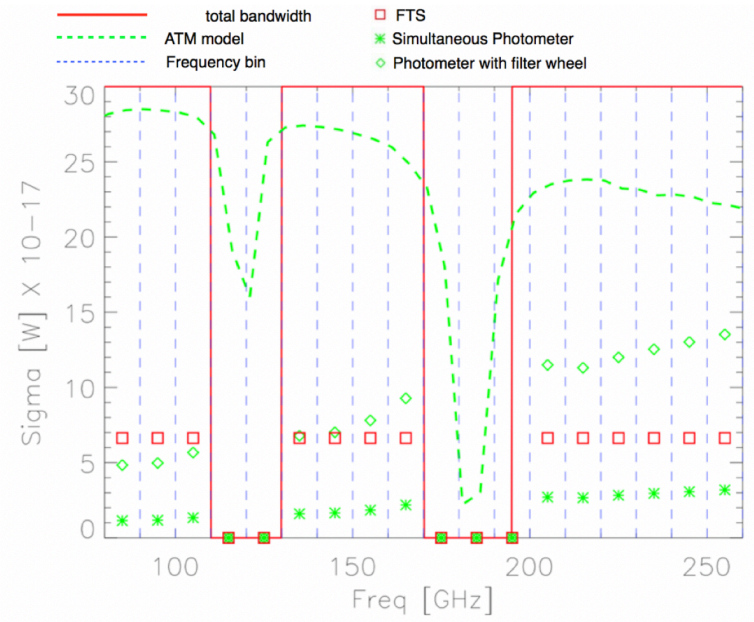

Figure 3.6: Comparison of r.m.s noise between an FTS and two different photometers observing in the same frequency domain. Given that the instantaneous *photometer has a r.m.s noise of about 5-6 times lower than the other two instruments, there are no notable differences between the* filter-wheel *photometer and the FTS.*

they increase the sensitivity while measuring different frequencies simultaneously. On the other hand, Fourier transform spectrometers (FTS) can cover a broad band and get all the spectral information with just one detector. This enormously reduces the complexity of the instrument, which makes it feasible in most cases. In this scenario, we can design a focal plane of a reasonable size observing the sky in 3-dimensions with large mapping speed. The downside is an higher noise level with respect to dispersion spectrometers. If we consider two cases, an instrument using FTS observing in a given band (χ) with a spectral resolution given by dividing the band into N bins, and a dispersion spectrometer observing with N detectors in N photometric bands covering the same χ band, we have:

$$\left(\frac{S}{N}\right)^{FTS}_{xbin} = \frac{Sig_\chi}{\sigma_\chi N}$$

for the FTS and:

$$\left(\frac{S}{N}\right)^{Spectrometer}_{xband} = \frac{Sig_\chi}{\sigma_\chi \sqrt{N}}$$

for the dispersion spectrometer, where Sig_χ is the integrated signal over the total band χ (for a signal with a flat spectral index within the band), and σ_χ is the r.m.s noise in the total band χ.

In Fig.3.6 we present a comparison of r.m.s noise per detector for three hypothetical ground-based instruments. The first instrument is a dispersion spectrometer (13 detectors observing simultaneously in 13 bands covering the whole frequency domain for an integration time of one second), labeled in the figure as *instantaneous* photometer. The second instrument is a photometer observing with one detector in 13 bands covering the whole frequency domain, each band with

an integration time 1/13 seconds (labeled as *filter-wheel* photometer). The third is an FTS (one detector observing with an FTS covering the whole frequency domain, with a spectral resolution given by the band divided into 13 bins with an interferogram scanning time equal to one second). Considering an optical load of the atmosphere (using an ATM model with PWV=2 mm), the *instantaneous* photometer has a r.m.s noise of about 5-6 times better than the other two instruments, there are no noticeable differences between the *filter-wheel* photometer and the FTS.

Observing with an FTS was successfully done by the FIRAS spectrometer, mounted on the COBE satellite [Kogut et al.(1996)], which made the first full measurement of the CMB spectrum and showed it to be consistent with pure black-body radiation. From our point of view, even from the ground, FTS instruments are still the best solution for spectrometers which requires large mapping speed and frequency coverage. A typical example is the measurement of CMB spectral distortions via the SZ effect. As presented in the first Chapter, the Sunyaev Zel'dovitch effect can manifest in two different ways: the thermal SZ (tSZ) effect, which refers to the interaction of the hot electrons in clusters with the CMB photons which results in a distortion in the CMB spectrum at the position of the cluster, and the kinetic SZ (kSZ) effect, which is a Doppler shift of the CMB photons induced by the proper motion of clusters of galaxies along the line-of-sight. The tSZ effect is particularly interesting as its spectral signature provides a unique redshift-independent way to detect and study clusters of galaxies (no cosmological dimming). Furthermore, the tSZ flux has been proved to be a good proxy of the mass of the cluster showing lower dispersion than those derived from optical, X-rays or lensing measurements. However, two issues need to be carefully addressed to do cosmology with the tSZ effect. Firstly, the complex physics of baryons can introduce significant bias in the relationship between tSZ flux and mass. Secondly, astrophysical contamination by foreground emissions (thermal dust, synchrotron, dusty and radio galaxies, CMB and others) limits the accuracy of the reconstruction of the tSZ effect (left panel of Fig 3.7). Observing the tSZ effect can be done using continuum observations with KIDs at high resolution, such as NIKA 2. For kSZ, multi-wavelength observations are needed to separate the different foreground components and to add complementary information. Indeed, with sufficiently precise spectroscopy measurements, we can independently measure the tSZ (including relativistic corrections) and the kSZ, which allows us to obtain the cluster's mass (tSZ flux), proper motion along the line-of-sight (kSZ), and temperature (relativistic corrections to the tSZ).

To achieve these goals, we are developing and constructing two spectrometers to make 3D intensity maps. The first instrument, KISS (Kids Interfero-Spectrometer Survey) hosts about 600 LEKIDs detectors operating in the frequency range 80-250 GHz. It has been installed at the end of 2018 at the 2.5 m QUIJOTE telescope at the Teide observatory in Tenerife, Spain[2]. KISS is the pathfinder for the CONCERTO instrument, which will observe at the focal plane of the Cassegrain cabin of the APEX[3] 12-metre antenna. CONCERTO will host about 4000 LEKIDs detectors operating in the frequency range 120-360 GHz. The instruments are very similar: both are based on the state-of-the-art development of new arrays observing in the millimetre band using KIDs. Both instruments are diffraction-limited with the angular resolution dependent only on the aperture antenna. Spectra are obtained using a fast Martin-Puplett Fourier-transform spectrometer (MPI) with variable resolution (tuneable from 1 GHz to 5 GHz) located in front of the cryostat, operating at room temperature. Each pixel acquires fast interferograms and will be able to extract a spectrum in 1-3 seconds integration time. Typically, faster acquisitions correspond to spectral resolution R = $\nu/\delta\nu$ =100 while slower acquisitions can achieve R=300. These instruments produce roughly one data cube containing the spectral image per second.

[2] http://www.iac.es/eno.php?op1=3
[3] http://www.apex-telescope.org

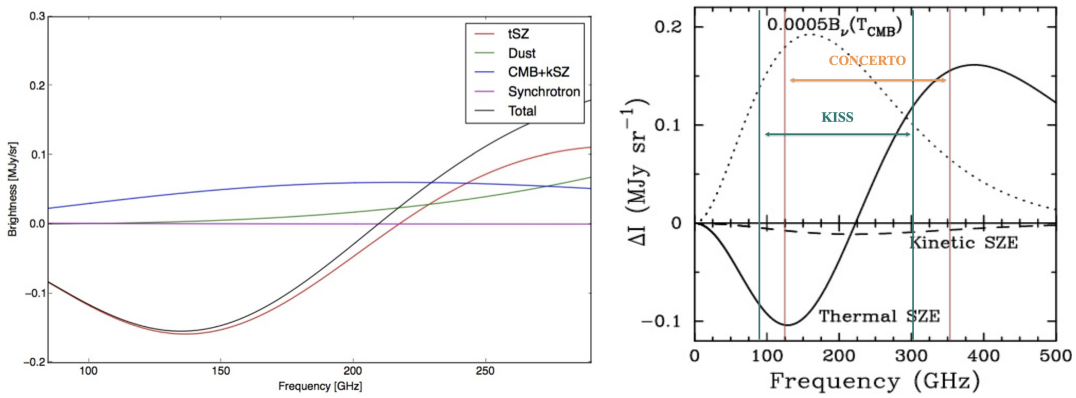

Figure 3.7: Left panel: different spectral contributions to SZ observations. Right panel: spectral coverage between KISS and CONCERTO instruments in comparison with signatures of the thermal and kinetic SZ effects.

3.4 KISS Instrument

KISS is based on two 316-pixel arrays of KIDs cooled to 150 mK by a custom dilution refrigerator-based cryostat. By using Ti-Al and Al absorbers, we can cover a wide frequency range from 80 to 300 GHz with a spectral resolution of about 1 GHz. In order to preserve a large instantaneous field of view (FoV) of 1 degree, the spectrometer is based on a fast Martin-Puplett interferometer (MPI) [Fasano et al.(2019)] [Fasano et al.(2019)]. This represents a technological challenge due to the fast scanning speed needed to overcome the effects of background atmospheric fluctuations. The design and the control of the systematic error of such a configuration drives the major requirement for the whole instrument. This is because the MPI must be able to perform continuously 10 cm path interferograms (which gives a spectral resolution of about 1 GZ within the band) at a frequency of about 4 Hz in order to maintain a low sky noise level. The fast KID time response permits us to use this method without any loss of information. The readout sampling frequency is also constrained by this requirement. We proved that few hundreds of data points for each interferogram are needed in order to preserve all the spectral information in the data in the band of interest. This means that the readout electronics has to operate at a sampling frequency higher than 1 kHz.

These requirements have been studied and a solution is presented in Fig 3.8. One of the two roof mirrors is moved by a mechanical-bearing direct-drive linear stage which meets the requirements. Mechanical vibration induced by the fast movement of MPI roof mirror can introduce a high level noise in the data. In order to achieve accurate linear movement, we use a flat spiral spring already developed for the Planck HFI 4 K compressor. In this geometry, the flexing movement is produced by arms that connect inner and outer annuli. Flexing allows the planes defined by these annuli to move easily with respect to each other by rotation perpendicular to the flexing axis, displacement, or a combination of both. When the inner and outer annuli are parallel, the displacement is along an axis perpendicular to the annuli. The movement that has the greatest resistance in this type of flexing is a relative radial movement between the two annuli. The remaining radial movement (which oscillates with an un-damped frequency proportional to the square root of the ratio between the spring constant and the mass of the system) is stopped by an eddy current brake (see Fig 3.8 on the top). It consists of a copper straight bar, which moves through the magnetic field of a permanent magnet. When the copper moves, the magnet exerts a drag force on the metal which opposes its motion, due to circular electric currents induced in the metal by the magnetic field.

Another original design adopted for KISS is the optical setup (see Fig. 3.9): since an MPI measures the difference between two optical inputs, we split the beam after passing through the

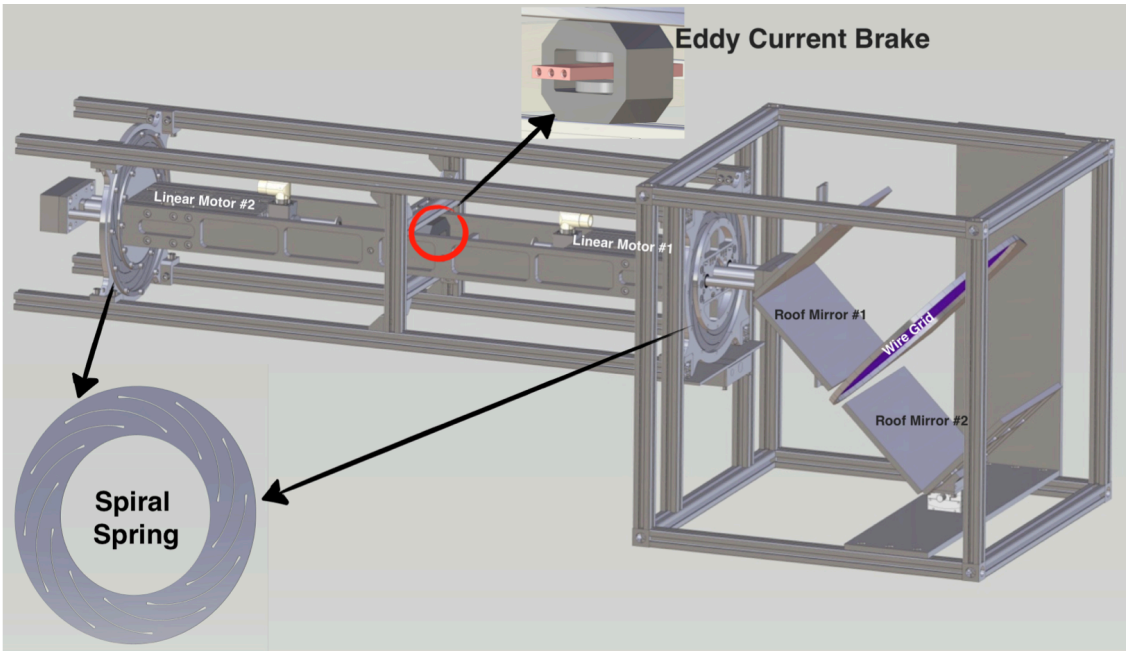

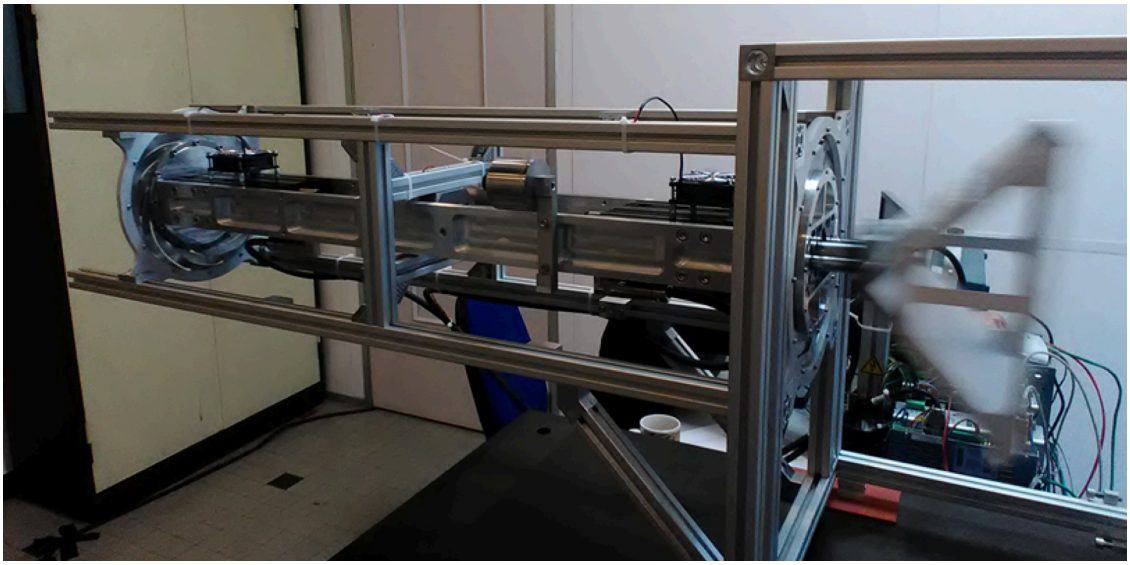

Figure 3.8: The fast MPI interferometer developed for the KISS/CONCERTO experiment. On the top, a mechanical drawing of the Martin-Puplett Interferometer. On the bottom, a picture of the actual MPI used in KISS with the roof mirror moving by 100 mm and at a frequency of 5 Hz.

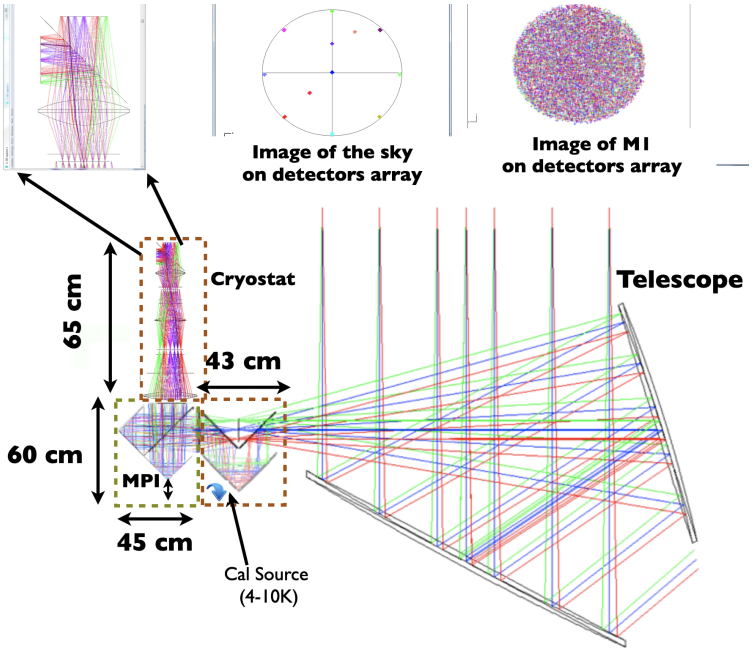

Figure 3.9: Optical scheme of the KISS instrument using the Zemax software (https://www.zemax.com).

telescope into two fully polarised beams before reaching the MPI. This can be done with the use an initial wire-grid polariser. After interfering in the MPI, the first half of the beam is focused onto the detectors, creating a image of one degree on the sky. The second half of the beam is first de-focused from a focused image to a pupil, (corresponding to the image of the primary mirror of the telescope) and then collected to the detectors. This makes an initial hardware subtraction of the constant common mode from the atmosphere to simplify the off-line analysis. In addition, instead of the sky itself, the second input can be taken from a cold reference, which can be a mirror looking at either the detectors themselves by *narcissus* effect or a cold black-body at a given tuneable temperature.

The design, the fabrication, and the testing of the whole instrument were done by LPSC and Neel Institute and the instrument demonstrated performances in line with requirements To illustrate this, in Fig.3.10 (top left) the reconstructed KISS focal planes are presented.

KISS has been installed at the QUIJOTE 2.25 m telescope in Tenerife since December 2018 and is currently in commissioning phase. We have performed several observations for calibration with sources accessible by the instrument, such as planets (Jupiter and Venus) and the Moon, to identify the pixels in the focal plane and demonstrate the multi-wavelength mapping capability. In Fig 3.10, I present some results of the calibrations: the measured focal plane geometry of the two detector arrays, a map of a point source (Jupiter), and a multi-wavelength maps (un-calibrated) in 6 GHz bins and convoluted transmission band of the Moon.

Principal contributions to KISS Instrument: I am the instrument scientist of the instrument. I participated in the design, fabrication, calibration, and data analysis of the instrument together with several management responsibilities (initiating and maintaining contacts with Tenerife staff, managing the project at the LPSC). I am the co-director of Alessandro Fasano PhD thesis (PhD viva expected for October 2020).

Prospective for the next future: The KISS instrument is installed at the QUJIOTE Telescope at the Teide observatory and it is finalising the commissioning phase. In 2020, I will be strongly involved in this project to start and consolidate the scientific observations. Obser-

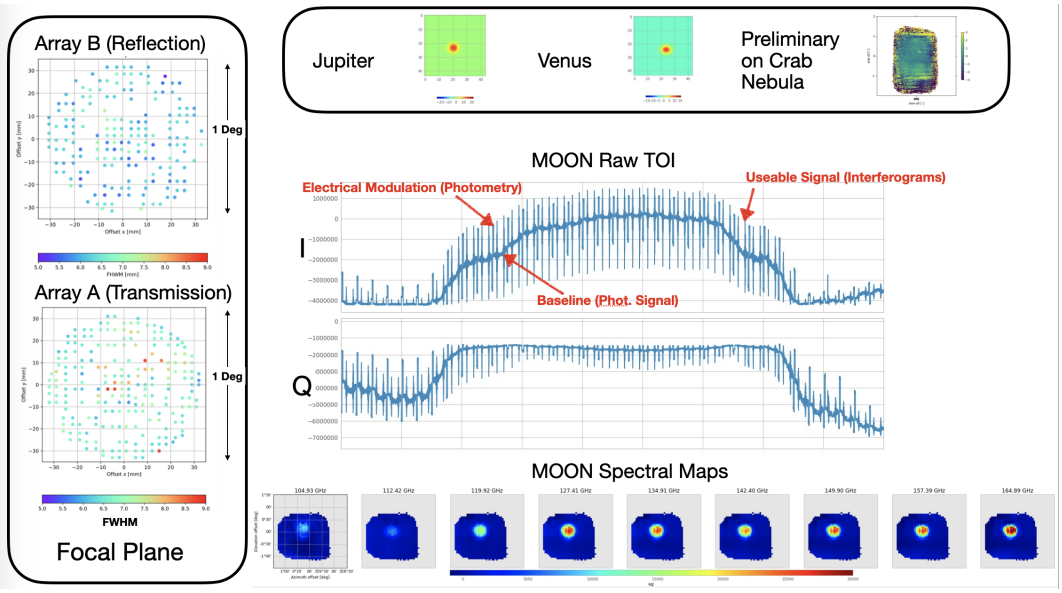

Figure 3.10: Overview of current KISS results obtained from laboratory characterisation and sky observations. On the left the focal plane geometry of the two arrays obtained from laboratory measurements is presented. More than 80 % of the pixels are viable for observations. This results has been confirmed on sky. Top panel: combined maps of Jupiter and Venus planets. Considering the angular resolution of KISS (about 7 arcmin), the two planets are the brightest observable point sources in the sky. In the same panel is also presented a preliminary combined map on the Crab Nebula. Centre-Bottom: spectral observation of the Moon with a resolution of about 6 GHz.

vations of the Crab nebula and COMA cluster are planned in the incoming months. Indeed, the goal is to keep this instrument in operation for the entirety of 2020 before the installation of CONCERTO instrument (see next section). After 2020, the instrument will be dismounted and repatriated to Grenoble.

3.5 CONCERTO Instrument

Starting from January 2019, the Grenoble collaboration together with the *Laboratoire d'Astrophysique de Marseille* (LAM) has been using an Advanced Grant ERC funding to design, fabricate, install, commission, and observe with the CONCERTO instrument, which will be installed at the 12-metres APEX telescope (ATACAMA desert in Chile). CONCERTO represents from a technological point of view a very similar instrument to KISS. For this reason, KISS can be considered as the pathfinder for the final instrument CONCERTO. Since CONCERTO will be freely available to the APEX community, the scientific goals will be manifold. However, the CONCERTO collaboration has two cosmological goals:

1) Measurement of [CII] line emission at redshift between 4.5 and 8. The atomic [CII] line is one of the most valuable tracers of star formation at high redshifts and is observed in the sub-millimetre and millimetre atmospheric windows [Kovetz et al.(2017)]. We will use the [CII] line emission as a tracer of cosmic density structure, and make the first constraints on the power spectrum of dusty star-forming matter. Our experiment will also observe the CO intensity fluctuations arising from galaxies at redshifts between 0.2 and 2, mapping the spatial distribution and abundance of molecular gas over a broad range of cosmic time.

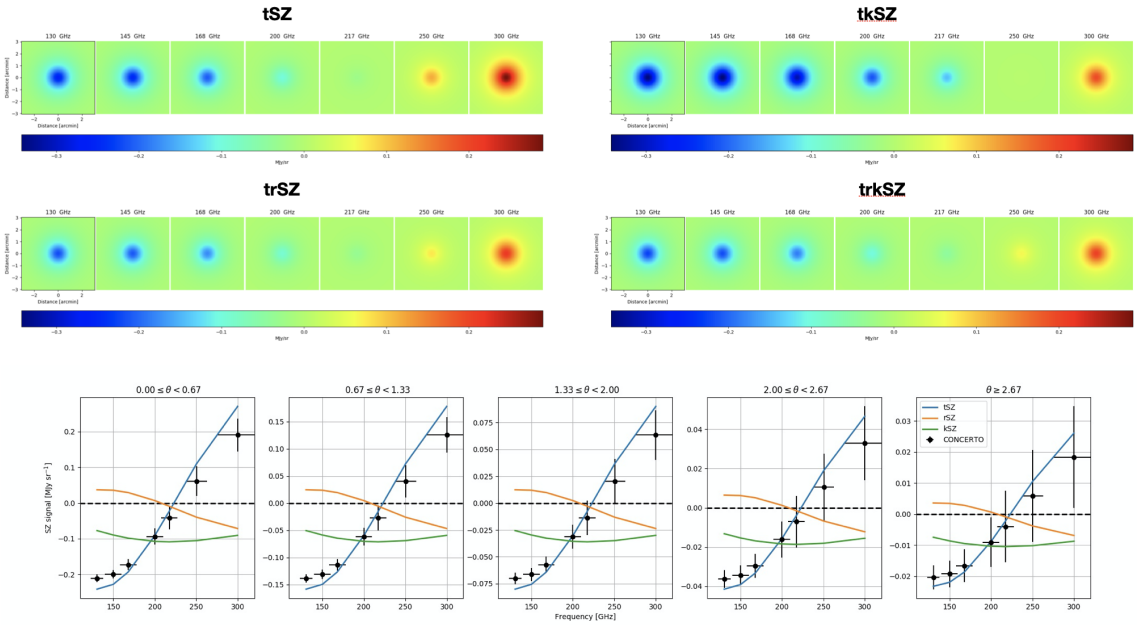

Figure 3.11: Simulation of a 10^{15} solar mass cluster at redshift z = 0.5. The simulation has been done assuming an universal pressure model [Arnaud 2010].

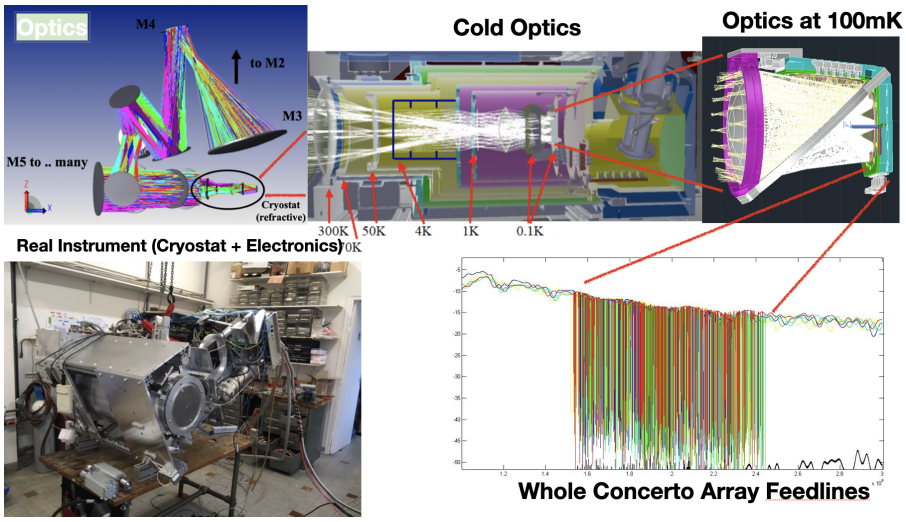

Figure 3.12: CONCERTO optical design (using Zemax software with details of the cold optics inside the cryostat and the 100 mK stage cold pupil, polariser and the two arrays). The entire baseline sweeps for one array from VNA scans are presented (bottom right panel). Finally on bottom left a picture of the fabricated CONCERTO cryostat and warm electronics are presented.

2) Precise estimation of the shape of the SZ electromagnetic spectrum for cluster of galaxies for redshifts between 0.2 and 0.8 by disentangling the kinetic and relativistic corrections from the main thermal contribution. In Fig. 3.11 we present a typical cluster which can be observed by CONCERTO. In this simulation the mass of the cluster is equal to 10^{15} solar masses and the cluster is located at a redshift of z = 0.6. In the figure we show four different cases:
- The signal expected for a cluster of T = 5 keV, which comes mainly from the tSZ.
- For tSZ + kSZ. Where kSZ is the kinetic contribution calculated for a cluster which is moving at 2000 km/h towards the observer. From left to right, we present.
- For a cluster of T =20 keV where we take into account the relativistic contribution.
- For tSZ + rSZ + kSZ.

In the maps presented on the bottom panels of Fig. 3.11, we present the simulated CONCERTO SED including uncertainties (black dots) for different radial bins with respect to the center of the cluster. We add the different SZ contributions (thermal (blue), kinetic (green) and relativistic (orange)).

The results show we will be able to detect the SZ contributions to the relativistic corrections and/or the kinetic contribution with CONCERTO with an integration time of about 40 hours. We can select few clusters that seem to show some level of relativistic or kinetic contribution detectable with CONCERTO but not with NIKA 2. This will be part of the scientific program of CONCERTO, using 150-200 hours of the telescope time.

The current plan for CONCERTO is deployment to the APEX telescope, which is a 12-m antenna located at a 5105 m altitude on the Llano de Chajnantor in Northern Chile. The instrument is based on a dilution cryostat, not requiring liquid helium or nitrogen, and is able to assure continuous operation, i.e. no cryostat recycling or other dead time. The field of view is 20 arcmin. Spectra are obtained using a Martin-Puplett Fourier-transform spectrometer with variable resolution (tuneable from 1 GHz to 5 GHz) operating at room temperature in front of the cryostat (see Fig. 3.12 for a general view of the instrument). Such a fast (compared to the atmospheric noise) spectrometer can now be used to get the spectra thanks to the very small response time (less than 0.1 msec) of KIDS. Typically, faster acquisitions correspond to a spectral resolution of $R = \frac{\nu}{\delta\nu} \approx 100$, slower ones reach $R \approx 300$. CONCERTO will produce roughly one data cube per second, which contains the spectral image.

Principal contributions on CONCERTO Instrument: I am the scientific coordinator of the project at the LPSC which is heavily involved in this development. The LPSC is in charge of delivering the warm electronics to read out the kilo-pixel KID arrays, several electronics sub-systems (actuators control, MPI movements, temperature control), the optical design, the fabrication of the mirrors and the lenses, and it will lead the SZ scientific program. Dozens of people are involved in the project at the LPSC in the context of technical services and researchers.

Perspectives for CONCERTO Instrument: In the coming years, one of my top priorities will be the deployment and the commissioning of the CONCERTO instrument. The instrument is proposed for installation in the C-cabin of the APEX antenna in 2021. Currently, we are mounting the instrument and characterising the cryostat, optics and electronics in lab. We can distinguish several key tasks to complete in the coming years:

- *Validation of the sub-systems (10/2019 - 02/2020) :* The CONCERTO instrument is composed of several sub-systems (dilution cryostat with optical filters, lenses and a wire-grid, interferometers Martin-Puplett, nine mirrors, two wire-grids, a fluid circulation system, a 4 K pulse tube with a water-cooled commercial compressor, a router, two DAQ computers, one RTA computer and data storage space). All these sub-systems has to be characterised and validated before being assembled into the final instrument. This work is in progress now. I am strongly involved with both the electronics technical services at the LPSC and the Neel Institute researchers and technical services.

- *Assembly (02/2020 - 07/2020) :* We have already begun to mount all the sub-systems in the final easily-movable *CHASSIS*. This is a critical step because of critical and complex interfaces between sub-systems and auxiliary equipment involved in this process.

- *Laboratory Characterisations (08/2020 - 12/2020) :* A first characterisation of the properties of the instrument as a whole must be done in laboratory to check carefully if the instrument meets the expected requirements (or goals). In order to replicate real observing conditions and properly estimate the amount of stray light onto the detectors, we have built a *sky simulator* which consists of cooling down a large, black disk with the same dimensions

as the telescope focal plane. This cold disk emulates the background temperature under normal ground-based observing conditions. To simulate an astronomical source, a high-emissivity ball with a diameter of 5–10 mm (which corresponds to a point source signal on detectors) was placed in front of the sky simulator window at room temperature. The ball is mounted on a motorised XY stage enabling movement with respect to the fixed disk. The laboratory has a stock of other devices, such as Gunn diode sources, to characterise the spectral capabilities of the instrument. In addition, the frequency scale of the CONCERTO FTS will be determined by the position of the moving roof mirror and the associated uncertainty is determined by how accurately the positions can be measured and converted into optical path difference.

- *Shipping and installation at the APEX telescope (12/2020-03/2021) :* The instrument is scheduled to be installed at the APEX telescope in the beginning of 2021. It will take about one month.

- *Technical and Scientific Commissioning (03/2021 - 12/2021) :* The technical commissioning (sanity check, rough focal plane geometries, rough calibration, rough pointing model) will start soon after installation. In the best case scenario, we will need two weeks to complete the technical commissioning before the start of the science commissioning (final pointing model, spectral calibration, fine photometric calibration, fine focal plane geometries, etc.). The first step of the on-sky commissioning is to perform several series of focus, pointing, beam map, skydip to refine the pointing model, reconstruct the focal place geometry and perform absolute photometric calibration (using the combination of the skydips and a beam map on a planet). Relative spectral photometric calibration will be done using a strong source with a known spectral energy distribution (SED). The two bandpass filters (low frequency and high frequency) will be measured using two black-bodies (one at each input port). However, they will need to be measured on sky for different opacities, using a planet. We will then observe secondary photometric calibrators, and check the stability.

  Part of the on-sky commissioning can be performed before summer 2021. Our ultimate goal is to make CONCERTO and its data reduction freely available to the APEX community by the end of 2021.

- *Scientific Observations (01/2022 - 12/2025):*

  The regular science observations ([CII] survey and SZ observations) will be controlled remotely with just one person from the CONCERTO collaboration in the APEX sequitor site. There is not a fully detailed agreement on the observing time dedicated to the principal scientific programs ([CII] survey and SZ observations). Roughly, we estimate 600 hours between the two programs.

Bibliography

[Abazajian et al. 2019] Abazajian K., Addison G., Adshead P., et al.,2019,arXiv,arXiv:1907.04473

[Thornton et al. 2016] Thornton, R. J. et al. The Astrophysical Journal Supplement Series 227.2 (2016): 21.

[Barron et al. 2014] Barron D., Ade P., Anthony A., et al.,2014,JLTP, 176,726

[Castro et al. 2009] Castro, P. G. et al. The Astrophysical Journal 701.2 (2009): 857–864. Crossref. Web.

[Perotto et al.(2019)] Perotto, L., Ponthieu, N., Macías-Pérez, J.-F., et al. 2019, arXiv e-prints, arXiv:1910.02038

[Adam et al.(2018)] Adam, R., Adane, A., Ade, P. A. R., et al. 2018, A&A, 609, A115

[Catalano et al.(2014)] Catalano, A., Calvo, M., Ponthieu, N., et al. 2014, A&A, 569, A9

[Pointecouteau et al. (2015)] Pointecouteau E., Allen S., Ota N., Athena SWG1. 1,2015,eheu.conf,13

[Ritacco et al. (2015)] Ritacco, A. et al. 2015, A&A, 16, 1602.01605

[Ritacco et al. (2017)] Ritacco, A. et al. 2017, A&A, 599, A34, 1609.02042

[Kogut et al.(1996)] Kogut, A., Banday, A. J., Bennett, C. L., et al. 1996, Astrophysical Journal, 470, 653

[Kogut et al. (2011)] Kogut, A., Fixsen, D. J., Chuss, D. T., et al. 2011, J. Cosmology Astropart. Phys., 7, 25

[Fasano et al.(2019)] Fasano, A., Aguiar, M., Benoit, A., et al. 2019, Journal of Low Temperature Physics, 362

[Fasano et al.(2019)] Fasano, A., Aguiar, M., Benoit, A., et al. 2019, arXiv e-prints, arXiv:1911.04917

[Kovetz et al.(2017)] Kovetz, E. D., Viero, M. P., Lidz, A., et al. 2017, arXiv e-prints, arXiv:1709.09066

[Arnaud 2010] Arnaud M.,2010,gcop.conf,16

4

Next-Generation Space-Borne Experiments

In the previous chapter, we listed all the advantages in observing with ground-based instruments. Of course, the other side of the coin is the science goals that are only feasible with observations from space. First of all, a satellite avoids all the problems from the absorption and contamination of the atmosphere. This allows observations to be made at any wavelength without any limitations. This represents a huge advantage since multi-frequency measurements reduce the contamination of astrophysical foregrounds (which obviously cannot be eliminated even with space observations). In addition, the stability of the optical load is almost perfect and it is possible to make surveys of the whole sky. Other than higher expenses, limitations of these experiments are only defined by the state of technology used. Indeed, an instrument that observes from space, must work perfectly for several years, be remotely controlled by telemetry, and have no access to any interventions or maintenance. All this makes designing space instruments extremely challenging, often at the expense of technological development; that is to say, a solid and reliable technology (which is measured in TRL, Technology Readiness Level) is heavily favoured. Most of the time, this means using legacy technologies which are already outperformed by new existing prototypes, which instead can be mounted on the ground-based experiments.

There is a strong competition in the development of future millimetre space missions, for which I am an active participant. Over the past few years, our team in Grenoble has concentrated our efforts of the optimisation of KIDs' performance to become a viable candidate for the next generation of satellites devoted to CMB observations.

In order to accomplish these goals, KID detectors must be optimised and tested under several conditions. Indeed, the specific detailed requirements on individual detector arrays will heavily depend on the final design of the focal plane instruments' characteristics, such as the optical load, frequency range, coverage of the focal plane (filled arrays, or horned-coupled detectors), strategy of polarization measurements, and cosmic ray susceptibility. This will allow us to identify the main challenges in the detector technology.

In particular, our group has focused on three main programs of R&D:

1. Widen the spectral coverage of KIDs detectors to a 80-600 GHz band

2. Optimise LEKIDs performance under low optical background conditions that are typical of space environment (from 0.2 to 4 pW)

3. Characterise the impact of ionizing particles on LEKIDs

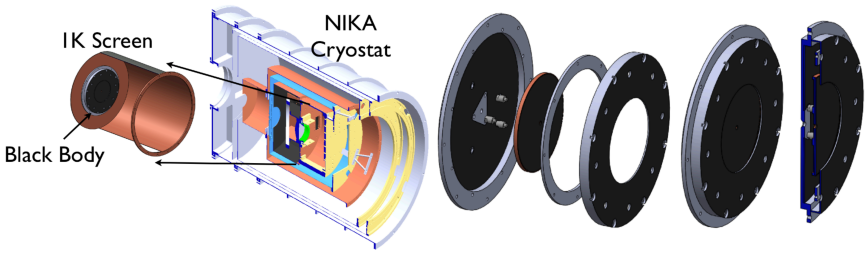

Figure 4.1: Top: 3D drawing of the dilution cryostat used for the tests. The black-body is mounted at the end of the still screen, at a base temperature of around 1 K. Bottom: Closeup of the cryogenic back-body.

These programs have been funded by CNES during the last five years and are developed by a team composed of laboratories of the Grenoble collaboration (LPSC, Néel and IPAG). I led two of these three CNES R&T - programs 2 and 3).

In the following sections I will describe the details of the main results of these programs.

4.1 LEKID sensitivity for space applications between 80 and 600 GHz

When operating above the atmosphere, an instrument covering the band 80-600 GHz is loaded mostly by the 2.72 K CMB and the thermal radiation of the interstellar dust. In addition, above roughly 300 GHz, the instrument itself becomes an important source of optical load due to the thermal emission of the telescope [Planck Collab & Lawrence (2011)]. The optical power loading a pixel, for typical configurations (e.g. Planck, LiteBIRD), is within the range of 0.1-1 pW, depending on the considered bandwidth and other factors like the instrumental throughput. The noise equivalent power (NEP) needed is at least one order of magnitude lower compared to the ground-based case. For this work, we define our goal NEP per pixel:

$$NEP_{goal} \leq \sqrt{2} \cdot NEP_{phot} \tag{4.1}$$

where NEP_{phot} represents the source of noise related to the photon noise[1]. $\sqrt{2}$ means that we require that all the other sources of instrumental noise to not exceed the photon noise level. When this condition is satisfied, we refer to the devices as photon-noise dominated detectors.

In order to reproduce space conditions for each band we used a dilution cryostat operating at 100 mK and equipped with a cryogenic black-body installed on the 1 K stage. The black-body can be regulated, via a standard PID procedure, between 1 K and 20 K. This has no impact on the thermal stability of the coldest stage and the detectors. The black-body (see Fig. 4.1) is composed of: a) an aluminium support covered by black stycast glue, b) three Vespel legs, c) a copper disk covered by carbon-doped black stycast, and d) a metallic support to hold the band-defining filters. The copper disk, with its highly emissive coating, represents the actual black-body. The geometry has been studied in order to minimise the thermal capacitance and ensure a good isotherm behaviour of the emissive part. The Vespel legs have a purely mechanical role, and

[1]The photon noise comes from the intrinsic fluctuations of the incident radiation that are due to the Bose-Einstein distribution of the photon emission. In the best-case scenario, the contribution of photon noise is the limit of sensitivity of the instrument

presents a negligible thermal conductance. A calibrated, and easily replaceable, thermal link is thus added to adjust the time constant.
In order to focus our efforts, the arrays have been optimised for five different bands: 80-120 GHz (centred on 100 GHz), 120-180 GHz (centred on 150 GHz), 180-270 GHz (centred on 240 GHz), 320-400 GHz (centred on 360 GHz), and 450-650 GHz (centred on 550 GHz).

The five spectral bands are defined by low-pass, high-pass, or band-pass metal mesh filters. For the detectors covering the 3 mm and 2 mm bands, the low-frequency cutoff is provided by the superconductor film itself (see Sec. 4.1.2).

The optical loading per pixel is equal to:

$$W_{pixel} = \tau \int_0^\infty A\Omega\chi(\nu)B(\nu,T)d\nu$$

Where:

- $A \cdot \Omega$ is the throughput of the system. A is the area of the 100 mK cold stop, through which the black-body is observed. Ω is the solid angle between the cold stop and the pixel.

- τ is the overall transmission, mostly the transmission of the optical filters used to select the spectral bands. This parameter has been characterised by the Cardiff team who provided the filters and is between 90 and 95 %.

- $\chi(\nu)$ is the measured spectral band, normalised to 1 to the peak, where we assume 100 % absorption. This assumption has been demonstrated by reflection measurements using a network analyser [Roesch et al.(2012)].

- $B(\nu,T)$ is the brightness of the black-body at the working temperature. We assume an ideal emissivity across the whole band.

In Fig 4.2, we present the results of an optical simulation of this setup. In particular, we show the optical power per pixel integrated in the specific spectral band.

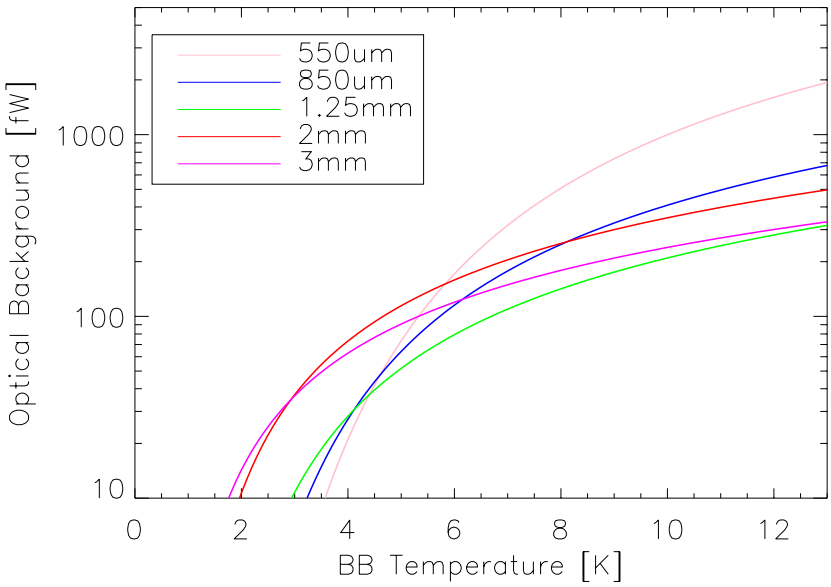

Figure 4.2: Estimation of the optical power per pixel as a function of the temperature of the cold black-body.

4.1.1 Design and fabrication of the LEKID arrays

Current arrays are made to have around hundred pixels each, and are completely multiplexed, i.e. a single readout line can readout one full array.

We have specifically designed and fabricated arrays optimised for low background, i.e. 0.1-1 pW per pixel, and for five distinct spectral bands centred on wavelengths of 3, 2, 1.25, 0.85 and 0.55 mm. The final designs are the result of extensive electro-magnetic (transmission-line model, planar and full 3-D) calculations and simulations. The detectors that have been used are back-illuminated LEKID, i.e. LC resonators made by a long meandered inductor terminated at both ends by an interdigitated capacitor. Most of the arrays are based on thin aluminium films (t_{FILM} = 15-18 nm), with a critical temperature $T_c \approx 1400$ mK, corresponding to a cutoff frequency of about 110 GHz. On the other hand, the array operating at 3 mm uses a titanium-aluminium film (t_{FILM} = 35 nm, with t_{Ti} = 10 nm and t_{Al} = 25 nm) with T_c = 900 $\pm$ 25 mK. For a standard Mattis-Bardeen superconductor, this results in a theoretical cutoff around 70 GHz [Catalano et al.(2015)]. The LEKID planar design's details mostly result from adaptations and optimisations starting from the pixels designed for the NIKA 2 instrument [Monfardini et al.(2015)]. One of the most important resonators parameters determined from planar simulations is the coupling quality factor of the resonators which was set to be in the range of $Q_c \approx 5 \cdot 10^4 - 10^5$ for this work.

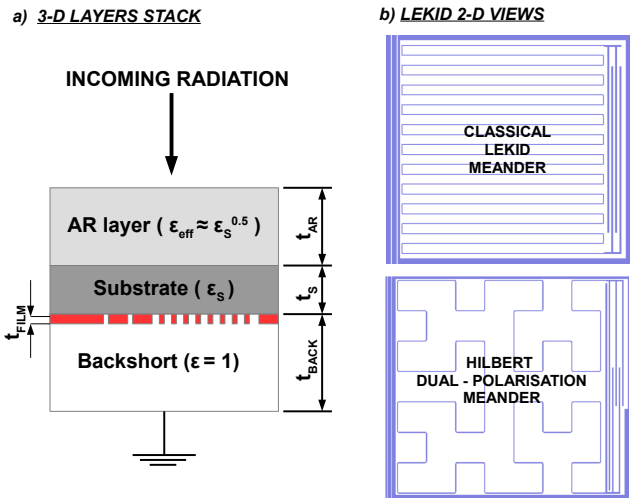

Figure 4.3: a) LEKID 3-D stack. In red, the superconducting film (thickness not-to-scale). The micromachined AR has been realised only on silicon substrates. The backshort lid is superconducting to avoid affecting the quality factor of the resonators; b) the two kinds of planar LEKID designs adopted: the classical (CL) meander and the Hilbert (H) dual-polarisation structure.

In Fig. 4.3, we present the three dimensional layout and examples of the LEKID planar views. As far as the optical coupling efficiency is concerned (left part of Fig. 4.3), the key variables to be calculated include the substrate (high-resistivity HR silicon or sapphire) thickness t_S, the thickness and effective dielectric constant of the anti-reflecting (AR) layer t_{AR}, ε_{AR} (only for silicon substrates), the thickness of the vacuum backshort t_{BACK} and the effective impedance of the superconducting (Al or Ti-Al) film as seen by the incoming wave. This last parameter is strongly related to the superconducting material(s) properties, and the thickness of the film t_{FILM}. As an example, we show in Fig. 4.4 a transmission-model estimation of the optical efficiency of the 3 mm array when varying t_{BACK}.

The 2-D planar structures printed in the superconducting film (right part of Fig. 4.3) are designed to ensure a good optical coupling and satisfy the circuit requirements in terms of things like quality factor and position of the resonance f_0. For the present study, we have adopted LEKIDs

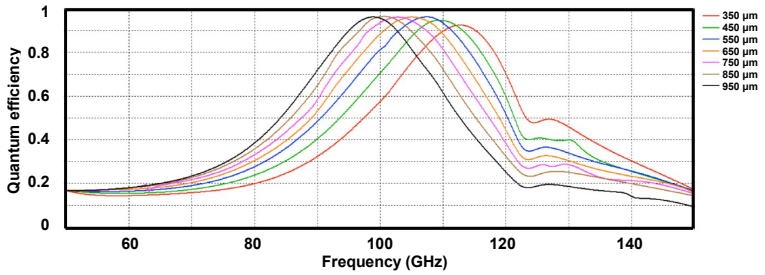

Figure 4.4: Transmission-line model calculation to optimise, in terms of the pixel quantum efficiency, the backshort distance t_{BACK} for the 3 mm array. The optimum value is established at $t_{BACK} \approx 750\ \mu m$.

with f_0 =1-3 GHz. The main geometric characteristics of the arrays are presented in Tab 4.1.

The fabrication process is similar for all arrays. The substrate (either HR Si or C-cut Al_2O_3) is prepared by applying an HF vapour cleaning. The superconducting film is deposited by e-beam evaporation and under a residual chamber pressure of $5 \cdot 10^{-8}$ mbars. In the case of the 3 mm array, the titanium and aluminium layers are deposited in sequence without breaking the vacuum. The deposition rates are within the range $0.1 - 0.5$ nm/sec. The UV photo-lithography step is done using a positive resist, and is followed by wet etching using a standard aluminium etching solution based on a diluted H_3PO_4/HNO_3 mixture. A dip in 0.1 % HF, to etch the underlying titanium film, is added for the 3 mm array case. The arrays made on silicon substrates undergo the AR-layer step by dicing, on the back of the Si wafer, a regular cross-pattern of grooves [Goupy et al.(2016)].

The diced and eventually AR-coated detectors are packaged in custom holders and bonded using superconducting aluminium wires (dia. 17 μm). The detector is connected via SMA connectors to the high-quality coaxial cables and a cold low-noise amplifier to be readout with the external multiplexing circuit [Bourrion et al.(2012)].

4.1.2 Detectors characterisation

The arrays described in Sec. 4.1.1 were first tested with the cryostat closed and the detectors illuminated by the cold black-body. The results of these measurements are shown in the sections 4.1.2 and 4.1.3. In order to correctly establish a NEP (Noise Equivalent Power) calculation, we

Wavelength	3 mm	2 mm	1.25 mm	850 μm	550 μm
Frequency	100 GHz	150 GHz	240 GHz	360 GHz	550 GHz
Film material	Ti-Al	Al	Al	Al	Al
Film thickness [*nm*]	10-25	18	15	15	15
Critical temperature [K]	900	≈ 1.3	1.45	1.45	1.45
Substrate material	Al_2O_3	Al_2O_3	Si	Si	Si
Substrate thickness [μm]	430	330	280	265	170
AR layer thickness [μm]	0	0	110	110	80
Backshort thickness [μm]	750	670	530	350	400
LEKID meander type	CL	H	H	CL	CL
Pixel size [mm]	2.3	2.3	1	1	1
Design pixels/array [#]	132	132	132	128	128

Tableau 4.1: Main characteristics of the arrays.

have then spectrally characterised the very same arrays. For that, the full cryostat optics is installed, and the camera is interfaced with the FTS. These experiments are described in more detail in Sec. 4.1.2. In addtion, the 3 mm array was tested with our fast, i.e. 1 MHz sampling, homodyne electronics to determine the LEKID response time constant (see Sec. 4.1.2). For space instruments which are exposed to a considerable flux of primary cosmic rays, the speed of response is a crucial parameter [Masi et al.(2019)], [Catalano et al.(2016)].

Resonators electrical properties characterisation

The 132 LEKIDs of the 3 mm (Ti-Al, t_{FILM} = 10-25 nm) and the 2 mm (Al, t_{FILM} = 18 nm) arrays (pixels size 2.3 mm) resonate between 1.4 and 1.9 GHz. They have average internal quality factors of 4.8×10^4 and 6.2×10^4, respectively, under typical CMB loading. The critical temperature of the Ti-Al film is measured by monitoring the readout line transmission, while slowly warming up the coldest stage of the cryostat. The transition is clearly observed at 900±25 mK, in good agreement with expectations. The transition is then crossed multiple times in both ways (warming-up and cooling-down) in order to exclude potential thermal drifts. The normal-state sheet resistance of the Ti-Al bilayer has been independently measured at T=1 K. The result is $R_N^{Ti-Al} = 0.5$ Ω/square.

The 132 LEKID of the 1 mm (Al, $t_{FILM} = 15nm$) array (pixels size 1 mm) resonates between 1.7 and 2.1 GHz. They show average internal quality factors of 5.0×10^4. The superconducting transition temperature of the 15 nm film is 1450±50 mK, while the normal-state sheet resistance is $R_N^{Al} = 2$ Ω/square.

The normal-state sheet resistance (measured) is related to the critical temperature (measured) and the surface inductance through the relation [Leduc et al.(2010)], $L_s = \frac{\hbar R_s}{\pi \Delta}$, where Δ is the superconducting gap defined as $\Delta = 1.764 \cdot k_B \cdot T_c$ for BCS ideal superconductors. The surface inductance has been estimated from electro-magnetic simulation, in order to explain the observed position of the fundamental resonance frequency. In the case of the Ti-Al film, we found $L_s \approx 1$ pH/square. The three electrical values (Δ, L_s and R_s), measured or estimated with independent methods, satisfy the cited relation to within 10 %.

Spectral characterisation

The spectral response has been measured using a custom built Martin-Puplett Interferometer (MpI) interfaced to the camera (cryostat) containing the detectors. The optics configuration for this measurement is shown in Fig. 4.5. Infrared-blocking filters are installed on the 300 K, 150 K and 50 K cryogenics stages. Metallic multi-mesh low-pass filters are placed at 50 K, 4 K and 1 K. The band-defining filters, again metallic multi-meshes, are installed at base temperature, i.e. around 100 mK, in front of the array.

In order to maximise the signal to noise ratio of the interferogram, we modulate the input signal between two distinct Rayleigh-Jeans spectrum sources held at different temperatures. The modulation is achieved by a rotating wire-grid polariser which also produces the fully polarised input signal. The signal is then extracted with a standard lock-in detection.

The measured band transmissions are presented in Fig. 4.6. The five spectral bands span the whole range of frequencies from 70 GHz up to 630 GHz, via adjacent bands with relative FWHM between 15-30 %. The relative bandwidths are mostly limited by the optical filters that were available.

Dynamical response characterisation

In order to measure the characteristic response time of LEKID under typical CMB radiation loading we have recorded some fast high-energy events on the 3 mm array. These events are generated

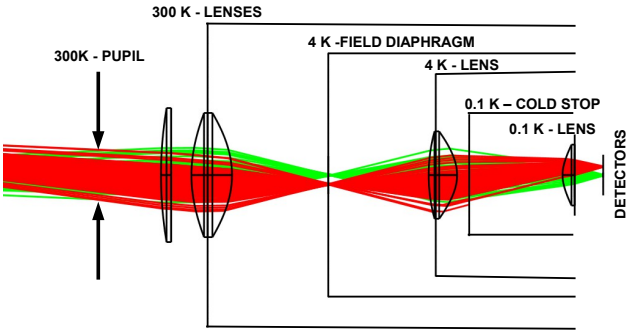

Figure 4.5: Schematic of the optics adopted for the spectral characterisation. The lenses are made out of HDPE (High Density Polyethylene). The low-pass and thermal filters positions are not shown. The interferometer input window is located at the 300 K pupil position.

by secondary cosmic rays (muons) reaching the ground and crossing the monocrystalline substrate. As a result of this ionising track, a-thermal ballistic phonons are generated in the crystal. A fraction of these phonons is energetic enough to break Cooper pairs in the superconductor film, generate lossy quasi-particles and change the kinetic inductance of the resonator [Swenson et al.(2010)]. By fitting the decay time of the spikes, we derived the quasi-particles recombination time constant in the Ti-Al film that coincides with the response time for these pair-breaking detectors. We present in Fig. 4.7 a typical cosmic-ray event. The energy that is deposited by the muon in the substrate is on the order of hundreds of keV. A small fraction, i.e. less than 1 %, of this energy is converted to breaking Cooper-pair at the particular pixel position. Considering the full sample of recorded pulses, and fitting each decay constant, we measure $\tau_{response} = 290 \pm 35 \mu$s. As expected, this time constant is higher with respect to the one seen on the same kind of pixels operating under higher loading, i.e. higher density of quasi-particles. For example, we have observed in the past shorter time constants of the order of tens of microseconds under typical ground-based backgrounds. However, a time constant of around 0.3 ms is still fast enough for a CMB space-borne mission in order to avoid introducing significant systematic errors [Catalano et al.(2016)], [Monfardini et al.(2016)].

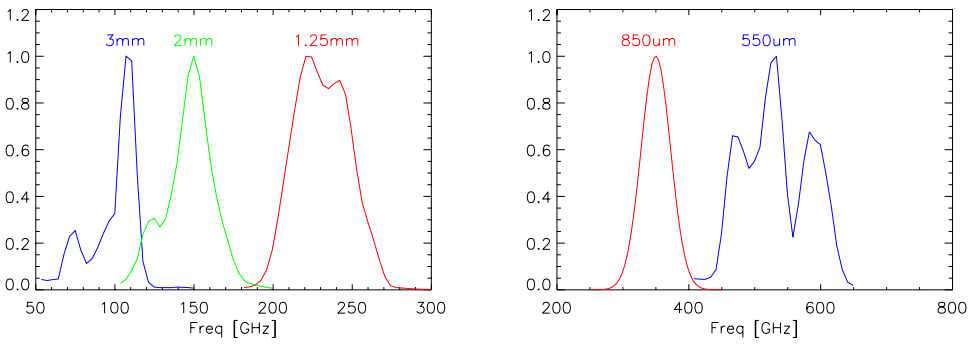

Figure 4.6: Normalised spectral response (averaged over the pixels of the same array) for the 5 arrays. The dispersion level between pixels is on the order of a few percent. The dip at 556 GHz is an artefact from a strong and well-known water vapour absorption line.

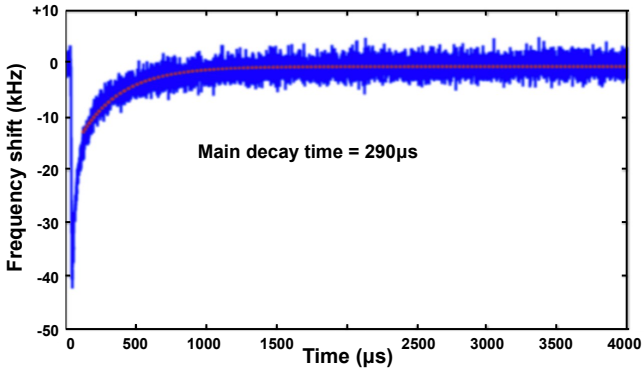

Figure 4.7: One representative cosmic-ray (muon) pulse showing a main decay time of around 0.3 ms. Trace recorded by fast (1 MHZ sampling) homodyne electronics on a typical LEKID of the 3 mm array (Ti-Al film). Array were operated under typical CMB optical background.

4.1.3 Sensitivity characterisation

The response of each detector (pixel) has been measured by performing, under stable conditions and for several black-body temperatures (T_{BB}), frequency sweeps to measure the LEKID transfer function ($\frac{\Delta f}{\Delta T_{BB}}$). The pixel responsivity is then obtained as the ratio between the frequency shift and the corresponding change of the optical background:

$$\Re esp(T_{BB}) = \frac{\Delta f}{\Delta W_{opt}}$$

Where W_{opt} is derived from the model presented in Fig. 4.2. In parallel, we measured the spectral frequency noise density $S_n(f)$, expressed in $Hz/\sqrt{Hz}$, for each T_{BB}. In Fig. 4.8 we show a typical noise (raw) measured for the 2 mm array and with T_{BB}=6 K. The correlated electronic noise is removed by subtracting a common mode obtained by averaging the Time-Ordered-Data (TOD) of all detectors. The resulting template is fitted linearly to each TOD. The best-fit is then subtracted from the detector TOD. After decorrelation, the spectral noise density is nicely flat in the 1-10 Hz band. Depending on the array and T_{BB}, the frequency noise level sits between 2 and 10 $Hz/\sqrt{Hz}$.

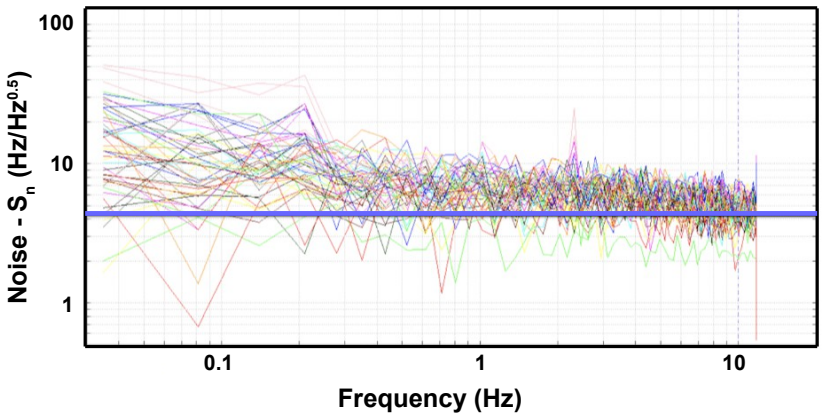

Figure 4.8: Noise density for all the pixels of the the 2 mm array. Measured with a cold black-body temperature of 6 K. The blue line represents the average noise level after common mode decorrelation.

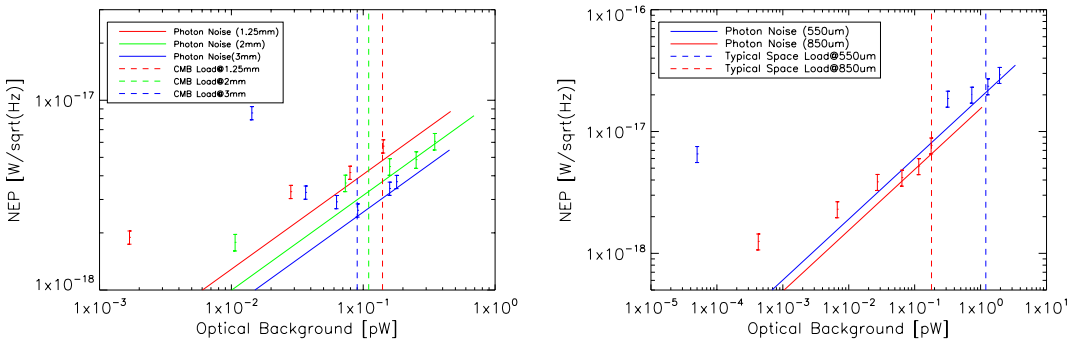

Figure 4.9: Noise Equivalent Power (NEP) per pixel (averaged over best 30% of the array) measured for the 1 mm, 2 mm and 3 mm arrays (left) and 550, 850 µm (right). Each point is derived from responsivity and noise measurements for different temperatures of the cold black-body. From each temperature, the corresponding optical load per pixel is derived using the optical simulation presented in Fig. 4.2. The vertical dashed lines represent the typical optical background expected from a real instrument operating at second Lagrangian point of the Sun - Earth system (chosen by the Planck satellite and target orbit for next generation spaceborne experiments).

The NEP is then derived as:

$$NEP = \frac{S_n(f)}{\Re esp}$$

Fig. 4.9 shows the NEP for all the arrays and as a function of the optical background. We compare these results to the corresponding expected NEP_{phot} derived for CMB in a space environment (see also Tab. 4.2). The results indicate that the NEPs approach the goal (defined in Eq. 4.1) in the range of CMB loading for all the arrays (bands) presented in this study. For higher optical loads, the measured NEP scales correctly. For lower optical loads, on the other hand, the expected NEP does not scale with the theoretical photon-noise. This discrepancy is likely due to the fact that our optical setup can introduce an additional background when running at fW-per-pixel levels. A deeper investigation of this background regime is not done for the moment. It is for sure

Wavelength	3 mm	2 mm	1.25 mm	850 µm	550 µm
Frequency	100 GHz	150 GHz	240 GHz	360 GHz	550 GHz
Optical Load [pW/pixel]	0.09	0.11	0.14	0.18	1.2
T_{BB} [K]	5	5	8	7	11
Averaged Optical Resp [kHz/fW]	2.3	0.78	1.1	0.84	0.19
Averaged Noise (1-10 Hz) $[Hz/\sqrt{Hz}]$	6	3	6.5	5.5	4
NEP $[aW/\sqrt{Hz}]$	2.6±0.4	4.0±0.4	5.5±0.5	5.2±1.1	23±3.5
NEP_{Phot} $[aW/\sqrt{Hz}]$	2.45	3.4	4.8	5.0	21

Tableau 4.2: Main results of the study: optical power, noise and derived NEP for a given optical load of a typical space environment. The averaged optical response and noise is derived over the best 30 % of the pixels for the arrays at 3 mm, 2 mm and 1.25 mm. In the case of 850 µm and 550 µm arrays, we have considered the best 10 % of the pixels. NEP_{Phot} is calculated from the photon noise at the given optical load.

interesting for other applications than space detectors devoted to CMB observations.

4.2 Characterization of the impact of ionizing particles on LEKIDs :

The impact of cosmic rays is another essential point to consider in the very early phase of the design of the detector arrays. Indeed, cosmic rays interacting with KIDs produce transient glitches in the raw time-ordered information (TOI). The data affected by large-amplitude glitches are rendered unusable for cosmology and must be masked out in subsequent data processing. Even worse, smaller glitches could remain hidden within the TOI noise, contributing an additional non-Gaussian systematic effect, which can influence, for example, the estimation of the cosmic microwave background (CMB) angular power spectrum. In particular, there is a risk of confusion between glitch residuals and the non-Gaussian features caused by topological defects or inflation processes.

We based our study on a one hundreds-pixels LEKID array developed for the previous study (see Sec. 4.1). We studied the impact of ionising particles on this array in laboratory in order to analyse the underlying the physical process. Then, we compared such impact on other real space experiment (like Planck HFI) with a simulation. Finally, we developed solutions to minimise this effect.

4.2.1 Cosmic rays impact in previous far-infrared space missions

Cosmic rays (CRs; [Mewaldt et al.(2010), Leske et al.(2011)]) at a typical orbital configuration (i.e. low Earth orbit or second Lagrangian point) are essentially composed of massive particles: about 88 % protons, 10 % alpha particles, 1 % heavier nuclei, and less than 1 % electrons. The energy spectrum of CRs peaks around 200 MeV, corresponding to a total proton flux of 3000 - 4000 particles $m^{-2}\,sr^{-1}\,s^{-1}\,GeV^{-1}$. This flux is especially dominated by Galactic CRs in periods of low solar activity. The solar wind decelerates the incoming particles and partially stops those with energies below about 1 GeV. Since the strength of the solar wind is not constant due to changes in solar activity, the level of the CRs flux varies with time [Mewaldt et al.(2010)]. The energy distribution of protons is presented in Fig.4.10. Below about 40 MeV, we assume protons do not have enough energy to penetrate the FPU box to reach the cold focal plane of the instrument.

The impact of CRs on the detectors time-ordered data has been observed in previous far-infrared space missions that used bolometers. For example, glitches in the COBE-FIRAS data were identified to be caused by cosmic-particle hits on the detectors as they were not correlated to the mirror pointings [Fixsen et al.(1996)]. The number of glitches observed for this experiment was sufficiently small and their removal was not a major problem. Glitches have been also identified in the Herschel Space Observatory both in the SPIRE (spiderweb bolometers operated at temperatures close to 0.3 K; [Griffin et al.(2010)]) and PACS (high-impedance bolometers at 0.3 K; [Horeau et al.(2010)]) instruments. Two types of glitches have been observed in the SPIRE detector timelines: large events and smaller co-occurring glitches, both associated with the impact of cosmic rays on the arrays. In the PACS instrument, the energy deposited by cosmic rays raised the bolometer temperature by a factor between 1 to 6 % of the nominal value. Moreover, 25 % of the hits depositing energy on the bolometer chips affect the adjacent pixels.

For the purposes of this study, we consider a case similar to the impact of CRs observed by HFI of Planck. The Planck satellite[2] observed the sky between August 2009 and August 2013

[2] *http://www.esa.int/Planck*

in the frequency range from 30 GHz to 1 THz [Planck Collab. (2014)]. It consisted of a telescope, a service module, and two instruments: the High Frequency Instrument (HFI) and the Low Frequency Instrument (LFI). The HFI operated with 52 high-impedance bolometers cooled to 100 mK at frequencies between 100 GHz and 1 THz. In the CMB channels (between 100 GHz and 300 GHz), the HFI sensitivity per pixel reached exceptional performance corresponding to a NEP of between $1-2\cdot10^{-17}\ WHz^{-1/2}$ [Planck Collab. (2011)]. However, the HFI detectors exhibited a strong coupling with CR radiation, which produces transient glitches in the raw time-ordered information (TOI) with a rate of about 1 Hz and a template that can be fitted by a sum of various first-order, low-pass filters with a main time constant between 4 and 10 ms plus long time constants up to 2 s. Flight data from HFI and ground tests provided strong evidence that the dominant family of glitches observed in flight are due to CR absorption by the silicon substrate of the HFI detectors [Catalano et al. (2014)], [Planck Collab. (2014)]. Glitch energy is propagated to the thermistor by ballistic[3] phonons, with non-negligible contribution by thermal diffusion. The average ratio between the energy absorbed per glitch in the silicon wafer and that absorbed in the bolometer is roughly a factor of 650, in this specific case [Catalano et al. (2014)].

4.2.2 Glitch characterisation from laboratory measurements

We have used the 2 mm LEKID array used for the sensitivity test discussed in Sec.4.1. We add an americium alpha particle source (^{241}Am) at a distance of about 600 μm from the array. The alpha particles hit the array on the front side. The ^{241}Am source produces 5.4 MeV alpha particles, which are completely absorbed by the 300 μm silicon wafer. To rescale the absorbed energy to that corresponding to the peak of the in-space CR spectrum, we set a 10 μm copper shield in front of the source. This allows the reduction of americium alpha particle energy to a normal distribution centred at 630 keV with a 30 keV 1 σ dispersion (resulting from a Geant-4 simulation). This energy corresponds to the energy absorbed in the silicon wafer by a 200 MeV proton, which is the particle most typical of CRs at the second Lagrangian point. We performed a read-out of the LEKID array with the NIKEL electronics tuning the sampling frequency between 20 to 500 Hz. The main results of the test are described below.

[3]Ballistic conduction is the unimpeded flow of energy that carries charges over large distances within a material.

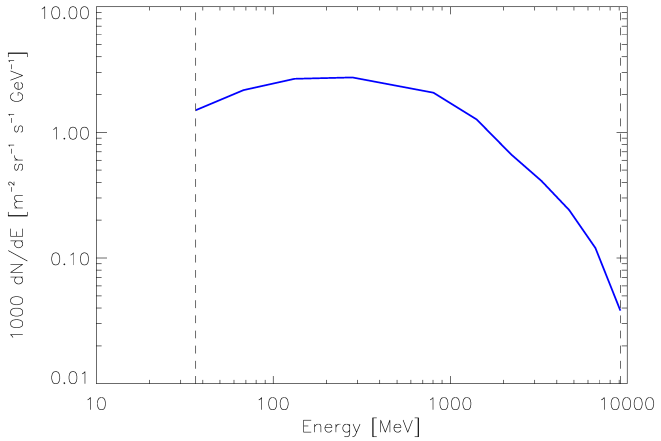

Figure 4.10: Energy distribution of CR protons at L2. The vertical dashed lines represent the range of energies of interest for a typical payload (from 35 MeV to 10 GeV)

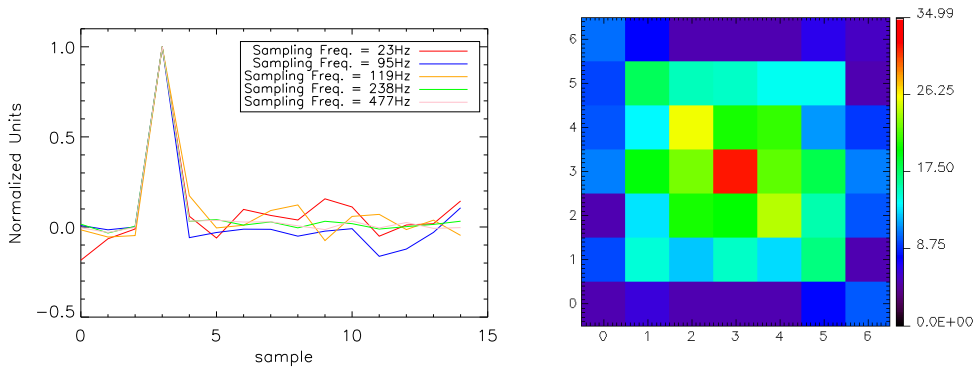

Figure 4.11: Glitch characterisation results. Left panel: glitch template over a line of samples for different read-out sampling frequency. Right panel: propagation of the energy in the LEKID array in units of signal-to-noise ratio. Each pixel in the map corresponds to a LEKID detector.

- **Suppression Factor:** As expected, the observed glitches are mostly constant in amplitude. This is because of the slightly fixed point-of-contact and impinging energy. Starting from the NEP measured in the previous section and the LEKID time constants measured in Sec. 4.2.2, we derived calibration factors (in units kHz/keV) as a function of the sampling frequency. Results are presented in Tab 4.3. This allows us to derive a suppression factor χ, which is defined as the ratio between the deposited energy and actual energy detected by the LEKID. This quantity is calculated as

$$\chi = \frac{E_\alpha \cdot C}{Amp},$$

where Amp is the maximum amplitude detected for each pixel measured in Hz, C is the calibration factor, and E_α is the deposited energy of the α particle (630 keV). We calculated the suppression factor at around 2000 and this value is nearly constant (as expected) for different read-out sampling frequencies. We estimated the variability of the suppression factor through the different pixels to be equal to 35%. This means that when the particle hits the silicon very close to a LEKID, only 0.05 % of its energy is transferred to the detector. The derived suppression factor is about three times larger then the measured one between the silicon wafer and the high-impedance bolometers of HFI.

Sampling frequency [Hz]	Calibration factor [kHz/keV]
23	20
95	85
119	100
238	200
477	420

Tableau 4.3: Calibration factor derived from measurement for different read-out sampling frequencies.

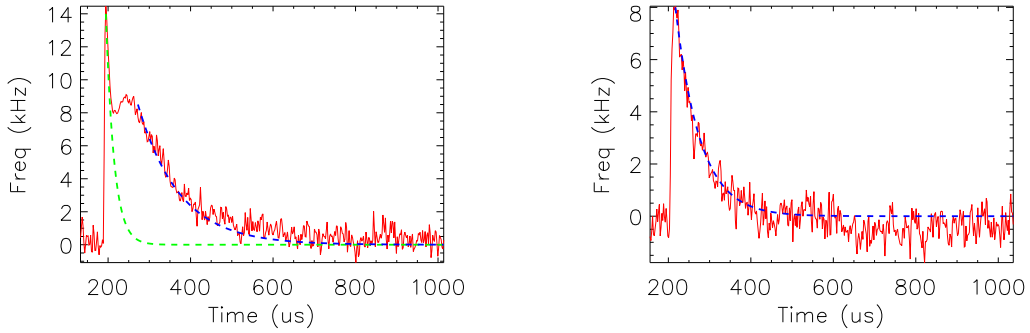

Figure 4.12: Typical glitches produced from the hit of a Cd X-ray on the LEKID array, along with the time constants of a two exponential model (left panel) and one exponential model.

- **Time Constants:** As shown in the left panel of Fig 4.11, the glitch time constants are unresolved for a range of sampling frequencies up to 500 Hz. This means that, in any case, for typical in-space read-out electronics, all glitches appear as one sample in the time ordered data instead of few tens of samples in the case of HFI bolometers. [D'Addabbo et al. (2014)] indicated, although not fully confirmed, the presence of a few ms time constants. However, the measurements in this study do not confirm this result and this kind of a slower component is not observed even when stacking a few thousand events.
- **Coincidences:** In terms of detected glitches at a level of 5 σ, the surface of the silicon wafer impacted by a 630 keV alpha particle never extends a square of 6x6 detectors (about 1.4 cm^2), as shown in Fig 4.11 (right panel).

Physical interpretation

In parallel with the tests performed in typical space conditions (e.g. sampling rate and background), we performed measurements dedicated to characterising the interaction of particles with LEKID detectors arrays using faster read-out electronics [Bourrion et al. (2013)]. This version of the electronics can acquire data fast enough to properly interpret the physical processes [D'Addabbo et al. (2014)]. The sampling rate can be tuned from 500 kHz to 2 MHz for a maximum of 12 channels over 500 MHz bandwidth.
For these tests we used a cadmium source that produces 25 keV X-rays and can impact all the detectors of the array with the same probability. If we analyse the observed glitches per detectors, two families of events can be isolated. The first family (Fig 4.12, left panel) peaks at an amplitude of between 12 and 14 kHz and corresponds to about 60 % of the glitches. This family can be represented by a double time-constant model (i.e. the faster between 10-15 μs and the slower between 80-100 μs). The second family of glitches peaks at a lower amplitude (less than 10 kHz) and constitutes about 40% of the glitches. These glitches agree reasonably well with a single time-constant model with the same slower 80-100 μs time constant as the first glitch family.
A possible interpretation of these two time constants is presented below.

- **Fast time constant:** the dynamic response of a LEKID is determined, among other things, by the quasi-particle lifetime[4] [Barends et al. (2008)]. This represents the time occurring between quasi-particle creation following an excitation (phonon or photon) exceeding the superconducting gap and their recombination back into Cooper pairs. This time constant

[4]The equilibrium state of a superconductor at a given temperature is represented by Cooper pair condensate and thermally excited quasiparticles.

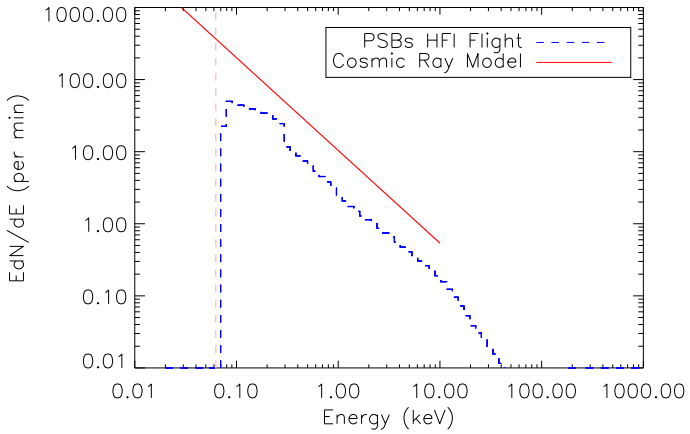

Figure 4.13: LEKID toy proton model (red line) compared to a typical 143 GHz in-flight HFI bolometer (blue dashed line). The pink dashed line represents the LEKID 5 σ level.

varies as a function of local quasi-particle density, meaning that we expect to have shorter time constants for higher working temperature of the device or for stronger signal. Moore et al. [Moore et al. (2012)] have shown that this time constant is equal to about tens of microseconds for low-temperature aluminium film KID fabricated on a silicon substrate. The measured fast time constant of the first family of glitches is compatible with this process.

- **Slow time constant:** as we observed for spider-web bolometers, particles hitting the silicon wafer produce ballistic phonons that can propagate unhindered through the crystal over large distances (up to centimetres [Holmes et al. (1999)]). Typically, ballistic phonons decay within hundreds of microseconds into thermal phonons that cannot be sensed by LEKID detectors because their energy is lower than the superconducting gap. The slower time constant observed might be ascribed to this process.

Starting from this interpretation, we can explain the observed two families of events with the X-ray distance of impact with respect to the considered detector. Rescaling the results of the previous section, at this energy (25 keV) and at this read-out rate, an X-ray hitting the silicon wafer should produce a measurable signal (5 σ) on about nine detectors. When the X-ray impacts the silicon wafer close to the considered detectors, the time constant related to quasi-particle lifetime dominates in amplitude and therefore can be resolved; otherwise only the time constant related to the ballistic phonons propagation can be isolated.

4.2.3 Simulation of the impact of cosmic rays in a LEKID array placed at L2

Starting from the results of the previous section, we developed an analytical model to extrapolate the results to what we would see for this type of LEKID array operating at the second Lagrangian point. Using this model, we can simulate a realistic timestream. In the following subsections, we describe the model and the generated timestream.

4.2.4 Proton toy-model

We consider a solid square box made of silicon with the same volume of the tested LEKID arrays. We also consider that each detector has a surface equal to 2x2 mm^2. The inputs of the model are:

- geometrical parameters of the LEKID array,
- stopping power function and density of the silicon,
- energy distribution of CRs at the second Lagrangian point, and
- ratio between the absorbed energy in the substrate and the energy detected by the LEKID (suppression factor χ).

From the literature, we know the energy distribution of the Galactic Cosmic Ray (protons) at L2:

$$\frac{\Delta N}{\Delta E_{p^+}} \sim E_{p^+}^{-\beta}, \tag{4.2}$$

where β is equal to 0.8. In the energy range of interest we can fit the stopping power function as a power law considering an impact angle equal to θ. We obtain therefore the generic absorbed energy as a function of the proton energy and the impact angle

$$E_{abs} = \frac{E_O}{cos\theta} \cdot (\frac{E_{p^+}}{E_{p^+o}})^{-\gamma}.$$

where E_{p^+o} is the reference proton energy, $E_O = \rho_{sil} \cdot d \cdot SP(E_{p^+o})$ is the reference absorbed energy for an orthogonal impact with ρ_{sil} the density of the silicon, d is the thickness of the silicon die, and $SP(E_{p^+o})$ is the stopping power function calculated at a reference proton energy.
By integrating Eq. 4.2 over the solid angle, surface, and integration time and considering the suppression factor, we obtain the energy absorbed in the detector,

$$\frac{\Delta N}{\Delta E_{LEKID}} = \frac{4\pi A \Delta t E_{p^+o} \cdot \chi}{(2\gamma + \beta - 1) \cdot E_O^{\frac{\beta-1}{\gamma}}} \cdot E_{abs}^{-\frac{\gamma+1-\beta}{\gamma}}, \tag{4.3}$$

where A is the surface of the silicon wafer impacted by a CR, Δt is the integration time, and χ is the suppression factor. In Fig 4.13 we show the spectrum obtained from Eq. 4.3 compared to a glitch spectrum measured from a typical 143 GHz in-flight HFI bolometer.

4.2.5 Simulation of LEKID time-ordered data

Starting from the distribution of the glitches absorbed energy induced by CRs, we simulated timestreams of LEKID data in the absence of sky signals. We added CR events to a realisation of noise with a standard deviation σ given from the expected photon noise level with an average of 0.3 pW. As already shown from laboratory measurements, the LEKID detectors have an unresolved time constant, so we consider that each glitch affects only one point of data. The main results we can derive from this simulation are:

- **Data loss:** As shown Fig 4.14, the CRs generate a rate of glitches of about 1.8 Hz, which is larger than what was observed in-flight on a typical Planck HFI bolometer. This is because the affected surface of the silicon wafer following a CR impact is about 1.4 cm^2, which is roughly twice that of the HFI bolometer silicon wafer. On the other hand, the time constants of the glitches are unresolved for sampling rates up to 500 Hz. The percent level of the flagged data due to the de-glitching is therefore about 1 % compared to about 12-15 % for Planck HFI bolometers.
- **Glitch residual contamination:** One of the main differences in comparing glitch impact between HFI bolometers and LEKID arrays is that for the latter, all detectors share the same substrate, while HFI bolometers are fully independent. As a consequence, CR impacts affect

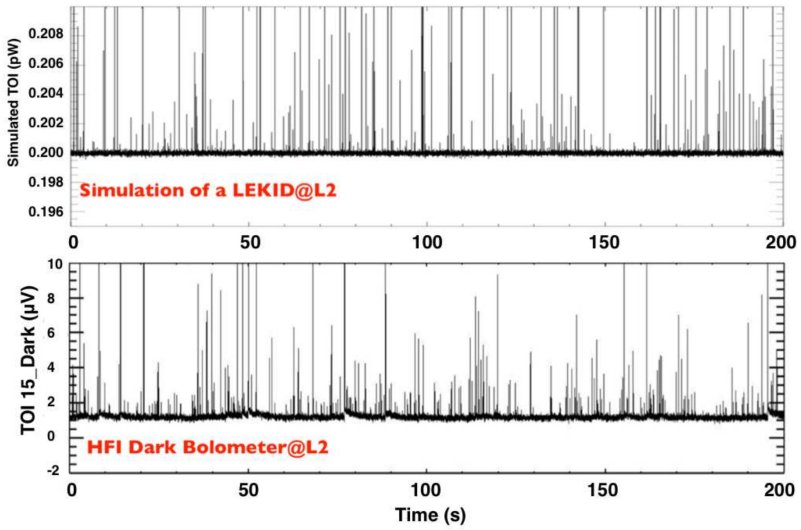

Figure 4.14: Simulated timestream of a LEKID detector at L2 compared to an in-flight HFI dark bolometer.

a surface of about 1.4 cm^2 in LEKID arrays giving a larger number of glitches per detectors. All of the residual glitches (below 5 σ) increase the rms noise by a factor of about 3%. In terms of non-Gaussianity, we expect glitches to induce non-Gaussian features in the TOD. This is shown in the left panel of Fig 4.15, where we present the one-dimensional (1D) distribution for simulated TODs with (red) and without (blue) glitch contribution, assuming Gaussian detector noise at the photon noise level. Glitches are presented as a positive tail with skewness and kurtosis more than 44 σ away from that expected for the Gaussian noise. These non-Gaussian features observed in the TODs are significantly reduced when they are projected to construct maps of the sky. This is because the noise per pixel in the map is expected to decrease as the square root of the number of TOI samples per pixel, $\sqrt{N_{\rm hits}}$, while the glitch contribution decreases as $N_{\rm hits}$. We project the TODs simulated above onto sky maps to test this hypothesis. We assume a 2.5 year space mission and a typical sky map pixel size of 1 arcmin, which corresponds to N$_{hits}$ = 150 samples per pixel for a Planck-like

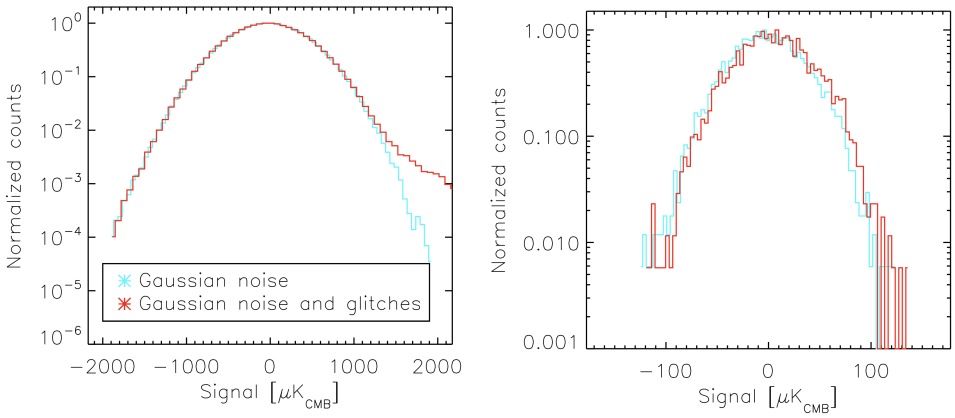

Figure 4.15: Left panel: 1D distribution for simulated LEKID timestream with (red) and without (blue) glitch contribution. Right panel: 2D distribution for simulated LEKID sky map with (red) and without (blue) glitch contribution.

sampling rate. We find that the glitch contribution leads to non-significant, non-Gaussianity in the final maps, as the skewness and the kurtosis is less than 0.23 σ away from that expected for the Gaussian noise. This can be observed in the right panel of Fig. 4.15 where we present the 1-D distribution of the pixel values for the projected sky maps in the case of noise only (blue) and noise and glitches (red) simulations.

4.3 Conclusions and Perspectives on KID developments

- **Perspectives on LEKID Sensitivity under typical space optical loads :**

  We have extensively characterised LEKID arrays optimised to work within five bands suitable for CMB space observations. We have implemented standard measurement protocols allowing to potentially test a large number of arrays in a reproducible and documented way. This is extremely important in the R&D phase in which new materials and designs have to be compared in order to identify promising candidates. Adopting this same protocol, we have tested the arrays covering the band 70-630 GHz. All the LEKID arrays seem to satisfy the stringent requirements in terms of sensitivity of post-Planck satellites dedicated to CMB polarisation studies.

  The future generation space instruments devoted to CMB studies will employ thousands pixels. Based on this study, i.e. fully multiplexed 100-pixels-like arrays run under realistic conditions, the scaling to the final number of pixels seems straightforward. The next step of the R&D phase will be therefore to improve the uniformity within kilo-pixels-like arrays.

- **Perspectives on LEKID cosmic rays susceptibility :** We have shown that the array optimised only for the low background sensitivity study have a cosmic ray impact rate that is larger than HFI detectors, they present extremely short glitch time constants (not resolved up to 500 Hz sampling frequency) compared to the HFI bolometers time constants (from 5-10 ms up to 2 s). This corresponds to roughly 1 % of the data flagged due to the de-glitching compared to about 12-15 % for Planck HFI bolometers. Residual glitches (below 5 σ) add no significant contributions to the noise rms (less than 3 %) and have negligible impact on non-Gaussianity studies.

  Starting from these promising results, we think that the propagation of the non-thermalized phonons in the silicon substrate can be attenuated using suitable phonon dampers. The aluminium ground plane surrounding the pixels represents the first example of such a damper. In order to downgrade even more efficiently the phonons energy below the aluminium gap, i.e. harmless phonons for the LEKID, we have already added a titanium layer on the back of the wafer. Titanium, a superconductor with critical temperature around 0.45 K (superconducting gap $\Delta Ti_{gap} < \Delta Al_{gap}$), is chosen in order to prevent secondary phonons from reaching the aluminium and breaking Cooper pairs in the LEKID. The proximity of this lossless superconductor layer does not affect the internal quality factor of the resonators as would be the case for normal metal films like gold. The first results of this test exhibits a rate of coincidences much smaller. The size of the array that is affected is now about 0.5×0.5 = 0.25 cm^2, a factor of 5 smaller than in the previous case.

- **Perspectives on instrumentation developments :** In order to focus light onto the KID arrays and modulate the polarisation or produce interference, we need to optimise optical elements specifically designed to interface with KID detectors. All these components have to be designed and fabricated and tested first in the laboratory in order to mimic as much as

possible the environment of a given experiment. In our laboratories, we have complementary skills related to the cryogenics, mechanics, optics, readout and software which allowed for designing and installing a new instrument based on KID technology. For the future, we need to become more proficient in AR-coating techniques on curved silicon dielectric coating using thermal compression, dicing saw machining, silicon grain pulverisation, and 3-D lithography. Moreover, we need to develop the pipeline for data acquisition and processing of KID-based instruments in the different laboratories of the collaboration.

- **General Perspectives on KID developments :** The development of KIDs detectors and the annex instrumentation will be central for my activities over the next years. We will keep improving the performance of KID detectors for space mission in order to increase the technology readiness level (TRL) of KID detectors. Today in France, the effort of the R&D activities on experimental cosmology takes place within the collaboration of IN2P3 laboratories (APC, CSNSM, LAL and LPSC), INP (Institut Neel) and INSU (IPAG) laboratories. This collaboration has strong roots starting with the Grenoble collaboration (Institut Neel, LPSC, IPAG). The Grenoble collaboration will be consolidated through a GIS (groupement d'interet scientifique). Today, all these laboratories participate in preparing the next generation instrument based on KID technology for cosmology and millimetre science. In order to be a competitive candidate for the next generation instruments devoted to cosmology, we need to develop and test new focal plane with tens of thousand of pixels and develop on-chip multi-color and polarization splitting. For the following years our plans, already expressed in several forms (as for example CNES working group on mm and sub-mm LEKID and instrumentation, Labex FOCUS road map), are to consolidate the results acquired with the R&D programs and transfer our knowledge on bigger arrays of detectors (of the order of few 10k-pixels) to bigger arrays (tens of k-pixels). We will also work on the different architectures of the planar antennas coupled with KID (antenna-coupled KID) in order to reduce the size of the focal plane and to be directly sensitive to polarisation. We complement these studies by our "spectroscopic" work carried. Together with the development directly related to the KID, we also aim to develop and improve the readout and the overall instrumentation.

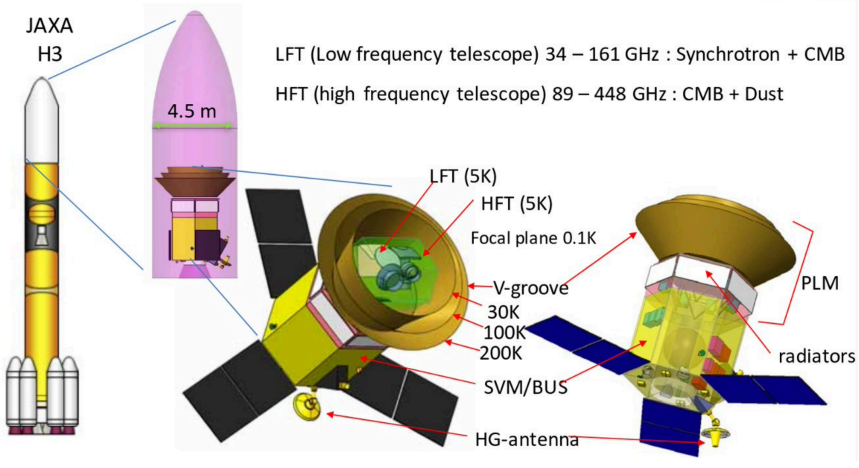

Figure 4.16: Litebird design of the payload and the instruments LFT and HFT.

4.4 An existing space-borne project: the LiteBIRD Satellite

For the next years, together with the ground-based instruments and technological developments, our interest also lies with the LiteBIRD satellite. LiteBIRD is the only CMB polarization satellite which can be deployed within the next 10-15 years. It is complementary with other major experimental effort, the ground-based observatory CMB-S4. LiteBIRD is a JAXA-led, international project, with strong contributions from US, Canada and Europe, both in terms of funding and teams. On the French side, the project has just entered in mid-2018 in Phase A1 at CNES, up to June 2019, and followed by a Phase A2 of 1.5 years to be synchronized with the 'new' JAXA Phase A. The goal of the CNES Phase A will be to increase the TRL of the sub-systems under the French responsibility, contribute to the optimisation of the instrumental design of the High Frequency Telescope (HFT), and define the ground calibration, in coordination with our US, Japanese and European counterparts.

Instrument Design: LiteBIRD will have two instruments : a Low Frequency Telescope (LFT) and a High Frequency Telescope (HFT), observing in 15 frequency bands from 34 GHz to 448 GHz, employing state-of-the-art kilo-pixel arrays of 3510 multi-chroic TES detectors and multiple modulations of the polarised signal obtained through an advanced scanning strategy and a continuously rotating polarisation modulator (HWP). The resolution of LiteBIRD will range from 10 to 70 arcmin in the highest and lowest frequency channels, respectively. The responsibility of the payload is shared between partners : Japan is in charge of the LFT, while Europe has been invited to deliver the HFT. The US will provide the focal planes and Canada the warm electronics for both instruments. The cryogenics chain is overseen by JAXA, apart from the sub-Kelvin stage which is under French responsibility. The design of these two instruments is fully optimised to offer a broad mapping of the astrophysical foregrounds and mitigate the impact of systematics, with a strong control of the temperature stability of both the focal plane and the full optical chain to reach the required sensitivity. Hence, the HFT telescope invokes 9 bands from 89 GHz to 448 GHz, 2262 TES detectors, optics cooled to 5 K, and a continuously rotated HWP as the first optics element.

I will be involved in the preparation of the ground calibration of the instrument (spectral and polarisation chararterisation).

Spectral Calibration : The main goal of the spectral transmission tests of the HFT instrument is to measure the spectral response of individual TES detectors to a known source of electromagnetic radiation. This was determined by measuring the interferometric output of all detection channels for radiation propagated through a continuously scanned polarising Fourier transform spectrometer (FTS). The best solution to be adopted for the FTS is currently under study and it will be one of the results delivered at the end of Phase A.

There are two requirements set at present: the acquisition of the spectral transmission of the single pixels with a resolution better than 0.1 cm^{-1} and a spectral transmission profile of the different channels with an accuracy of about 0.5 %. For such a device the control of systematic effects (e.g. apodisation errors, particle hits and baseline thermal excursions) and the procedure chosen is a key issue and will drive the design of the final system.

Polarisation Calibration : The characterisation of the polarisation of the instrument mainly aims to measure the orientation of the polarisation sensitive detectors in the focal plane. This measurement is of primary importance as it cannot be measured in another way with good precision. Combined with telescope measurements, it will provide the polarisation sensitivity orientation on the sky, which cannot be determined accurately in flight because of lack of well-characterised polarised sources. The requirement for the accuracy of this orientation is of the order of arcminute. A second objective was the check of the cross-polarisation level that was measured at the sub-pixel level.

Bibliography

[Planck Collab & Lawrence (2011)] Planck Collaboration & Lawrence, C. R. 2011, in American Astronomical Society Meeting Abstracts, Vol. 217, American Astronomical Society Meeting Abstracts 217, 243.04

[Roesch et al.(2012)] Roesch, M., Benoit, A., Bideaud, A., et al. 2012, arXiv e-prints, arXiv:1212.4585

[Catalano et al.(2015)] Catalano, A., Goupy, J., le Sueur, H., et al. 2015, A&A, 580, A15

[Monfardini et al.(2015)] Monfardini, A., Benoit, A., Bideaud, A., et al. 2011, ApJS, 194, 24

[Goupy et al.(2016)] Goupy, J., Adane, A., Benoit, A., et al. 2016, Journal of Low Temperature Physics, 184, 661

[Bourrion et al.(2012)] Bourrion, O., Vescovi, C., Bouly, J. L., et al. 2012, Journal of Instrumentation, 7, 7014

[Masi et al.(2019)] Masi, S., de Bernardis, P., Paiella, A., et al. 2019, J. Cosmology Astropart. Phys., 2019, 003

[Catalano et al.(2016)] Catalano, A., Benoit, A., Bourrion, O., et al. 2016, A&A, 592, A26

[Leduc et al.(2010)] Leduc, H. G., Bumble, B., Day, P. K., et al. 2010, Applied Physics Letters, 97, 102509

[Swenson et al.(2010)] Swenson, L. J., Cruciani, A., Benoit, A., et al. 2010, Applied Physics Letters, 96, 263511

[Monfardini et al.(2016)] Monfardini, A., Baselmans, J., Benoit, A., et al. 2016, Society of Photo-Optical Instrumentation Engineers (SPIE) Conference Series, Vol. 9914, Lumped el- ement kinetic inductance detectors for space applications, 99140N

[Leduc et al.(2010)] Leduc, H. G., Bumble, B., Day, P. K., et al. 2010, Applied Physics Letters, 97, 102509

[Bueno et al.(2014)] Bueno, J., Coumou, P. C. J. J., Zheng, G., et al. 2014, Applied Physics Letters, 105, 192601

[Calvo et al.(2014)] Calvo, M., D'Addabbo, A., Monfardini, A., et al. 2014, Journal of Low Temperature Physics, 176, 518

[Mewaldt et al.(2010)] Mewaldt, R. A., Davis, A. J., Lave, K. A., et al. 2010, ApJ, 723, L1

[Leske et al.(2011)] Leske, R. A., Cummings, A. C., Mewaldt, R. A., & Stone, E. C. 2011, Space Sci. Rev., 126

[Fixsen et al.(1996)] Fixsen, D. J., Cheng, E. S., Gales, J. M., et al. 1996, ApJ, 473, 576

[Griffin et al.(2010)] Griffin, M. J., Abergel, A., Abreu, A., et al. 2010, A&A, 518, L3

[Horeau et al.(2010)] Horeau, B., Boulade, O., Claret, A., et al. 2012, ArXiv e-prints

[Planck Collab. (2014)] Planck Collaboration, Ade, P. A. R., Aghanim, N., et al. 2014a, A&A, 571, A10

[Planck Collab. (2011)] Planck HFI Core Team, Ade, P. A. R., Aghanim, N., et al. 2011, A&A, 536, A4

[Catalano et al. (2014)] Catalano, A., Ade, P., Atik, Y., et al. 2014a, A&A, 569, A88

[Planck Collab. (2014)] Planck Collaboration, Ade, P. A. R., Aghanim, N., et al. 2014b, A&A, 571, A16

[Bourrion et al. (2013)] Bourrion, O., Vescovi, C., Catalano, A., et al. 2013, Journal of Instrumentation, 8, C2006

[D'Addabbo et al. (2014)] D'Addabbo, A., Calvo, M., Goupy, J., et al. 2014, in Society of Photo-Optical Instrumentation Engineers (SPIE) Conference Series, Vol. 9153, Society of Photo-Optical Instrumentation Engineers (SPIE) Conference Series, 2 Doyle, S. 2008, PhD Thesis, 1, 193

[Barends et al. (2008)] Barends, R., Baselmans, J. J. A., Yates, S. J. C., et al. 2008, Physical Review Letters, 100, 257002

[Moore et al. (2012)] Moore, D. C., Golwala, S. R., Bumble, B., et al. 2012, Applied Physics Letters, 100, 232601

[Holmes et al. (1999)] Holmes, W., Gildemeister, J. M., Richards, P. L., & Kotsubo, V. 1998, Applied Physics Letters, 72, 2250

Conclusion

The deeper I get into this job, the more I realise that the real results of research is to be always limited by new kind of errors, ever smaller and ever harder to be removed. Right from when I started at the "Sapienza" University, my professor used to say: "for being properly a scientist, it is much better to know a little of everything rather than being a big expert on a single field". I still do not know if it is a true statement, but anyway this was the direction I unconsciously followed. I was always comfortable between experimentalist and theorist scientists, trying to learn both languages.

All years spent behind the High Frequency Instrument of Planck have allowed me to join the Grenoble team whose today hopefully I give a valid contribution. The instruments and the related technology that we developed together during these last eight years allowed us to discuss around big projects together with the brightest laboratories in France and over the World.

Since few years, our interest is directed towards the spectroscopy, in particular the FTS techniques. This resulted in the KISS and CONCERTO instruments. They put forward a number of ideas and a experience feed-back for the new generation instruments. Probably indeed, the mid-term future (10-15 years), will be characterised by the need to go deeper on our knowledge of CMB spectral distortion. This because most of the ongoing instrument at date (CMB Stage-4, Simons Observatory, LITEBIRD to cite the most significant ones), should detect in a 10-15 year time scale, CMB B-modes or eventually an upper limit above which it will be difficult to overcome. In both cases, CMB spectral observations will be the only way to go deeper. It seems to me very important to chart a path as of today to be prepared to this challenge. Exactly like when a large part of European cosmologists were involved in making the Planck Satellite working, Americans have already started to develop new technology and instruments to be prepared to CMB B-mode detection.

Figure 4.17: Part of our team in front of the 30-metre IRAM telescope during a winter observing campaign with NIKA (note that we are wearing only t-shirts!)